2015-04-03

# Coastal Shallow Water Diurnal Warming

Xiaofang Zhu
*University of Miami*, xiaofang.zhu@noaa.gov

## Recommended Citation

Zhu, Xiaofang, "Coastal Shallow Water Diurnal Warming" (2015). *Open Access Dissertations*. 1376.
https://scholarlyrepository.miami.edu/oa_dissertations/1376

UNIVERSITY OF MIAMI

# COASTAL SHALLOW WATER DIURNAL WARMING

By

Xiaofang Zhu

A DISSERTATION

Submitted to the Faculty
of the University of Miami
in partial fulfillment of the requirements for
the degree of Doctor of Philosophy

Coral Gables, Florida

May 2015

UNIVERSITY OF MIAMI

A dissertation submitted in partial fulfillment of
the requirements for the degree of
Doctor of Philosophy

# COASTAL SHALLOW WATER DIURNAL WARMING

Xiaofang Zhu

Approved:

Peter Minnett, Ph.D.
Professor of Applied Marine Physics

William Drennan, Ph.D.
Professor of Applied Marine Physics

Adrianus Reniers, Ph.D.
Professor of Applied Marine Physics

M. Brian Blake, Ph.D.
Dean of the Graduate School

Chelle Gentemann, Ph.D.
Senior Principle Scientist
Remote Sensing Systems, Santa Rosa,California

ZHU, XIAOFANG (Ph.D., Applied Marine Physics)

Coastal Shallow Water Diurnal Warming (May 2015)

Abstract of a dissertation at the University of Miami.

Dissertation supervised by Professor Peter Minnett.
No. of pages in text. (145)

A good understanding of diurnal warming phenomenon is important for satellite sea surface temperature (SST) validation against in-situ buoy data and satellite data merging. For the coastal region, it also helps to improve the satellite data application to predict ecosystem health such as coral reef bleaching. Compared to its open ocean counterparts that have been studied extensively and modeled with good success, coastal diurnal warming is rarely studied. This study summarizes one of the first studies which attempts to study the coastal diurnal warming comprehensively, considering many aspects of coastal characteristics, including the influence of tidal impacts and geographic locations, using an integrated approach including in-situ data analysis, modeling and satellite SST analysis.

First, two in-situ datasets at the Caribbean Sea and at the Great Barrier Reef region were studied. We found that most stations have clear diurnal warming signals at sub-surface depths. Similar to open ocean cases, the warming is influenced by wind and insolation. Coastal tidal impact on warming was quantified and found to be limited. Water depths, station reef types, and relative locations of the station to the barrier reef chain in the east-west direction were found to affect the warming significantly. Second, three one-dimensional diurnal warming models are used for simulation. The simple “box model” predicts the warming amplitudes best during strong and intermediate(>5 $ms^{-1}$) wind speeds while the POSH (Profiles of Ocean Surface Heating) model predicts the low wind warming best, though the modeled heat does not penetrate sufficiently downward. Finally, coastal SST from polar-orbiting and geostationary satellites are tested. Comparing SST against in-situ data yielded bias of < 0.15K, and standard deviations of between 0.56K and 0.74K, similar or better than previous studies. Geostationary data captures diurnal warming well both in amplitudes and timing, while polar data captures the warming with various degree of success.

# ACKNOWLEDGEMENTS

I would like to express my sincere gratitude to my advisor, Dr Peter Minnett, for his continuous patience, support and guidance throughout my research. Doing a Ph.D. long distance is a journey with the challenges and rewards which I did not expect at the beginning, I am very grateful for our bi-weekly phone chats, the great opportunity of being a visiting scientist at National Oceanic and Atmospheric Administration, and trips to many conferences and workshops, which keeps me motivated and keep my research work relevant in the community. I am also truly thankful to my dissertation committee members, Drs. William Drennan, Ad Reniers, and Chelle Gentemann, who offered me their many insightful and invaluable advices for my research.

The research project benefits from help from many people. I thank Jim Hendee, Mike Jankulak, Miguel Angel Izaguirre, Carrie Mafrino, Rob Hedges and Wessley B. Merten for the instrument maintenance and additional temperature loggers' installation efforts at the Caribbean locations. Lewis Gramer has provided great suggestions for the data analysis. I also would like to thank Ray Berkelmans, Richard Brinkman and William Skirving for providing the Great Barrier Reef logger data, sharing knowledge of reef hydrodynamics and interaction with coral physiology, and their hospitality during my visit in Townsville, Australia. Helen Beggs and Leon Majewski have provided the TWP+ dataset for our satellite data study. Michael Brunke has provided me the code of ZB model.

Also, I would like thank many people including Alexander Ignatov, Eileen Maturi, Andy Harris, Jonathan Mittaz, Xingming Liang, John Sapper, Ron Vogel, Bob Potash and Gordana Rancic , who makes my experience in NOAA a very rewarding one and many

have become dear friends. They have provided me amazing environments to grow, both as a person and as a scientist, and have taught me many useful skills in research and programming. Back in RSMAS, Professor Roland Romeiser and Josefina Olascoaga and fellow students Zhixuan Feng and Yang Liu, as well as Cary Rios and Veronica Tejeda from Graduate Studies Office have been very helpful in helping me meeting registration requirements, setting up student seminars and accommodating me during my visits back in Miami.

This dissertation work is funded by the NASA grants NNX08AH99G and NNX13AE30G.

Last but not least, thanks to my family and friends, especially my husband Ivan, for his amazing love, support, and encouragement throughout the way. And also thanks my parents back in China, and my grandma who has just passed away in January, you have taught me the meaning of unconditional love and support.

# Table of Contents

# List of Figures

# List of Tables

# Chapter 1 Introduction

## 1.1 Study focus and motivation

Ocean diurnal warming refers to the phenomenon where the upper few meters of the ocean heat up daily due to the absorption of solar radiation. Since the top 5m of the ocean absorbs about 60% of the incoming solar radiation (Fairall et al., 1996), the near-surface water tends to warm up more than the layers beneath. The precise distribution of the heat content, i.e., the shape of the vertical temperature profile, depends primarily on the strength of upper ocean mixing. Diurnal warming related error is one of the largest potential absolute contributor to the SST uncertainty budget (up to O (1K)), albeit only at specific times (near local noon) and specific environmental conditions (low wind speeds). Thus an accurate quantification of the diurnal warming amplitude and vertical structure is important for merging satellite sea surface temperature (SST) data taken at different times of day, for more accurate surface SST retrieval and validation against buoy data taken at certain depths (Gentemann et al., 2004), as well as for correctly calculating air-sea heat flux (Fairall et al., 1996).

This study is concerned with the diurnal warming in shallow coastal waters. Shallow coastal waters refer to locations adjacent to land, with a water depth ranging from a few meters to up to 30 meters, a depth comparable to the diurnal warming layer found in studies of diurnal heating in the open ocean.

Diurnal warming in coastal shallow waters is of interest for a number of reasons. First, for satellite measurements of SST at the coastal regions, only those from infrared radiometers can be used due to side-lobe contamination in the microwave radiometer measurements. Since infrared measurements are vulnerable to cloud contamination, merging multiple SST measurements taken from satellites with different overpass times is needed to reduce data loss from clouds. Knowledge of the coastal SST diurnal variation is essential for such data merging. Second, deep ocean diurnal warming has been studied extensively in recent years, with the development of physical and empirical modeling tools. Thus, extending the research towards more complex coastal cases, and studying the similarities and differences of the two is a natural next step. Finally, understanding coastal diurnal warming could help improve the coral reef bleaching prediction by understanding coral depth daily heating signals and gauging short-term thermal stress on the corals.

## 1.2 Study materials and structure of the dissertation

The coastal diurnal warming is studied using an integrated approach including in-situ data analysis, satellite SST analysis and modeling. For in-situ temperature data, two in-situ datasets at the Caribbean Sea and at the Great Barrier Reef (GBR) region off northeast Australia are used. The Caribbean Sea datasets have the in-situ wind and light measurements along with temperature profile data at 4 stations, thus it is a good dataset for detailed warming physics study. On the other hand, GBR bottom temperature datasets include over 60 stations throughout GBR for our studying period, thus provide a good dataset to study spatial distribution and characteristics of the warming. For modeling study, we used three one-dimensional models, including two diurnal warming models and a simple bulk heat budget model to study the diurnal warming at a sample station at Caribbean datasets. The model performances at the shallow water site are evaluated, and possible ways to improvement are tested. For satellite data, SST data is obtained from five polar orbiting infrared instruments (AVHRR on NOAA17, 18 and 19, MODIS on

Aqua and Terra) and also hourly SST data from geostationary satellite MTSAT, and study region is the Great Barrier Reef region.

The structure of the dissertation is as follows: Chapter 2 describes the background of this study. It includes descriptions on previous studies and findings from ocean diurnal warming, limited research on coastal shallow water warming, as well as the motivation to study the coastal diurnal warming to aid coral reef bleaching research. Chapter 3 describes the diurnal warming amplitudes, timing, seasonality and the relationship with environmental forcing of the all four Caribbean stations. Chapter 4 concentrates on Little Cayman, one of the Caribbean stations with most vertical temperature measurements. Detailed investigations of diurnal warming dependences are conducted by looking into individual day case studies, as well as summarizing the accumulative and instantaneous impacts of various forcing. In Chapter 5, Great Barrier Reef dataset is studied. Taking advantage of the fact that there are over 60 stations in our study periods and they span a large geographic area with very different environmental characteristics, the emphasis is to study the impacts of the locations and bathymetry features on diurnal warming characteristics in a statistically sufficient way. In Chapter 6 and 7, we investigate how the one-dimensional heat budget and diurnal warming models simulate the daily warming processes at Little Cayman. Chapter 6 describes the details of the models being used and some of the coastal specific physical processes related to shallow water warming, while chapter 7 describes the comparison results with the in-situ data, the merits and limitations of those models, as well as propose some ways to adapt them to coastal shallow water diurnal warming. In Chapter 8, we investigate the usage of satellite sea surface temperature (SST) for shallow coastal locations to study coastal diurnal warming. The data are first validated with the in-situ station measurements. Then we explore whether diurnal warming signals in the SST exist for different stations, as well as their amplitudes and dependences

# Chapter 2 Background

## 2.1 Past studies on ocean diurnal warming

The daily warming of the upper ocean has been a focus of research in recent years. Large diurnal SST variations have been recorded, and areas prone to intense heating have been identified, thanks to the availability of global satellite SST coverage (Gentemann and Minnett 2008, Gentemann et al. 2003, Gentemann et al. 2004, Gentemann et al. 2008, Merchant et al. 2008, Qiu et al. 2009), as well as the ability to measure the warming close to the water surface using both autonomous vertical profilers (Soloviev and Lukas 1997, Ward 2006) and ship-mounted infrared spectroradiometers (Gentemann and Minnett 2008). The largest reported warming reached around 7K at extra-tropical regions (Flament et al. 1994, Gentemann et al. 2008), and surface temperature deviations greater than 3K are not uncommon (Yokoyama, Tanba and Souma 1995, Minnett 2003), though on average surface warming amplitude from measurements is modest [O(0.1 K)]. The daily shape of the surface and subsurface warming and its dependence on environmental forcing including wind and insolation has been documented (Gentemann et al 2003, Stuart-Menteth et al 2005). Moreover, it is realized that the warming has a vertical profile shape influenced dramatically by wind speed (Soloviev and Lukas 1997, Ward and Minnett 2001, Ward 2006, Gentemann et al. 2009), thus when reporting the diurnal warming, it is crucially important to report the measuring depth and recognize the depth genre, whether it is ‘skin’, ‘subskin’ or ‘subsurface temperature’ (Donlon et al. 2002, Donlon et al. 2007, See Figure 2.1).

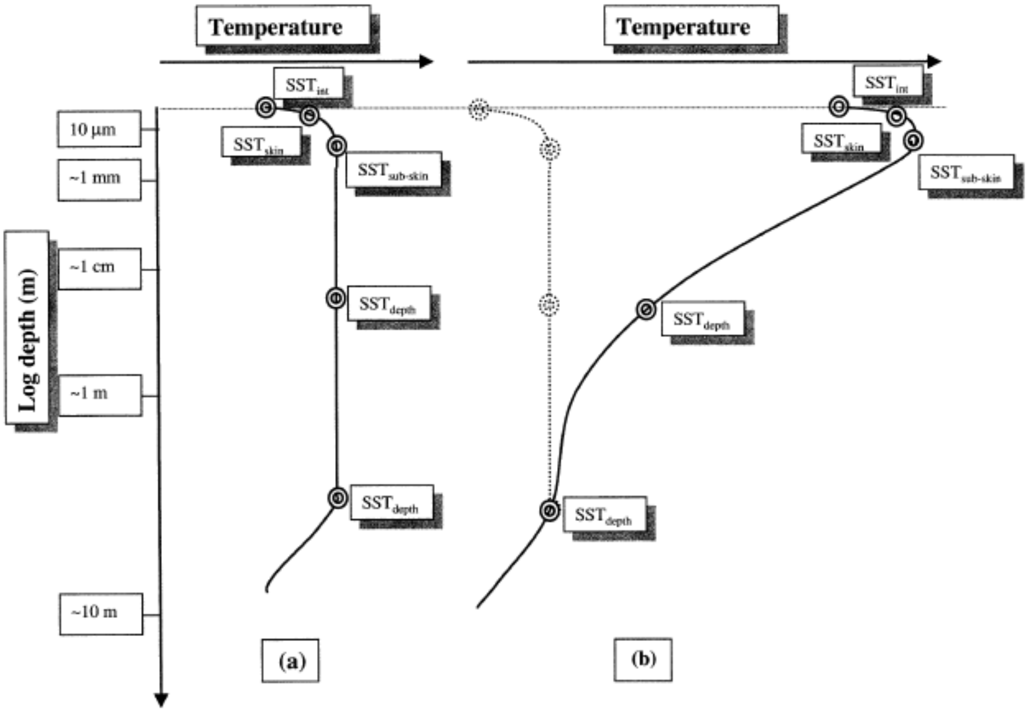

Figure 2.1 Idealized temperature profiles of the near surface layer (~10m) of the ocean during (a) night time as well as day time during strong wind conditions and b) daytime during low wind and sunny conditions. The diurnal warm layer is located below the molecular cool layer, ranging from 1mm to tens of meters under the water surface. The plot is from Fig.1 in Donlon et al 2002.

In the recent studies of diurnal warming phenomenon, many numerical models were developed. Many models are 'regression-based' types, which provide an empirical formula with coefficients derived from analytical results of in-situ or satellite data (e.g. Webster, Clayson and Curry 1996, Kawai and Kawamura 2002, Kawai and Kawamura 2003, Gentemann et al. 2003, Stuart-Menteth et al 2005). While these models are simple to implement and computationally economical, they are based on and limited by the datasets and regions they study, often making them difficult to apply to other datasets and regions with good accuracy. On the other hand, general physics-based one-dimensional models employing turbulence closure or a detailed modeling of turbulence diffusion and mixing (Kantha and Clayson 1994, Price, Weller and Pinkel 1986, Kondo et al 1979) are most physical, but often require comprehensive measurement data and are computationally expensive. Alternatively, a genre of models which combines the physical elements of the mixing as well as some predetermined empirical properties such as shapes of the warming are shown to capture the warming characteristics well and efficiently, thus are widely used (Fairall et al. 1996a, Gentemann et al. 2009, Zeng and Beljaars 2005). For instance, the model from Gentemann et al (2009), a simplified version of the Price, Weller and Pinkel (1986) model and an improved version to the widely used Fairall et al (1996) model, assumes an exponential profile determined by wind speed. It was shown to capture the large warming amplitudes better, also simulate the afternoon cooling better than most other models. Also, Zeng and Beljaars (2005) model calculated the eddy diffusion coefficients in the surface layer using Monin-Obukhov similarity theory, and calculate the warming in a conservative fashion assuming a 3 meter depth warm layer. This diurnal warming scheme is implemented into ECMWF (European Centre for Medium-Range Weather Forecasts) model. For our study, we utilize the model schemes from both Gentemann et al (2009) and Zeng and Beljaars (2005)

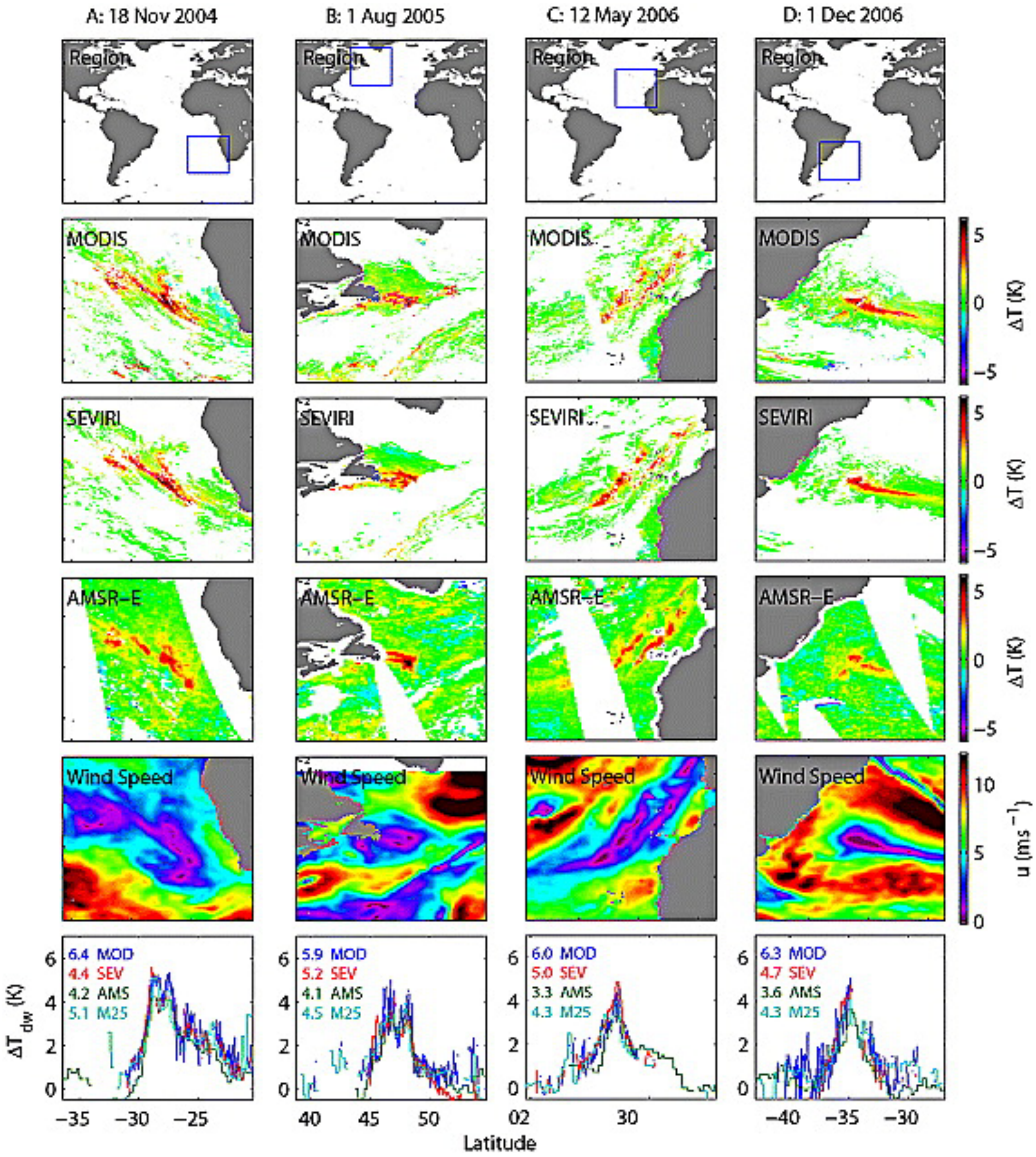

Figure 2.2 Sample SST maps showing diurnal warming observed by infrared and microwave radiometers onboard satellites, and corresponding wind map. The plot is from Gentemann et al 2008.

## 2.2 Shallow coastal diurnal warming studies

So far, most diurnal studies either took place far from the coastline, or made a deliberate effort to eliminate coastal data to avoid the complex coastal dynamics (Merchant et al 2008). A few studies have examined the diurnal warming at seas or coastal regions

(Bohm et al., 1991; Kawai et al., 2006); however water depths of the study locations are over 50 m, a depth far exceeding the diurnal warming layer depth. As such, the effects of bottom and local bathymetry could be viewed as negligible and coastal characteristics were not assessed. A relevant paper on coastal diurnal warming is by Kaplan et al (2003), where the authors examined in-situ temperature measurements from moorings located at 20 to 30 m depth at two offshore locations in Chile. The authors reported several coastal characteristics including tide and sea breeze effects on the diurnal warming near the coast, in addition to the influence of wind and insolation. Due to the limited number of locations however, that study was not able to examine other coastal characteristics such as bathymetry and the effects of shoreline geometry, or to summarize the tidal effect in a statistical fashion.

### 2.3 Possible application: improving coral reef bleaching prediction

Coral bleaching is a generalized stress response in corals but occurs predominantly when temperature reaches an intolerable level, resulting in corals losing their symbiotic algae and turning pale to white. Mass coral bleaching events have occurred in recent years and have been closely monitored using satellite SST data (Berkelmans et al., 2004; Berkelmans and Oliver, 1999). Current coral bleaching monitoring and prediction products based on satellite measurements, such as bleaching HotSpots and Degree Heating Week (DHW) focus on the harmful effect of long-term (12 weeks, bi-weekly data) SST anomalies based on night time SST (Strong et al., 2004).

However, recent studies have suggested the cell death within the coral symbiosis occurs much more rapidly (minutes to hours) than previous thought, especially during high temperature events (Dunn et al., 2004), whereas other studies have found that daily maximum temperatures correspond better to bleaching events than night temperature (Berkelmans et al., 2004; McClanahan et al., 2007). Both point to a possible link between coral bleaching and daily temperature variation at the shallow depths where corals are located. Thus a better understanding of coastal shallow water diurnal warming, both its amplitude and vertical structure is needed so that the surface measurements can be extended in a physically reasonable manner to the depths of the corals. This could improve coral bleaching prediction and monitoring.

# Chapter 3 Diurnal warming signals at the Caribbean dataset

In this chapter, we describe the first in-situ dataset we use to study the diurnal warming: the Caribbean dataset. The Caribbean dataset includes temperature measurements at multiple depths with co-located weather and light measurements at four locations. We first describe the study locations, physical environments and instrument setup of the dataset. Then we look for diurnal warming signals both in the water temperature time series and in temperature spectrum domain. The averaged daily temperature evolution, diurnal warming statistics for each station as well as the seasonal changes of diurnal warming are described.

We reserve the study of relationship between warming characteristics and environmental forcing for next chapter. There our study will be concentrated on one of stations, where the temporal and spatial resolution of the temperature data is highest.

## 3.1 Locations and local physical environment

The Caribbean dataset includes measurements from four locations: southwest Puerto Rico (station ID LPPR), Little Cayman Island (station ID LCIY), St Croix in the U.S Virgin islands (station ID SRVI), and Lee Stocking Island at Bahamas (station ID CMRC). The stations belong to the National Oceanic and Atmospheric Administration (NOAA)'s Integrated Coral Observing Network (ICON) program. All stations were located close to the shore ( less than 300 m at SRVI, CMRC and LCIY,  and less than 3000 m in LPPR inside a bay). The station locations were chosen to be protected from dominant wind direction to avoid being pounded by high seas (Jim Hendee, personal communication).

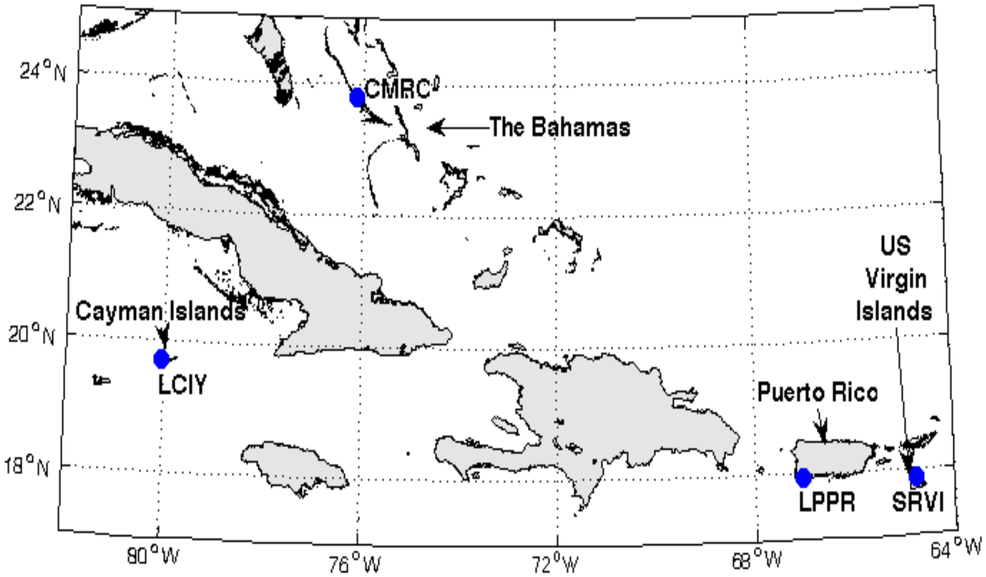

Figure 3.1 Map of the locations of four Caribbean stations LPPR (17.939 °N , 67.052 °W) , SRVI (17.784 ° N, 64.762 ° W) , LCIY (19.699 ° N, 80.06 ° W) and CMRC (23.791 ° N, 76.139 °W) marked in blue dots.

The winds at the Caribbean sites are a combination of the dominant Easterly Trades and diurnal sea breeze, which is a mesoscale phenomenon caused by the differential heating between land and sea (Miller et al 2003). As a result, wind speeds have an obvious diurnal cycle, with stronger wind during the daytime and weaker wind speed at night (Figure 3.2) .The wind directions are mostly from the east, mostly between 30 to 120 degree at the Puerto Rico station (LPPR1) , Bahamas station (CMRC), and Little Cayman station (LCIY2), while the wind direction is mostly from 90 to 150 degree in the St Croix station (SRVI). The wind pattern is similar to those found in this area, Caribbean locations such as Puerto Rico (Altaii & Farrugia, 2003).

The Caribbean region has micro tidal ranges (Kjerfve 1981). Three of the stations we study have tidal amplitudes of less than 0.4 m, while CMRC has somewhat larger tidal range of 0.8 m (Figure 3.3). No currents measurements are available. However, tidal currents are believed to be very weak due to the small tidal ranges and proximity to the shoreline, except when the location is close to a tidal inle, which is the case of the CRMC station in Bahamas.

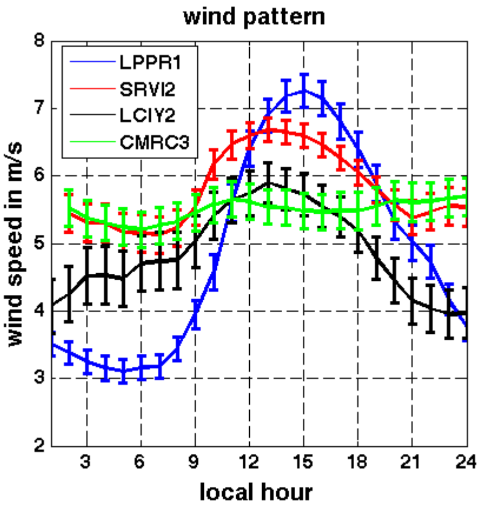

Figure 3.2 Daily averaged wind speeds at four ICON stations using a year worth of data. Error bar denotes the 95% confidence interval.

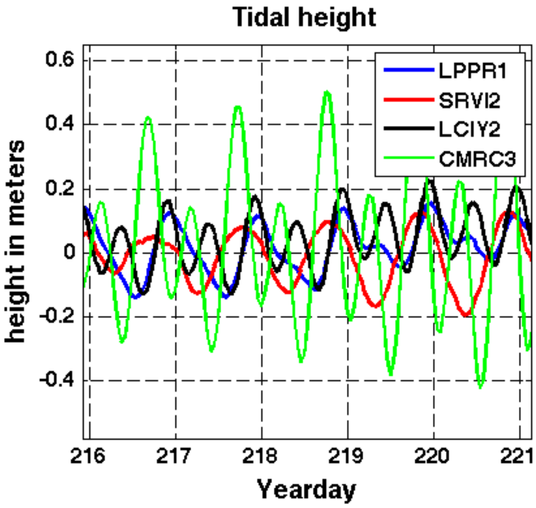

Figure 3.3 A sample period of the tidal height at four ICON stations. X-axis shows year day. For different stations, one year of data are from different years. LPPR1 is from 2009, SRVI is from 2007, LCIY2 is from 2009 and CMRC3 is from 2006.

### 3.2 Instrument and data

For each station, a pylon was installed in about 7 m depth of water on sea bottom categorized as ‘colonized pavement’ which is flat, low-relief, solid carbonate rock with coverage of algae and coral as the structure of the pylons require at least 20 m in diameter of flat terrain for the installation of chains to brace the structure (Figure 3.4).

A variety of meteorological and oceanographic instruments are attached to the station pylons above and under the water (Table 3.1). Above water measurements include wind speed and direction, air temperature, air pressure, precipitation, relative humidity and light with an hourly resolution. Light intensity is measured in 3 ultraviolet wavelength bands and at visible wavelengths (PAR, photosynthetically active radiation). The broad spectrum solar radiation can be calculated from PAR assuming visible radiation represents a constant fraction (=0.4) of the total incoming radiation (Gill, 1982). Underwater, hourly water temperatures and depth (pressure) variations were recorded by CTD (Conductivity, Temperature, Depth Sensors) at a ‘shallow depth’ (1~2 m below the water surface) and at a ‘deep’ depth (4 to 6 m). At LCIY station, only the ‘deep’ depth was measured hourly by CTD. For February to September 2011, 6-minute resolution water temperature and depth (pressure) measurements were available at three near-surface depths (1.2 m, 1.5 m and 2 m) and a near-bottom depth (7.2 m) from four additional loggers.

Figure 3.4 A picture of station pylon at LPPR1 stations, the light and atmospheric instruments are located on top at about 6.5 m height.

To study the diurnal warming phenomenon, one year of water temperature and environmental data from each station were analyzed. To ensure there were minimal missing data, measurements from different years were used (LCIY data from 2011, LPPR data from 2009, SRVI data from 2007 and CMRC data from 2006). They also took advantage of the measurements from the additional temperature logger at the LCIY station from February to September in 2011.

| | Measurement types | Instrument | average installation depth |
|---|---|---|---|
| Surface | light (UV and PAR) | Biospherical BIC2104R | distance above mean water surface:<br>LPPR1: 6.5m<br>SRVI2: 6.5m<br>LCIY2: 7.3m<br>CMRC:6.5m |
| | air temperature | Campbell Scientific model107<br>Vaisala WXT510 | |
| | wind speed<br>wind direction | RM Young Models 05106, 32500<br>Vaisala WXT 510 | |
| | Relative humidity | Vaisala WXT510 | |
| | Barometric pressure | GE/Druck CS115<br>Vaisala WXT510 | |
| | Precipitation | Vaisala WXT510 | |
| Underwater, shallow | Water temperature | Falmouth NXIC-CTD | Distance below mean water surface:<br>LPPR1:1m<br>SRVI2: 1.7m<br>LCIY2: none<br>CMRC:2.3m |
| | Salinity | | |
| | Depth | | |
| | Light (UV and PAR) | Biospherical BIC2104U | |
| Underwater, deep | Water temperature | Falmouth NXIC-CTD | Distance below mean water surface:<br>LPPR1: 5m<br>SRVI2:5.3m<br>LCIY2: 4.6m<br>CMRC: 5m |
| | Salinity | | |
| | Depth | | |
| | Light (UV and PAR) | Biospherical BIC2104U | |
| Additional loggers | Water temperature, pressure | Solinst Levelogger<br>Gold model No 3001 | LCIY2: 1.3m, 1.5m, 2m, 7.2m |

Table 3.1 Instrumentation and types of measurements at Caribbean stations relevant for our study.

### 3.3 Diurnal warming characteristics

This section is concerned with describing the overall shallow water diurnal warming characteristics for all four stations.

### 3.3.1 Sample temperature time series and the impact of tides in daily warming

Warming patterns from different stations are identified by presenting summer temperature time series as well as temperature spectra. The CTD temperature measurements at the LCIY station show a clear single-peak diurnal warming pattern with an early morning temperature minimum and afternoon temperature maximum (Figure 3.5). The afternoon warming peak averaged about 0.5 K at this location. This single peak warming pattern was very similar to those found in SRVI and LPPR stations in the Caribbean data (not shown). The Bahamas CMRC station, however, has a double daily temperature peak for about half of the days in the time series (Figure 3.5). The double peak pattern in the temperature is related to tides, a significant contributor to temperature changes in the coastal warming. It is often difficult to separate the tidal related warming from that caused by the absorption of solar radiation when examining temperature time series, as the solar heating cycle has similar length or is multiple times of tidal cycle lengths. Spectrum analysis, on the other hand, can help tease these issues apart. We have examined the spectra of insolation, tides and temperature measurements. In the insolation spectra, solar radiation induced warming has the fundamental peak at 24-hour cycle as well as harmonics at 12 hours, 6 hours, etc, since the shape is not a perfect sine wave (not shown in plots). Tidal spectrum has many peaks, most of which are related to various diurnal and semi-diurnal components (not shown in plots here). The major components include principal lunar semidiurnal component M2 (period=12.42 hour), principal solar semidiurnal component S2 (period=12 hour), larger lunar elliptic semidiurnal component N2 (period=12.66 hour), lunar diurnal component K1 (period=23.93 hour) and lunar diurnal component O1 (period=25.82 hour). The components with the largest amplitudes for both datasets is the principal lunar semidiurnal component M2, So if a station has strong tidal influence, the M2 peak in the temperature spectra is very visible and can be easily separated from nearby peaks. Thus its strength, referred to here as $PSD_{M2}$ in the temperature spectrum, is a good indicator of the tidal influence on the temperature. Similarly, we use the PSD value at 24 hour period in the temperature spectrum, denoted here as $PSD_{24}$, to represent the influence of insolation on temperature. In addition, the relative strength of the M2 component versus the insolation component ($PSD_{M2}/PSD_{24}$) is used here to quantify the relative importance ratio of tides versus solar heating on the temperature at each location (Figure 3.5).

For the LCIY station, the temperature spectrum analysis shows a strong 24 hour cycle ($PSD_{24} = 31.67 K \cdot Hz^{-1}$) and a weak M2 component ($PSD_{M2} = 0.03\ K \cdot Hz^{-1}$), so the relative influence of tide versus insolation is only 0.11 %. This strong solar driven warming pattern could be enhanced by the effects of the local shoreline geometry and environmental features. The Little Cayman station is located offshore a small island with very calm water and is also protected from the dominant wind direction. The Bahamas station CMRC on the other hand, has a larger tidal influence. In the spectrum analysis, $PSD_{M2} = 169.57\ K \cdot Hz^{-1}$, and is greater than the $PSD_{24}$ ($145.97\ K \cdot Hz^{-1}$). This is because CMRC is located along an island chain, very close to a tidal inlet between two small islands. Previous studies conducted in the region have recorded very strong tidal currents in the tidal inlets at the Lee Stocking Island area where CMRC were located (Thorrold et al., 1994; Vogel et al., 2000).

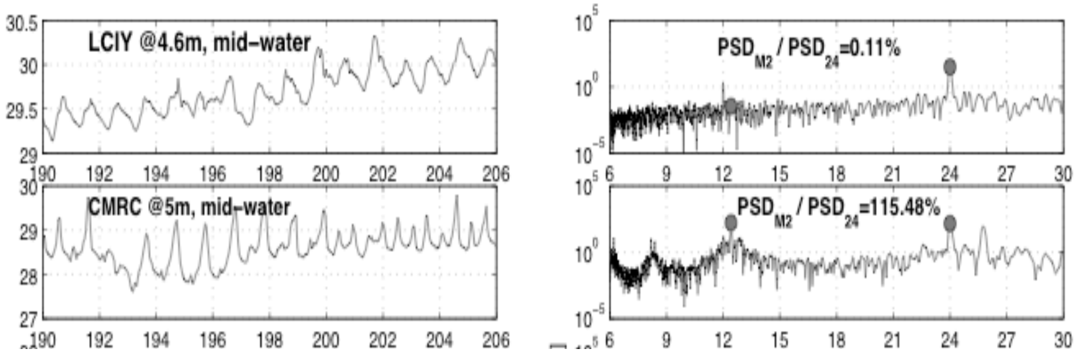

Figure 3.5 Sample temperature time series (left panels) and temperature spectra (right panels) for LCIY station and CMRC station from the hourly mid-water temperature measured by CTD. The grey circles in the spectra denote the power spectral density (PSD) at M2 frequency (12.42 hr/cycle) and 24hr cycle, the temperature spectrum were calculated based on 1-year hourly data for Caribbean stations The power spectral density peaks are not averaged.

### 3.3.2 Average daily temperature evolution, vertical temperature structure pattern

In this section, sample average daily evolutions are shown by binning the temperature measurements according to the station local time. For the stations in the Caribbean dataset, measurements were co-located with different measurement depths, thus the temperatures measured at the shallower depths were always higher than (stratified vertically) or equal to (well mixed vertically) temperatures measured at deeper depths. For the Little Cayman station, St Croix station (not shown) and Bahamas station (not shown), the temperatures at different depths peaked around the same time of the day, while for Puerto Rico station, the temperatures at shallower depth peaked earlier than deeper depth. In the open ocean studies, the temperatures peaks measured at deeper depths usually have a noticeable time lag compared to the temperature peaks measured at the shallower depths, unless the wind speed is high enough to mix heat swiftly downward through turbulent mixing (e.g. Stuart-Menteth 2005). In the shallower coastal ocean, the vertical wind-driven turbulent mixing is generally stronger, and additional turbulent mixing at the bottom can also contribute, thereby making it less likely to have significant time lag between temperature peaks at different depths. Thus, at three out of four stations in the Caribbean dataset, the average temperatures peaked around the same local time at different depths (Figure 3.6).

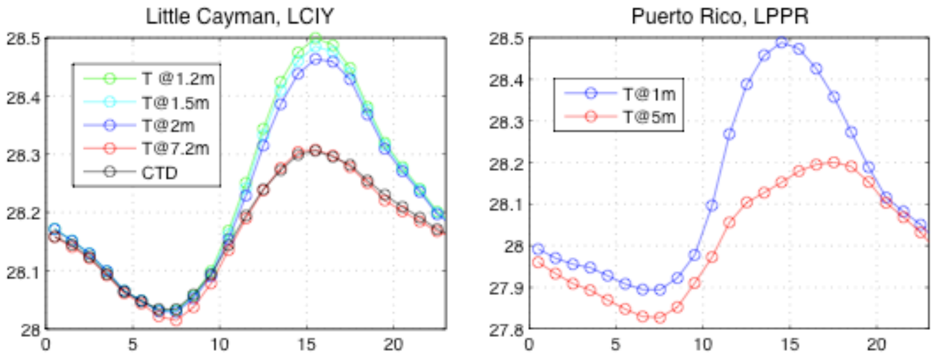

Figure 3.6 Average daily temperature evolutions at two Caribbean stations Temperature data are divided into hourly bins according to the measurement time, and the average temperatures for each hour are shown by circles.

### 3.3.3 The daily warming amplitude and timing of temperature maxima and minima

In this section, the warming characteristics including daily maximum and minimum warming, timing and warming amplitudes were calculated and statistics were summarized (Table 3.2). Daily warming amplitudes were derived by calculating the differences between the temperature maximum and minimum for each day, starting from 6 am to 6 am next day. We chose 6 am as the start of the day because previous studies have shown that the warming from the previous day is likely to linger past midnight, but is usually erased by early next morning (e.g. Gentemann et al. 2009).

Of the four Caribbean stations, LCIY, LPPR and SRVI had relatively small daily temperature differences, the maximum values were in the 1K-2K range, while the mean daily temperature changes were in the 0.3 - 0.7 K range. The CMRC station had a larger mean daily temperature difference (though not necessarily a single peak warming caused by solar radiation, as shown in Figure 3.5) both in maximum temperature difference (close to 4 K), and mean daily temperature difference (>1 K). Daily minimum temperatures mostly occur in the morning between 6:00 to 7:30, i.e. close to dawn or soon after, and similar to previous findings (e.g. Gentemann et al 2003), while daily maximum temperatures mostly occur between 15:00 and 17:00 at all stations. The sub-surface temperatures peak later than those surface measurements recorded from satellite and in-situ radiometers of around of 14:00 - 15:00 (e.g. Gentemann et al., 2003). It is understandable since the measurements at depth tends to lag the surface measurements (e.g. Gentemann et al 2009).

In the vertical, the temperatures at shallower depths generally have larger diurnal temperature increases than at the deeper depths. For the eight-month period data in Little Cayman station, three loggers close to the water surface (depth 1.2 m to 2 m) have maximum daily warming of around 2 K, and mean daily warming ranges from 0.64 K to 0.70 K. The logger near the bottom at 7.2 m has a maximum daily warming of 1.06 K and mean warming amplitude of 0.45 K. The middle water CTD measurements at 4.6 m; however has a maximum daily warming of 1.03 K and mean warming amplitude of 0.40 K, slightly lower than the temperature measured at the bottom, contrary to expectations. While it is possible that this is a real physical phenomenon of ‘warm bottom’, where the bottom is heated up by the absorption of solar radiation energy, this is most likely to be an artifact caused by different sampling frequencies. Because the CTD only recorded hourly averaged temperature, it does not capture the maximum temperature or the precise peak time as can be done with the 6-minute resolution loggers, thus resulting in lower measured warming amplitude.

| Stations | Instrument and duration | Warming amplitudes [K] | | | | Timing [LT] | |
|---|---|---|---|---|---|---|---|
| | | Tmax | Tmin | Tmean | Tstd | tmax | tmin |
| LCIY @2011 | Logger @1.2 m from Feb to Sept | 2.10 | 0.17 | 0.70 | 0.33 | 15.7 | 6.8 |
| | Logger @1.5 m from Feb to Sept | 1.99 | 0.17 | 0.68 | 0.30 | 15.7 | 6.8 |
| | Logger @2 m from Feb to Sept | 1.88 | 0.16 | 0.65 | 0.27 | 15.8 | 6.7 |
| | CTD @4.6 m from Feb to Sept | 1.03 | 0.06 | 0.40 | 0.14 | 15.8 | 7.0 |
| | CTD @4.6 m one year | 1.03 | 0.06 | 0.40 | 0.14 | 15.8 | 7.1 |
| | Logger @7.2 m from Feb to Sept | 1.06 | 0.11 | 0.45 | 0.15 | 15.5 | 7.2 |
| LPPR @2009 | CTD @1 m one year | 1.33 | 0.19 | 0.72 | 0.20 | 14.8 | 6.5 |
| | CTD @5 m one year | 1.13 | 0.17 | 0.49 | 0.14 | 17.5 | 6.4 |
| SRVI @2007 | CTD @1.7 m one year | 1.23 | 0.03 | 0.46 | 0.18 | 15.7 | 6.2 |
| | CTD @5.3 m one year | 1.11 | 0.02 | 0.37 | 0.14 | 15.2 | 6.3 |
| CRMC @2006 | CTD @2.3 m one year | 3.86 | 0.00 | 1.13 | 0.69 | 15.1 | 7.4 |
| | CTD @5 m one year | 3.97 | 0.21 | 1.19 | 0.64 | 15.8 | 7.4 |

Table 3.2 Statistics of the amplitudes of daily temperature changes as well as timings of daily temperature maxima and minima for four Caribbean stations at different depths. The loggers in LCIY refer to the additional four pressure and temperature loggers that recorded data from February to September 2011 in 6-minute resolution. For the hourly CTD measurements, the statistics were calculated from one-year long data for all the stations. At LCIY station, CTD warming statistics were also calculated for a period from February to September 2011, in order to compare with statistics from loggers. LT refers to local time in each station.

### 3.3.4 Seasonality of the daily warming amplitude

In this section, daily warming seasonality is presented by calculating the monthly average of the amplitudes using the 1-year long data (Figure 3.7). The results show that for all four Caribbean stations at shallower depths, the largest warming occurred in spring (April and May). Three stations also have larger warming in late summer and early autumn (August and September). Winter months have the weakest warming amplitude. The temperatures measured at deeper depths have far less variation compared to those measured at shallower depths, indicating the daily warming amplitudes at the middle and bottom parts of the water column are more consistent throughout the year. Counter-intuitively, mid-summer months did not exhibit the largest warming amplitude, when the solar radiation was strong (June at LCIY and SRVI stations, as well as July at the LPPR station). Monthly averaged wind speeds are stronger in mid-summer compared to spring and late summer, a factor likely to explain the lowered daily warming amplitude at the surface. Also note the winds during winter months were strong, which explains the smaller daily warming amplitude, in addition to weaker solar radiation.

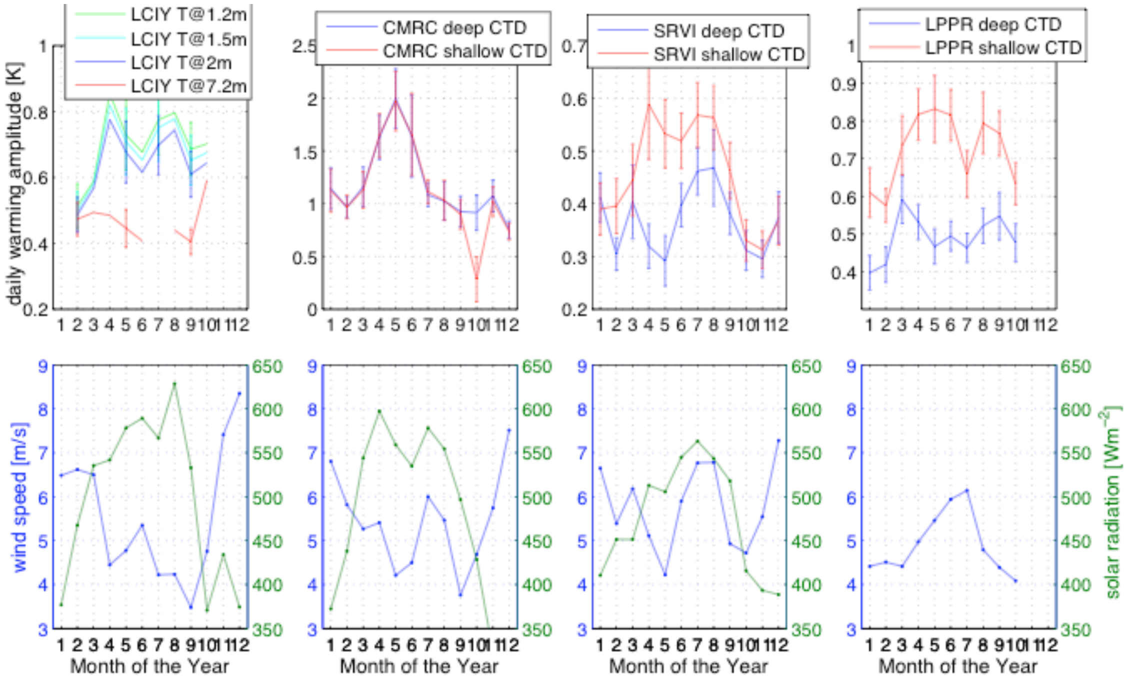

Figure 3.7 Monthly averages of the daily warming amplitudes, wind speed, solar radiation. The 95 % error bars are shown for the daily warming. Reliable solar insolation data at the LPPR station was not available.

### 3.4 Concluding remarks

In this chapter we described the forcing and temperature characteristics for the four stations from the Caribbean temperature dataset. Most locations are found to have a diurnal wind pattern, where the wind speed peaks around noon or in early afternoon.

Tidal range at CMRC station was found to be 1 m, while other three stations were found to have smaller tidal ranges of around 0.5 m. The tidal impact can be shown by examining the temperature time series, where it is found that CMRC station time series show a clear double-peak pattern for some days, while other stations do not. By performing spectrum analysis on temperature it was found that the power spectrum density (PSD) ratio between the semi-diurnal lunar principle tidal component M2 and the 24-hour period insolation component ($PSD_{M2}/PSD_{24}$) is a widely varying parameter. For instance, the ($PSD_{M2}/PSD_{24}$) ratio is 115.48% at the Bahamas station, compared to 0.11% at Little Cayman station. Next, an averaged daily temperature evolution for each station is calculated at various depths. For Little Cayman station where there are five vertical temperature measurements, it is found that there is a bottom mixed layer with a depth of at least 2.6m, and near bottom warming at 7.2m almost always exists. Finally, seasonal changes of diurnal warming are described. The results show that at shallower depths the largest warming occurred in spring (April and May) for all four Caribbean stations. Although the strongest solar radiation was recorded in mid-summer months, this time period did not exhibit the largest warming amplitude, possibly due to strong summer winds.

# Chapter 4 Little Cayman station analysis

Among the two in-situ datasets, we choose the Little Cayman station from Caribbean dataset to conduct a more detailed analysis between diurnal warming characteristics and the environmental forcing. The reason is that the location has co-located light and weather measurements as well as a five-point vertical thermal profile measurement for 6 months in 2011. Also, the station is located in a calmer, well-sheltered environment with minimum effect of tides and currents, thus it provides a simpler yet common coastal scenario to study the phenomenon.

## 4.1 Characteristics of the environmental data at LCIY

Little Cayman Island is the smallest island among three Cayman islands, and has a tropical marine climate. In this section, we examine the detailed weather and tide pattern shown in our dataset for the study location.

### 4.1.1 Wind pattern at Little Cayman station

This wind pattern at Little Cayman is similar to those found in other Caribbean locations such as Puerto Rico (Altaii & Farrugia, 2003). The shoreline orientation of Little Cayman station is about along 70-250N. Thus at this location, the alongshore wind is mostly along the shore to the west, and the wind perpendicular to the shore is almost always offshore. This conclusion was also supported by observing a sample of the wind time series data (Fig 4.2). Note that as the Little Cayman Island is only about 32km$^2$ in area, the sea breeze effect is unlikely to be local. Rather, the sea-land temperature difference between the ocean and the surrounding land mass (Mexico to the west, for instance) is a likely cause.

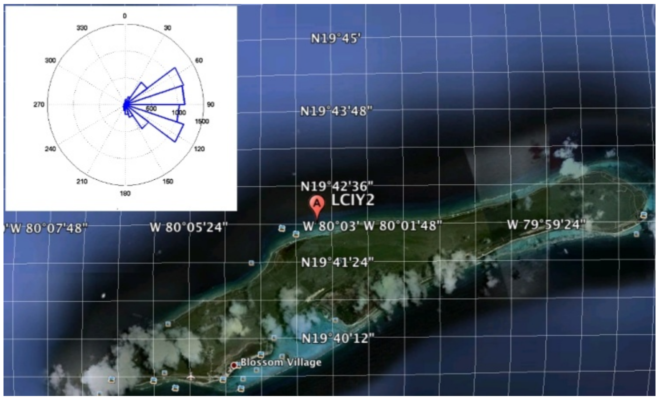

Figure 4.1 The map of Little Cayman with wind rose plot is shown.

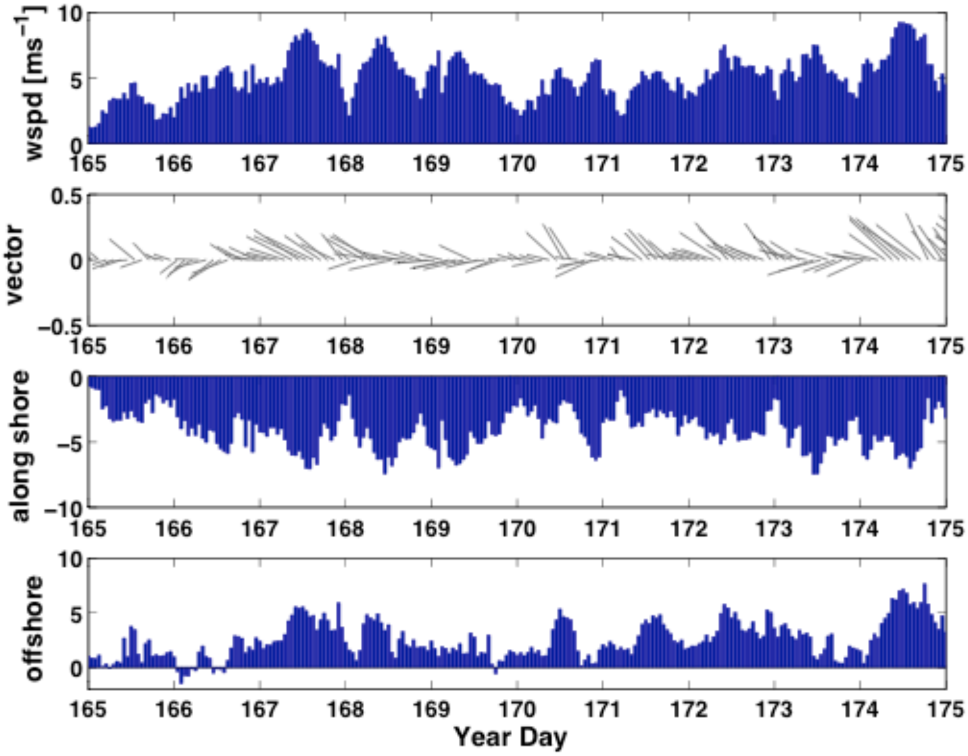

Figure 4.2 A typical wind sample time series. The first panel (top) is wind speed converted to 10m heights. The second panel shows the vector wind. The third panel is the wind component along the shore, where positive is to the east of the shoreline. The fourth panel is the wind component in the directions perpendicular to the shore, where positive is offshore.

### 4.1.2 Tides at Little Cayman

The tidal elevation in Little Cayman is recorded by the CTD depth gauge, or can be calculated by low passing the pressure measurements from the additional loggers. It is found that Little Cayman has a tidal range of less than 0.4 meter, and has mixed semi-diurnal and diurnal tidal components, where the semi-diurnal tidal components is slightly dominate.

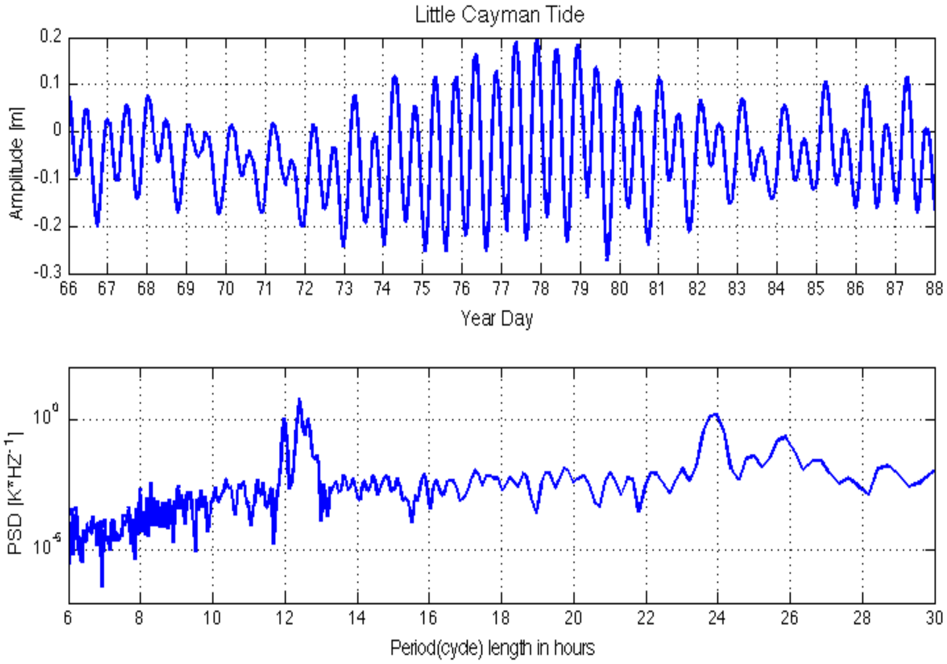

Figure 4.3 A sample series of tidal amplitudes at Little Cayman and the tidal spectra. In the spectra plot, the semi-diurnal peaks correspond to principal lunar semidiurnal component M2 which has a cycle of 12.42 hours and principal solar semidiurnal component S2 which has a cycle of 12 hours; while the diurnal peaks correspond mostly to lunar diurnal component K1 which has a cycle of 23.93 hours and lunar diurnal component O1 which has a cycle of 25.82 hours.

### 4.1.3 Extracting wave information from pressure measurements

No direct wave measurements were specifically collected at Little Cayman station. However, the 6-minute resolution pressure measurements from the four newly installed loggers revealed some pressure perturbations, which appeared to be related to the wind speed, and decay with depth. Using the linear gravity wave theory, wave information such as significant wave height, wave number and period could be derived from these pressure perturbations.

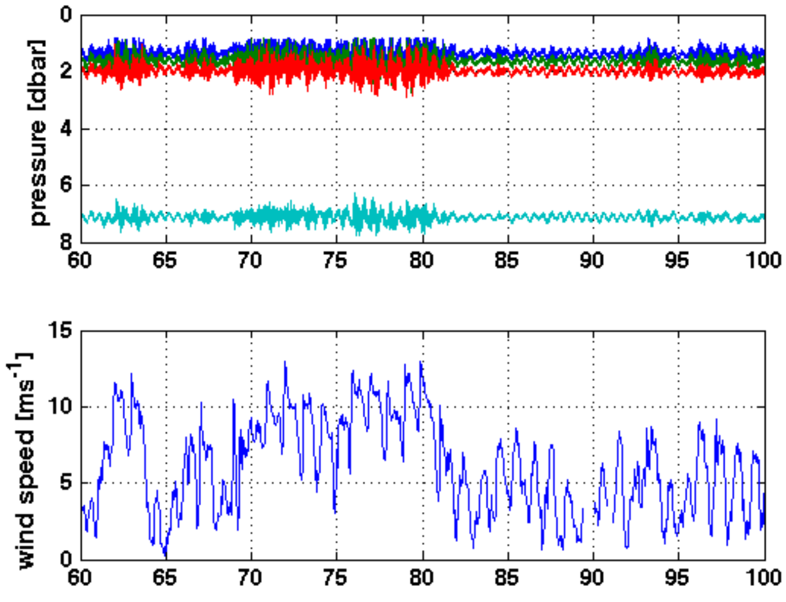

Figure 4.4 Sample time series of pressure measurements from four loggers and the corresponding wind measurements. X-axis is the day of the year in 2011.

The procedure to calculate the waves is as follows.

First, the tidal influence in pressure perturbations was removed by high passing the pressure data at all four depths, cutting off frequencies with periods longer than 6 hours. Second, 6-minute resolution data were split into hourly segments, so that each segment had 10 data points. The rationale of creating hourly ensemble instead of individual data points was that the measuring time of the pressure was not synchronized between the depth gauges. Therefore, instantaneous vertical profiles of wave induced pressure fluctuations could not be obtained. Instead, one hour long ensembles of pressure fluctuations were used to obtain estimates of pressure standard deviation at each depth. Third, waves were assumed to be linear and monochromatic, i.e., have a constant wave number k and wave amplitude a within each one hour segment. According to the linear wave theory (Kundu, 2002, page 204), at depth z, the pressure perturbation caused by waves is

$$p' = \rho ga\frac{\cosh k(-z+H)}{\cosh kH}\cos(kx-wt) \qquad \text{equation 4.1}$$

where p’ is the pressure perturbation, $\rho$ is density of the sea water, 1025 kgm$^{-3}$ at 25°C g is gravitational acceleration rate of 9.8ms$^{-2}$, a is the wave amplitude, k is the wave number, and z is the distance between the measurement and water surface, which was assumed to be constant within each hour, but changed on longer time scale due to tides. The total water depth H was also updated every hour due to tidal fluctuations.

Using the 10 data points within each hour, standard deviation was calculated for both sides of equation 4.1. As one hour is many times longer than the typical wind wave period of several seconds, the standard derivation of a cosine wave within the hour is $\frac{1}{\sqrt{2}}$. Thus for each depth and within each hourly segment

$$std(p_i') = \rho ga\frac{\cosh k(-z_i+H)}{\sqrt{2}\cosh KH}\text{, i=1, 2, 3, 4} \qquad \text{equation 4.2}$$

Fourth, system of four equations at four depths (equation 4.2), has only two unknowns: surface amplitude a and wave number k, therefore the problem is over defined. Thus the top three logger measurements were averaged as follows:

$$\frac{1}{3}(std(p_1') + std(p_2') + std(p_3')) = \rho ga\frac{\cosh k(-z_{123}+H)}{\sqrt{2}\cosh kH} \qquad \text{equation 4.3}$$

$$std(p_4') = \rho ga\frac{\cosh k(-z_4+H)}{\sqrt{2}\cosh kH} \qquad \text{equation 4.4}$$

where $z_{123}$ is the average depth of the top three loggers (note, top three loggers are grouped close together, whereas the bottom logger is relatively isolated in depth), resulting in one equation for the top three loggers, and one equation for the bottom logger.

To solve for a and k, first a was eliminated by dividing equation 4.3 by equation 4.4

$$\frac{std(p_{123}')}{std(p_4')} = \frac{\cosh k(z_{123}+H)}{\cosh k(z_4+H)} \qquad \text{equation 4.5}$$

To solve for k, a numerical algorithm iterated values of k starting with zero, changing the iteration step by a factor of -0.5 every time the difference between LHS and RHS of equation 4.5 changed sign, until the difference was within the numerical error tolerance of 0.001. Once k was calculated, a could be derived from either equation 4.3 or equation 4.4.

Finally, for each hour, significant wave height Hs was calculated as four times the standard deviation of the surface elevation, i.e., $H_s = 4 * a * \frac{1}{\sqrt{2}}$. The wave period was calculated using finite depth wave dispersion relationship $T = \frac{2\pi}{\sqrt{gk \tanh KH}}$. Finally, wave steepness ak, defined as a product of wave amplitude and wave number, was calculated to check if resulting waves have realistic properties. Most of the wave steepness falls within 0.1, and occasionally reaches 0.15 or 0.2, which is expected for young waves (Toba 1972) in case of offshore wind, or shoaling waves in case of onshore wind. There was a clear relationship between the significant wave height and wind speed (Fig 4.6).

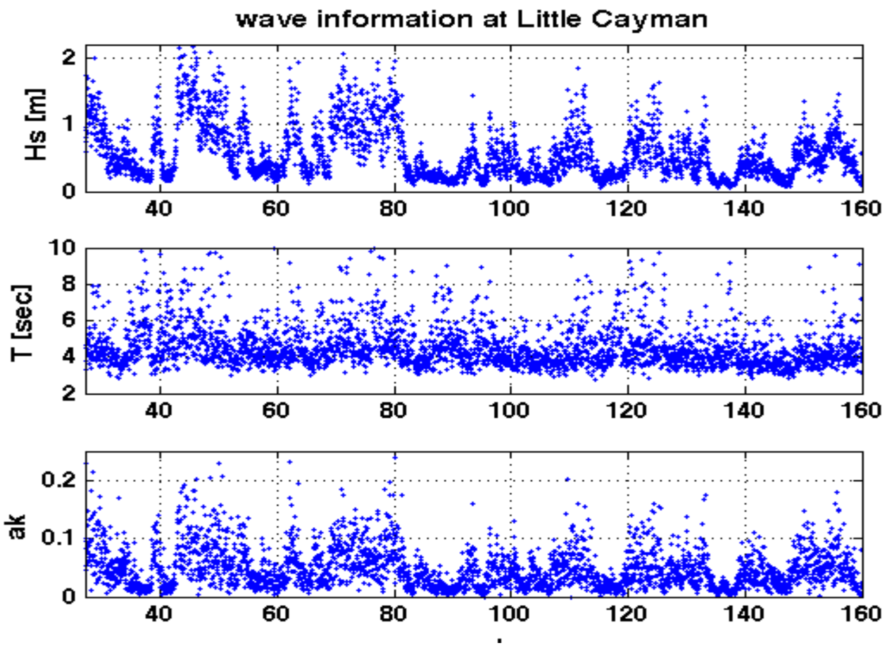

Figure 4.5 Sample time series of significant wave height $H_s$, wave period $T$ and wave steepness *ak* at Little Cayman station.

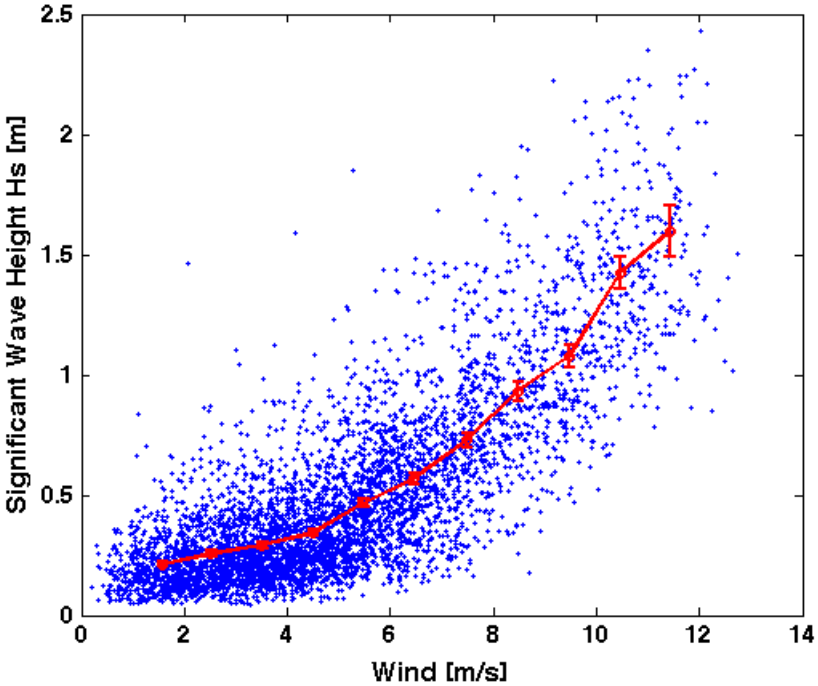

Figure 4.6 Significant wave height versus wind speed. The red line is the bin-averaged value for the significant wave height for each 1 $ms^{-1}$ wind speed bin with 95% confidence error bar plotted.

## 4.2 Little Cayman temperature data

Since January 2011, Little Cayman station LCIY2 had five water temperature measurements at different depths on the pylon. Three self-recording thermometers were added close to the surface at an average depth of 1.3 m, 1.5 m and 2 m, and another logger was added 0.1 m above the water bottom at an average of 7.1 m. In addition to the original CTD at 4.6 m depth, this 5-point setup facilitates the study of warming signatures at different depths, the vertical thermal profile evolution throughout a day, as well as provides data to test models of the shallow-water diurnal heating.

### 4.2.1 Addressing the calibration drift in the temperature data

Before processing the temperature data, it is important to evaluate the data quality and address any issues related to the data quality. A simple plot of temperature time series at different depths showed a clear daily warming pattern at all depths. It also revealed time-dependent discrepancies in the additional temperature time series, which gradually worsened with time.

An example of the unrealistic temperature time series from the additional temperatures is shown in Fig. 4.7. Of the top three loggers, positioned at depths ranging from 1.3m to 2m, the highest temperatures were constantly measured by the second logger at 1.5m, both during the day and at night; this is unlikely to occur due to the thermally induced convective instability. The night-time temperature measurements are more revealing: the temperature at 1.3m and 2m are significantly lower than at 1.5m, 7.2m and 4.6m, first by about 0.08 K during day 85 through 88, then by about 0.2K during day 229 through 232. This is clearly not physical, and requires correction.

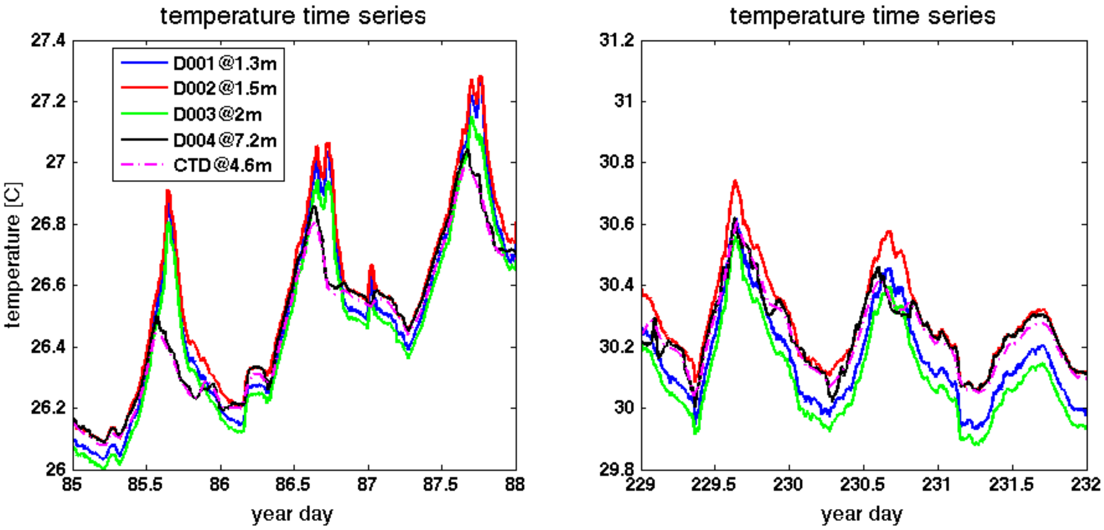

Figure 4.7 Sample time series of temperature measured at the Little Cayman station. The x-axis is the year day of 2011.

We used the CTD measurement at 4.6 m as the reference because the instrument is of much higher quality, and is expected to be much more reliable and accurate. Also, at this particular site, the CTDs were switched out and factory-calibrated every half a year. We addressed the apparent calibration drift according to two physically plausible criteria: Firstly, the temperature should be lower at deeper depths for most time, at least within the uncertainties of the measurements. Temperature inversions might occur during individual cases such as active mixing driven by strong wind or by salinity compensation, but on average should not exist. Secondly, diurnal warming from the previous day is expected to be erased by convective instability driven by surface cooling, and the water column should be well mixed before the next sunrise on average.

Firstly, the CTD data were linearly interpolated to 6 minutes resolution to match the resolution of the additional thermometers. Also, a 30 minutes time shift was applied to CTD data as the time stamps were recorded at the end of each measuring hour, and the stored values is an estimate of the average samples. Based on the second criteria, CTD measurement at 5am was subtracted from temperature measurements at 5am from other loggers. For loggers with accurate reading and no calibration drift, the difference should remain zero. Downward trends were found in the data from loggers 1 and 3. For loggers 2 and 4, the trend was more invariant, but there was a small offset. The time dependences were represented by a linear fit and corrections were applied to the original data (Fig 4.8 and Table 4.1). After applying the corrections, the temperatures at different depths were more physical and no temperature inversions were visible (Fig 4.9).

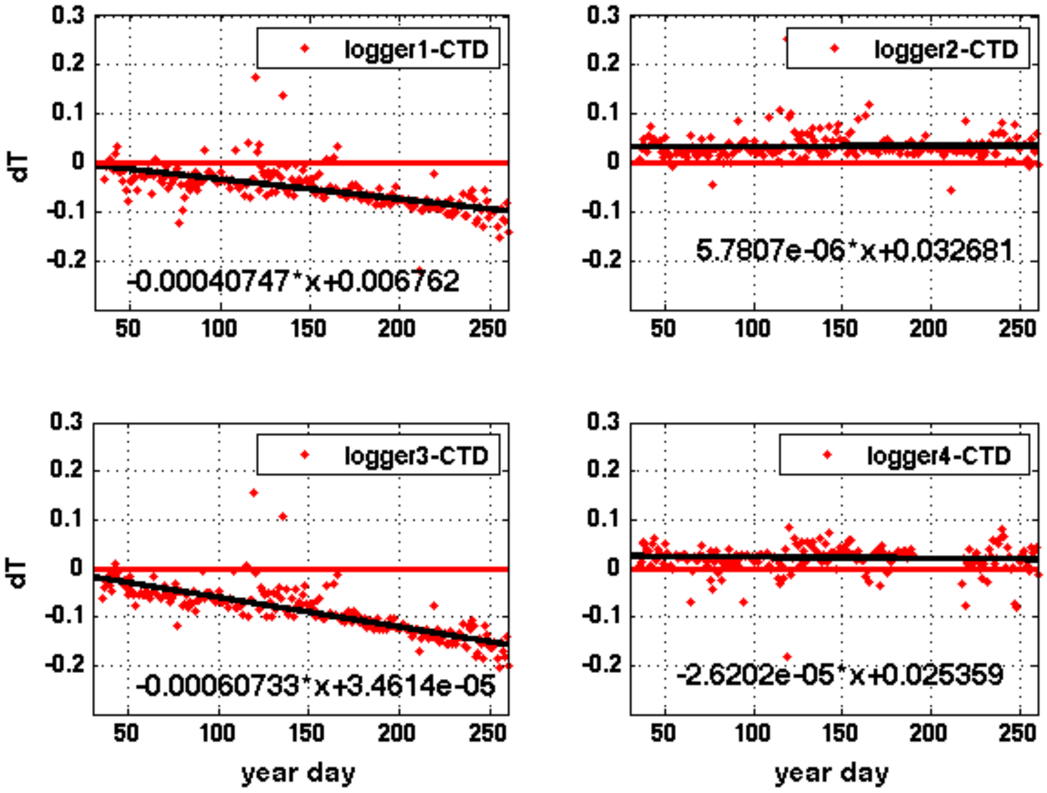

Figure 4.8 The temperature differences between the loggers and CTD measurements at 5am local time everyday are shown as red dots. Their linear fit lines are shown in black. The x-axis is day of year in 2011. The y-axis is temperature difference.

| Temperature drift $\Delta T$ | logger 1-CTD | logger 2-CTD | logger 3-CTD | logger 4-CTD |
|---|---|---|---|---|
| slope A (K/day) | -4.0747e-4 | -5.7807e-6 | -6.0733e-4 | -2.6202e-5 |
| intercept B (K) | 6.762e-3 | 3.2681e-2 | 3.4614e-5 | 2.5359e-2 |
| rms of residual (K) | 0.0322 | 0.0292 | 0.0298 | 0.0298 |

Table 4.1 Coefficients to correct the calibration drift from the self-recording thermometers. Temperature drifts can be calculated as $\Delta T = AX + B$, where X is the elapsed time in days from 2011-01-01 00:00 in local time. The new logger data is calculated as $T_{NEW} = T_{original} - \Delta T$

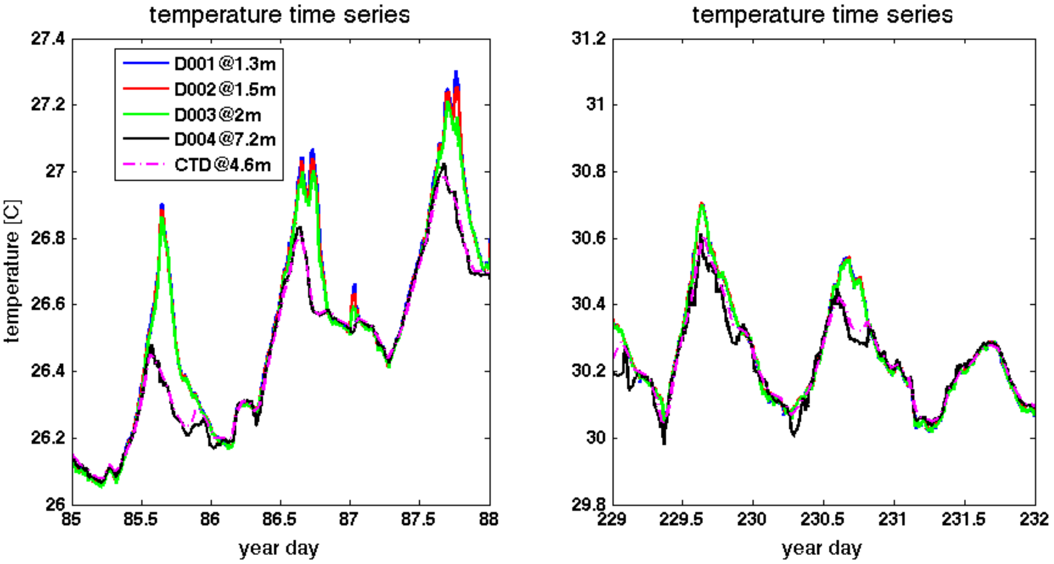

Figure 4.9 Same sample time series as in Fig.1 at Little Cayman station, but after the calibration drift correction has been applied. The x-axis is the year day in 2011.

### 4.2.2 Daily warming statistics

Data from a total of 189 days were analyzed from early February to late September in Little Cayman after days with missing data from either temperature data or weather measurements were removed. Daily average temperature time series showed an obvious daily warming pattern at all five depths. The daily averaged lowest temperature occurred at 7:00 LT (Local Time), and daily averaged highest temperature occurred at 15:00 LT at all depths. The top three loggers from 1.3m to 2m depth had an average of about 0.5K warming with slight stratification (~0.03K) between these levels, while the warming from

4.6m and 7.2m had about 0.3K average warming and were very similar in the daily progression. Using logger measurement at the shallowest 1.3m depth, we also examined the distribution of the timing when the daily maximum and minimum were reached (Fig 4.11).

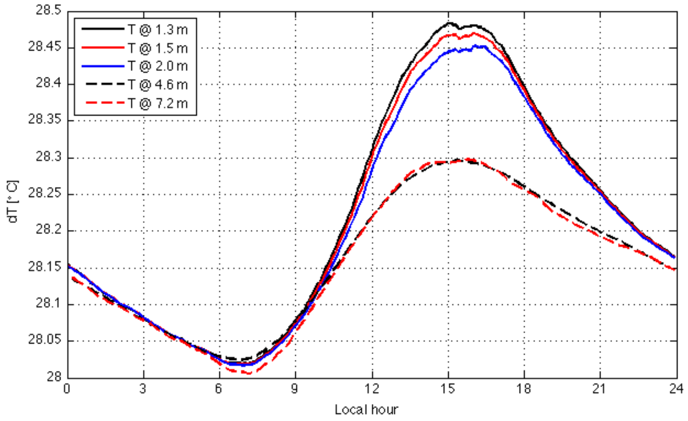

Figure 4.10 Temperature on an average day at different depths at Little Cayman station. The data length is from January 25th, 2011 to September 26th, 2011.

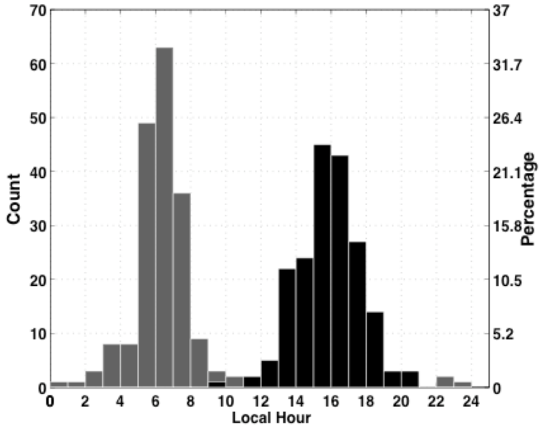

Figure 4.11 Histogram of the local time when daily maximum (black bar) and minimum (gray bar) are reached for the surface logger at depth 1.3m. The x-axis is the local hour. Y axis on the left is the number of the days, while y axis on the right is the percentage of days.

### 4.3 Relationship between daily warming and environment data

The strength of the Little Cayman data of course, was the availability of temperature profile measurements, as well as the onsite weather data including wind speed, insolation, humidity and rain. The 6 minute-resolution depth measurements also captured sub-tidal undulation of the water surface, thus provided some information of waves. So this section we study the relationship between the diurnal warming and various environmental parameters.

### 4.3.1 Case studies

In this section we chose several example days to illustrate the evolution of warming at different depths, and how the warming is related to environmental influences. The first four cases illustrated four days from summer months, with very similar amplitude of insolation, and quite different wind patterns throughout the day (Fig 4.12). The last two cases illustrated a cloudy day and a heavy rain day (Fig 4.13). The warming at 6:00 each day is referred to be zero.

Case (a). Strong insolation, weak steady wind.

Day 221 had weak and steady wind speeds (3~4ms$^{-1}$) throughout the day. The warming amplitude was 1.8K at the near surface logger, with a temperature difference of 1.3 K between near surface depths and the bottom, one of the largest ever recorded in this dataset. The temperature difference also started to develop as early as 10:00 as the weak wind was not sufficient to mix the heat down as the insolation increased. The warming was not completely erased at 6:00am next day due to the weak wind speed throughout the night.

Case (b) Strong insolation, diurnal breeze wind pattern

The wind during day 196 was quite typical at the coastal stations, where wind speed reached its peak in the early afternoon. Compared to case (a), the temperature difference between top and bottom loggers was much weaker (<0.5K), and occurred only after noon time. The near surface warming was much less than the steady weak wind case (0.8K vs. 1.8K), but the mid-depth CTD and bottom temperature actually showed similar warming of 0.5K compared to the weak wind case. The wind increase the surface fluxes significantly due to the increase in latent heat fluxes. A difference of more than 100 $Wm^{-2}$ in outgoing fluxes resulted as the wind increased from $3ms^{-1}$ to $6ms^{-1}$. The weak wind throughout evening and night only erased vertical temperature differences around 21:00, and there was still residual warming next day at 6:00.

Case (c) Strong insolation, alternating wind speed

Day 185 showed the warming pattern changed rapidly as the wind speed changed from weak to intermediate strength. A very weak morning wind allowed the vertical temperature difference to start developing as early as 9:00am, and the surface warming was 0.5K near surface at noon with obvious temperature difference between the surface loggers. The warming near the surface started to decrease when the wind started to increase also the solar radiation is reduced a little possibly due to clouds, and by 14:30, the temperature differences among near surface loggers were erased as wind reached a local peak of $5ms^{-1}$. Note that the mean wind on day 185 was $3.11ms^{-1}$, smaller than that in the first case on day 221. But stronger instantaneous wind in the early afternoon caused the resulting warming to be much less than day 221. This case illustrated the quick response of warming to changing wind speed. Also note that there is a rainfall event at night, which resulted in a slight temperature inversion.

Case (d) Strong insolation, strong wind, and rough surface

Day 235 had quite strong wind throughout the day, from up to $9ms^{-1}$ at previous midnight, to a steady $6\sim7ms^{-1}$ until next morning. No vertical temperature difference was developed due to the strong wind. It was interesting to notice the large wave amplitude captured by the depth measurements at the surface logger, which suggested possible mixing by waves in addition to wind.

Case (e) Cloudy day, weak wind speed

Day 199 was very cloudy with the maximum insolation of just over 500 $Wm^{-2}$, the wind was very weak (~2.5$ms^{-1}$) in the morning and reached its maximum around 4$ms^{-1}$ at noon. Because of the weak insolation, such a weak wind was sufficient to keep the water column well mixed. In the late afternoon, however, around 16:00, the wind speed relaxed and decreased to 2$ms^{-1}$ again. Vertical temperature difference of 0.2K immediately developed despite the very weak insolation, and remained until 18:00 when insolation decreased to zero.

Case (f) Cloudy day, heavy precipitation

As the shallowest logger we had was below 1m, only heavy rain effects could be captured in the temperature measurement. Day 156 had very weak insolation, intermediate wind speed and a rough surface, so the warming amplitude and vertical temperature difference was minimum. As rain is colder than the air, and the water at the sea surface (the wet-bulb temperature of the atmosphere, e.g. Gosnell et al 1995), the heavy rainfall around 15:00 caused the temperature measurement near surface loggers and CTD measurement to decrease, and a maximum thermal inversion of -0.4K were developed right after 15:00.

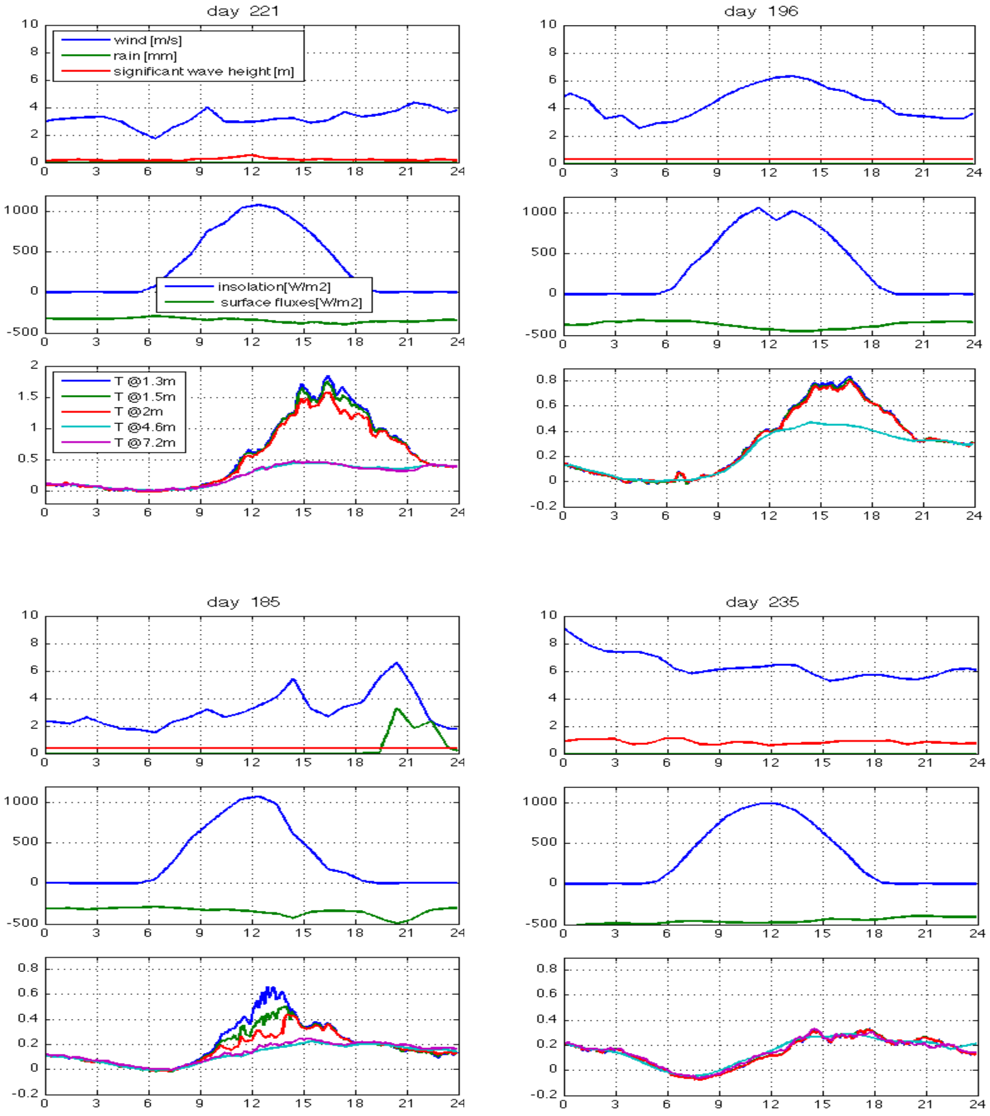

Figure 4.12 Four days with strong insolation and different wind patterns. The first panel shows the time series of temperature at different depth. The surface logger located at 1.3m, 1.5m, 2m, CTD located at 4.6m and bottom logger located at 7.2m are shown as red, green, blue, cyan, black lines respectively. The second panel shows wind speed and insolation. The third panel shows surface fluxes from atmosphere to ocean calculated from weather measurement. The SH (sensible heat flux), LH (latent heat flux), and LW (net longwave radiative flux) are shown in blue, red and green line respectively. The fourth panel is hourly rainfall amount in mm. The fifth panel shows 6 minute resolution depth measured by the shallowest surface logger, as well as wave height derived from the surface logger depth measurement. Note the different temperature scale in the first panel.

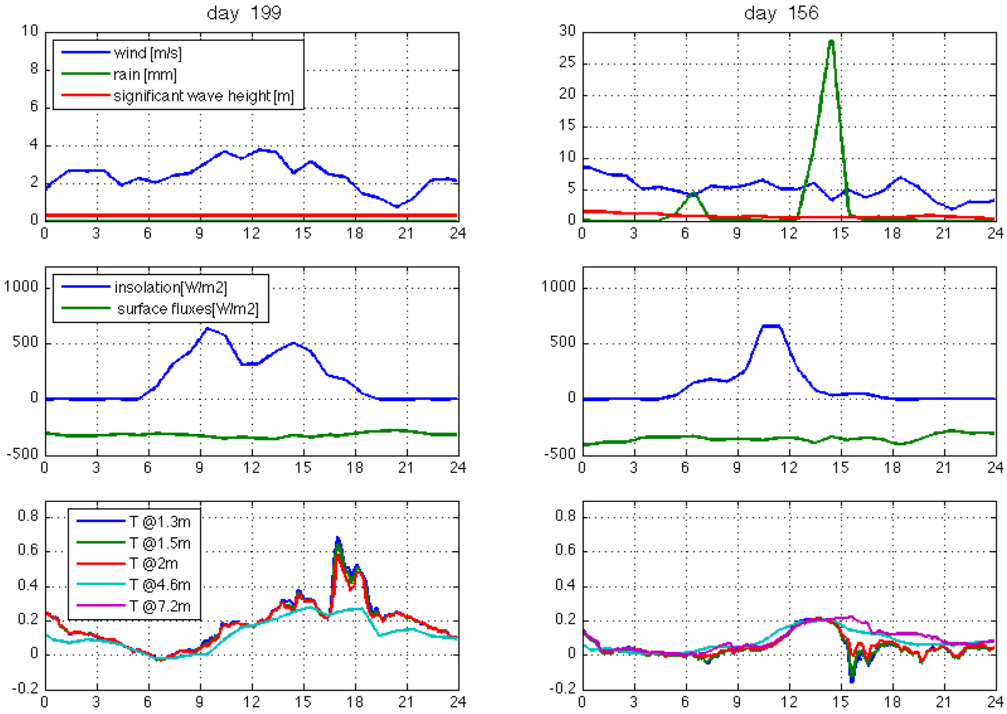

Figure 4.13 Two days with weak insolation without and with precipitation.

### 4.3.2 Linking daily warming amplitude with daily average wind and daily maximum insolation

The daily warming amplitude combined with an assumption of the daily surface warming curve shape is often a decent estimate of actual diurnal warming evolution. For this reason, simpler diurnal models often calculate the daily peak warming or warming curves as a function of daily averaged wind and daily maximum insolation and sometimes maximum precipitation (e.g. Webster, Clayson, and Curry 1996, Gentemann et al. 2003). In this section temperature and weather data at Little Cayman were explored to link daily peak warming and daily values of wind and insolation.

Daily peak warmings were calculated by subtracting daily minimum temperature from daily maximum temperature, while a day was defined to start from local time 6:00 to next day 6:00. By the same token, daily mean wind speed and daily maximum insolation were calculated.

First we studied the relationship between the peak warmings at a certain depth and wind speed as well as insolation (Fig.4.14 top two panels). The daily warming amplitude at the shallower depth had a clear relationship with the daily mean wind speed (correlation coefficient r=-0.40). Days with largest warmings (e.g. larger than 1.2K) all occurred during days when mean wind speeds were less than 6ms$^{-1}$. The daily maximum insolation (shown as color of the data points) also influenced the warming (correlation coefficient r=0.34). For most of the days where maximum insolation was less than 700Wm$^{-2}$(green and blue dots), the warming amplitudes were less than 0.4K , despite very low mean wind speeds on some days. For the deeper depth at 7.2 meter, influence of the mean wind speeds on the daily warming amplitude was much weaker (correlation coefficient r=0.28), the influence of the insolation was also weaker (correlation coefficient=0.22). It is interesting to notice the positive correlation between wind and warming amplitude at the bottom depth, which means stronger wind tend to transport the heat downward deeper, causing stronger heating at deeper depths. Thus wind is negatively correlated to warming at shallow depths and positively correlated to warming at deeper depth. The exact depth where this correlation changes sign is a very interesting question.

In addition to absolute warming values at certain depths, the thermal stratification at 16:00 between two different depths was calculated and its relationships between wind and insolation were shown. 16:00 was chosen as it was close to when the thermal stratification peak values were reached for most days. The thermal stratification is essentially an indication of how well water column is mixed and directly related to mechanical wind mixing, thus it was not surprising that there was a very clear relationship with the daily mean wind speed. Larger wind speeds were needed to mix the entire water column (Fig 4.14 bottom left panel) than the near surface water column (Fig 4.14 bottom right panel). When the wind speed was above 9ms$^{-1}$, the thermal stratification through whole water column was mostly zero. When the wind was above 4ms$^{-1}$, the thermal stratification near surface was mostly zero. Days with weak insolation values were shown to have smaller thermal stratification.

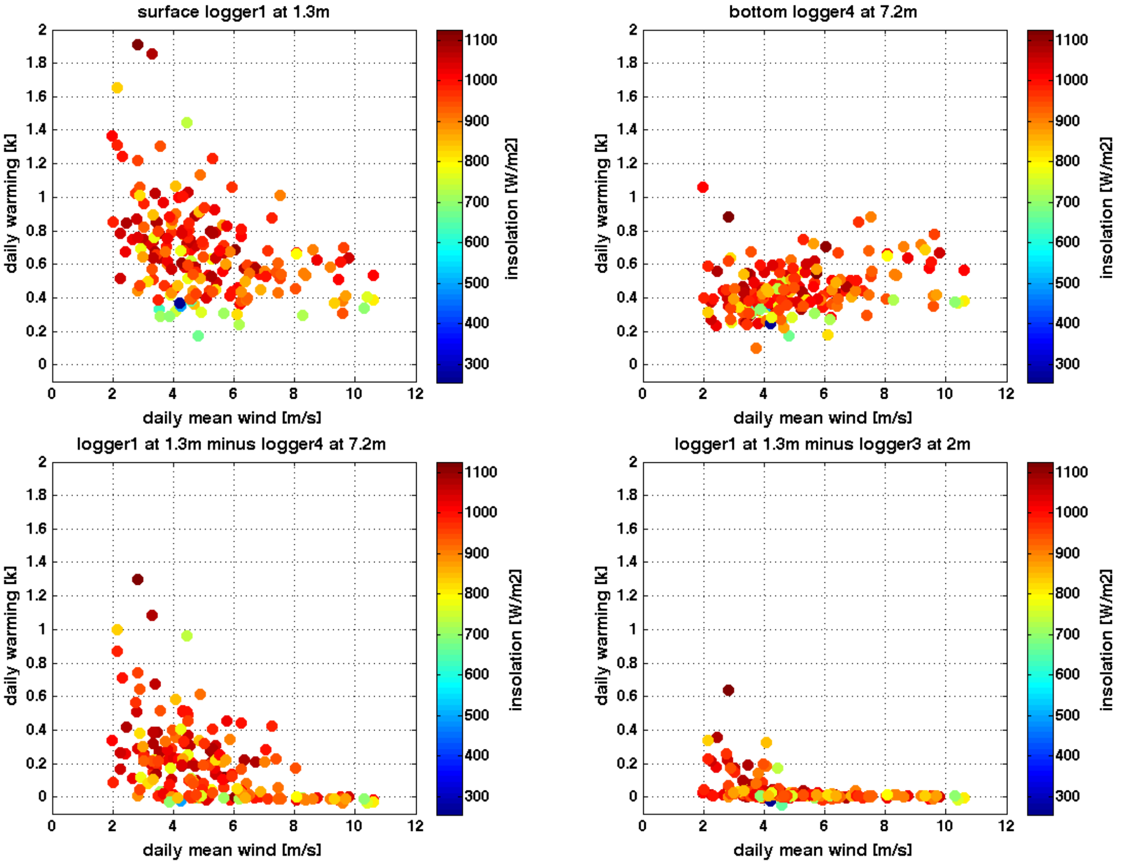

Figure 4.14 Scatter plots of warming and vertical temperature differences vs. daily mean wind and maximum insolation. The y-axis are respectively: a) daily maximum warming amplitude at 1.3m ;b) daily maximum warming amplitude at 7.2m; c) thermal stratification between 1.3m and 7.2m at 16:00 LT; d) thermal stratification between 1.3m and 2m at 16:00LT. x-axis is the daily mean wind speed in ms$^{-1}$. The color indicated the daily maximum insolation value.

### 4.3.3 What influenced the instantaneous thermal gradient and warming at Little Cayman?

In addition to the relationships between daily warming and the daily mean wind and daily maximum insolation, the case studies also illustrated that the instantaneous sub-surface thermal gradient responded rather rapidly to the environmental parameters, particularly to the instantaneous wind speed. A rapid increase or relaxation of the wind speed was often followed immediately by the disappearance (Figure 4.12, day 185) or re-appearance of the vertical thermal gradient (Figure 4.12, day 199).

In this section, we explore the relationship between the instantaneous thermal stratification of the water column and the instantaneous environmental parameters including wind speed, insolation, significant wave height, tide, etc.

In order to find underlying relationships and enhance statistical confidence, data obtained during various times of the day was combined using a normalization technique. Specifically, vertical thermal gradient $dT$ at any point in time was normalized by the thermal gradient during this time of the day, averaged over ~180 days available within the dataset. Here, thermal gradient $dT$ was defined as the temperature difference between the shallowest logger at 1.3m and the deepest logger at 7.2m. Examples of the averaged thermal gradient, as well as of absolute and normalized gradient values for a specific day were shown on Figure 4.15. A normalized value of smaller or larger than 1 at any given time indicated a smaller or larger than average thermal gradient for this time of the day. Relationship between such deviations and various external parameters indicated and quantified their effect on the vertical temperature profile. It is the goal of this section to investigate such relationships.

Figure 4.15 also suggested that typical difference between the two loggers (1.3 and 7.2 m) was very small in the morning and night (<0.05K), which resulted in large uncertainty of normalized thermal gradient. Therefore, only daytime data (from 11:00 to 22:00 Local Time) was considered in the following analysis.

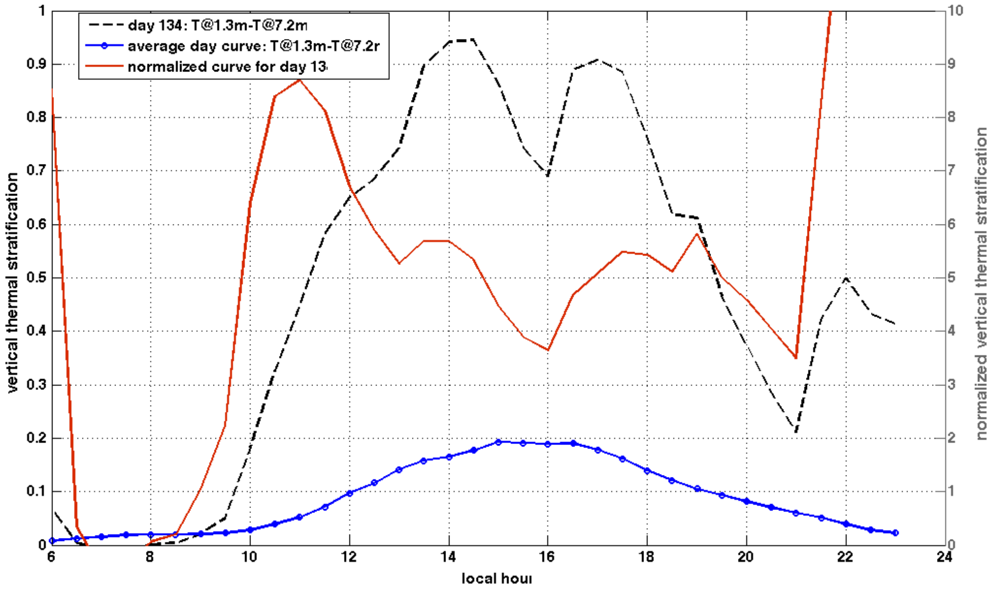

Figure 4.15 Example of how a sample day temperature is being normalized. The black dash line is the time series of the temperature difference between top logger and bottom logger on day 134. The blue line with '.' maker is the temperature difference between these two loggers on an average day. These two lines both use the left Y-axis [K]. The red line is the normalized thermal gradient on day 134, which is calculated by dividing the black dash line by the blue line with '.' marker. The red line uses the right Y-axis.

#### 4.3.3.1 Relationship of normalized thermal gradient and wind speed

The instantaneous wind speed was found to have a clear and immediate effect on the thermal gradient, regardless of the time of the day (Fig 4.16). The bin-averaged curve of normalized stratification versus wind speed showed that stronger wind speed resulted in weaker stratification, and vice versa. The gradient tended to be less than the average day value when the wind speed was larger than $5ms^{-1}$, and larger than the average value when the wind speed was less than 5ms$^{-1}$. It is notable that while the thermal gradient could be large or small during weak wind, it is necessarily well mixed in higher winds, independent of other external parameters.

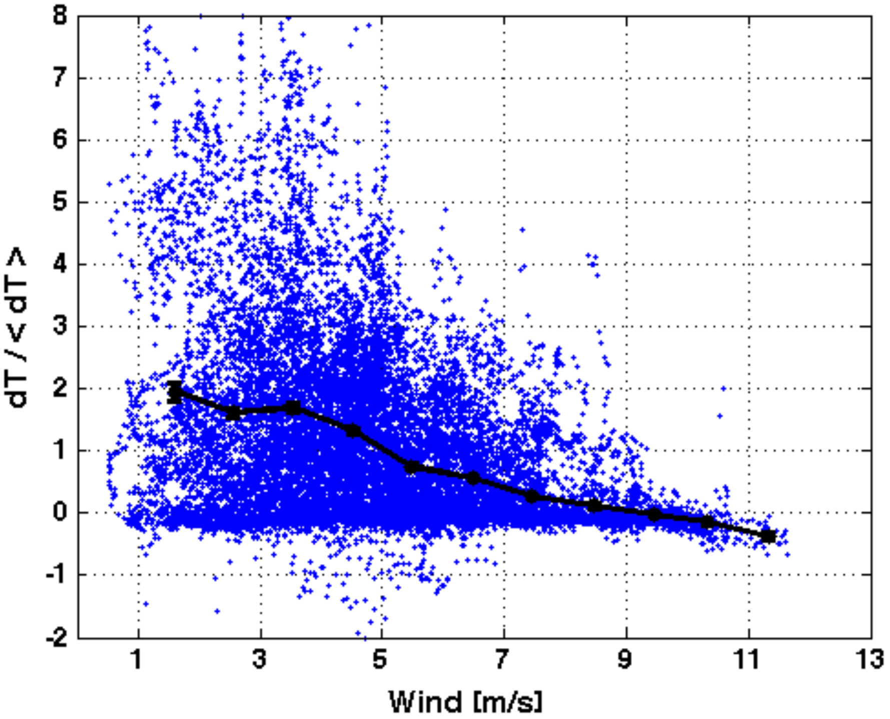

Figure 4.16 Relationship between thermal gradient and instantaneous wind speed. The wind speed is converted to 10m height. The black line consists of 1 ms$^{-1}$ bin-averaged values with 95% confidence intervals.

### 4.3.3.2 Relationship of normalized thermal gradient and insolation

Compared to the wind speed, instantaneous insolation had less effect on the instantaneous normalized thermal stratification. The bin-averaged stratification was around 1 for insolation values ranging from 0 to over 1000 Wm$^{-2}$ (figure 4.17). Note, while the absolute thermal gradient was expected to depend on the solar insolation, here much of this dependence was accounted for within the normalization factor, therefore it did not appear in the figure. It was, however, interesting to investigate if the wind-induced variability was affected by the insolation. Plotted along with wind, the instantaneous insolation was shown to have a secondary effect on the thermal stratification, in addition to the wind speed (Figure 4.18, left). For the same wind speed interval, a subset of points with insolation larger than 300 $Wm^{-2}$ produced consistently larger thermal gradients than data points with any insolation (relative difference as large as 0.7K at low wind speed), while a subset of points with insolation equal to or smaller than 300 $Wm^{-2}$ consistently produced a smaller gradient than average; except for the very strong wind case ($>11ms^{-1}$), where the stratification is very close to zero in both cases (Figure 4.18, right).

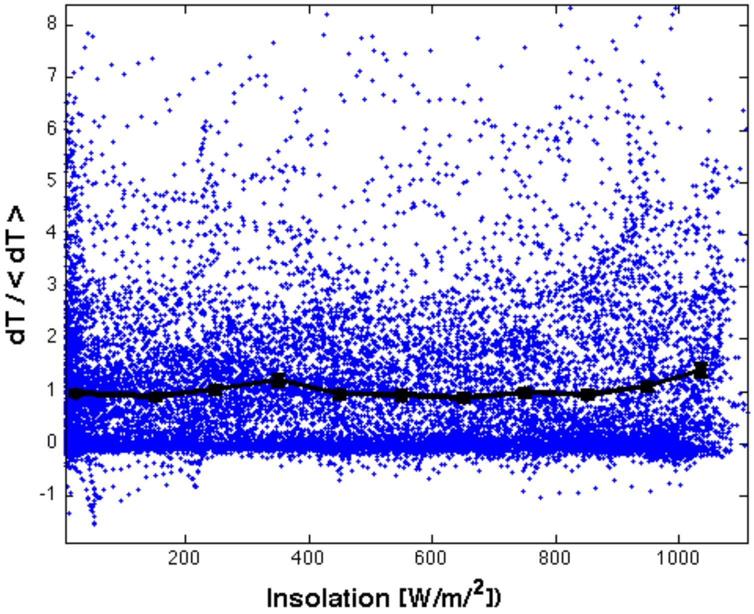

Figure 4.17 Relationship between normalized thermal stratification and instantaneous insolation. The black line is the bin-averaged value for the average stratification for each $100Wm^{-2}$ insolation bin. Error bars show 95% confidence intervals.

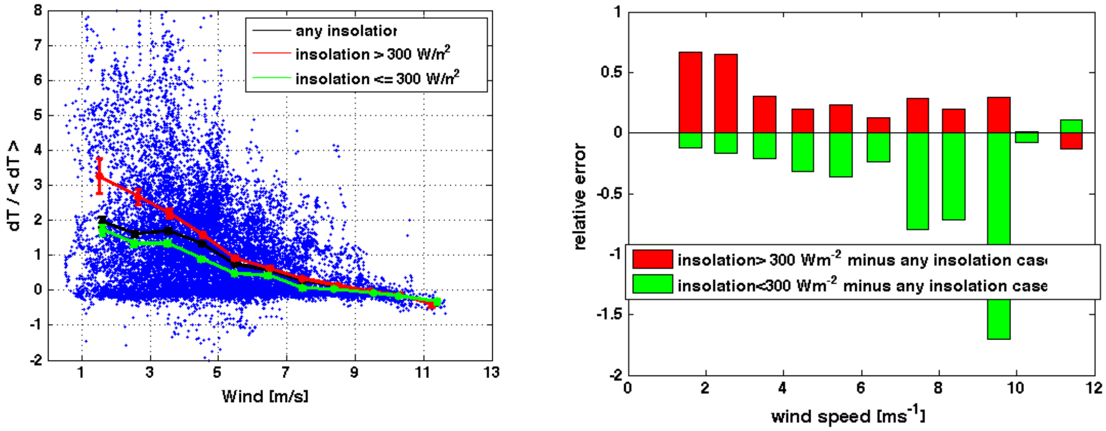

Figure 4.18 Dependence of normalized thermal gradient on instantaneous wind speed and insolation. In the left panel, the black line is the bin-averaged normalized stratification for each 1 ms$^{-1}$ wind speed bin with 95% confidence error bar plotted. The red line is the bin-averaged normalized thermal gradient versus wind for data points with instantaneous insolation of larger than 300 Wm$^{-2}$. The green line is the bin-averaged normalized stratification versus wind for data points with instantaneous insolation smaller than or equal to 300 Wm$^{-2}$. In the right panel, red (green) bars refer to relative differences of bin-averaged values (left panel) between the high (low) insolation curves and the overall average curve.

#### 4.3.3.3 Relationship of normalized thermal gradient and significant wave height

Next the relationship between the significant wave height (SWH) and the normalized thermal stratification was explored. Since SWH were related to wind speeds (Figure 4.6), the wave effect on normalized stratification was separated from wind effect by grouping points with similar wind speed and different SWH. For each data group binned within 1ms$^{-1}$ wind speed range, bin-averaged normalized thermal gradients were calculated for the largest 25% and the smallest 25% of the significant wave heights.

The SWH clearly influenced the normalized stratification when the wind speed was intermediate to strong (5ms$^{-1}$ to 12ms$^{-1}$). For the same wind speed interval, a subset of points with the smallest 25% of SWH produced a larger normalized stratification than data points with any SWH, while a subset of points with the largest 25% of SWH consistently produced a smaller normalized stratification. The relative difference was largest for intermediate wind of 5ms$^{-1}$ to 10ms$^{-1}$(Figure 4.19, right panel).

For very strong wind (>10ms$^{-1}$), the relative difference decreased, indicating that the influence of SWH decreased. Evidently, at this wind speed, the strong wind alone was able to result in a well-mixed water column, thus added wave mixing could not influence stratification further. Similarly, at low wind speeds additional effect of waves was not found to be significant as the SWH tended to be small (Figure 4.6).

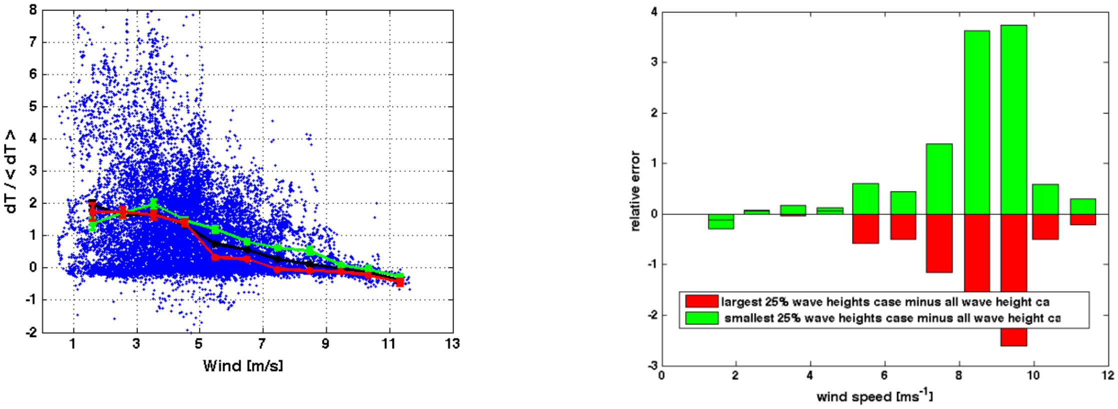

Figure 4.19 Dependence of normalized thermal gradient on instantaneous wind speed and significant wave height. The wind speed is converted to 10m height. In the left panel, the black line is the bin-averaged stratification for each 1 ms$^{-1}$ wind speed bin with 95% confidence error bars plotted. The red line is the bin-averaged stratification for the points with the largest 25% of the significant wave heights for each 1ms$^{-1}$ wind speed bin. The green line is the bin-averaged stratification for the points with the smallest 25% of the significant wave heights for each 1ms$^{-1}$ wind speed bin. In the right panel, red (green) bars refer to the relative difference of bin-averaged normalized thermal gradient between the largest (smallest) 25% significant wave height subset, and the overall average curve (see left panel).

#### 4.3.3.4 Relationship of normalized thermal gradient and tidal phase

In this section, the influence of tide on the normalized thermal gradient is explored. The key question is whether the normalized thermal gradient is related to the phase of the tide. The instantaneous phase angle could be calculated by performing the Hilbert transform on the tide elevation time series. Hilbert transform converts a real data sequence xr into a complex helical sequence called the analytical signal x=xr+i*xi, where the real part is the original real data, and the imaginary part xi is the original real sequence with a 90° phase shift. The instantaneous phase angle then could be calculated as angle of the complex number x. Comparing a sample time series of the tidal elevation and resulting phase angle time series (Figure 4.20), it was shown that the zero angle corresponded to the high tide, while ±180° corresponded to the low tide, for a day with clear high tide and low tide peaks.

Using similar bin-average approach, it was found that the normalized thermal gradient was close to 1 for most of the tidal phases, indicating tidal phase had a rather minor effect (Figure 4.21). There was, however, a slight decrease shortly after high tide (zero phase angle) and a slight increase shortly after low tide (-180 phase angle) in normalized gradient. The largest negative deviation from 1 occurred when the phase angle was about 45 degree, i.e. shortly after the high tide, where the normalized stratification was around 0.7. This could be explained by the fact that the warming tended to be trapped close to the surface. Thus during high tide, thicker water column and larger thermal gradient existed between the water surface and shallow logger, resulting in decreased thermal gradient between shallow logger and the bottom logger. This tidal effect on the thermal gradient was not immediate; a rather significant lag existed. For a semi-diurnal tidal region with tidal period of about 12 hours, 45-degree phase lag equaled to 3 hours in time. The results also indicated that the tidal currents were not likely to be important for thermal gradient in this location. The strongest tidal currents, which usually occurred at ±90° phase angle (mid-water), would cause the thermal gradient to decrease due to increased turbulence mixing. However, this was not the case in the present dataset.

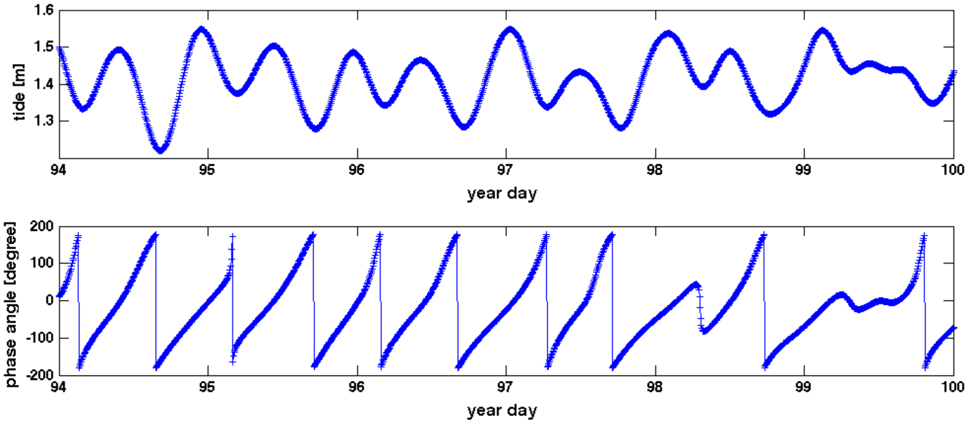

Figure 4.20 A sample time series of tidal elevation (top) and instantaneous phase angle (bottom), calculated using Hilbert transform.

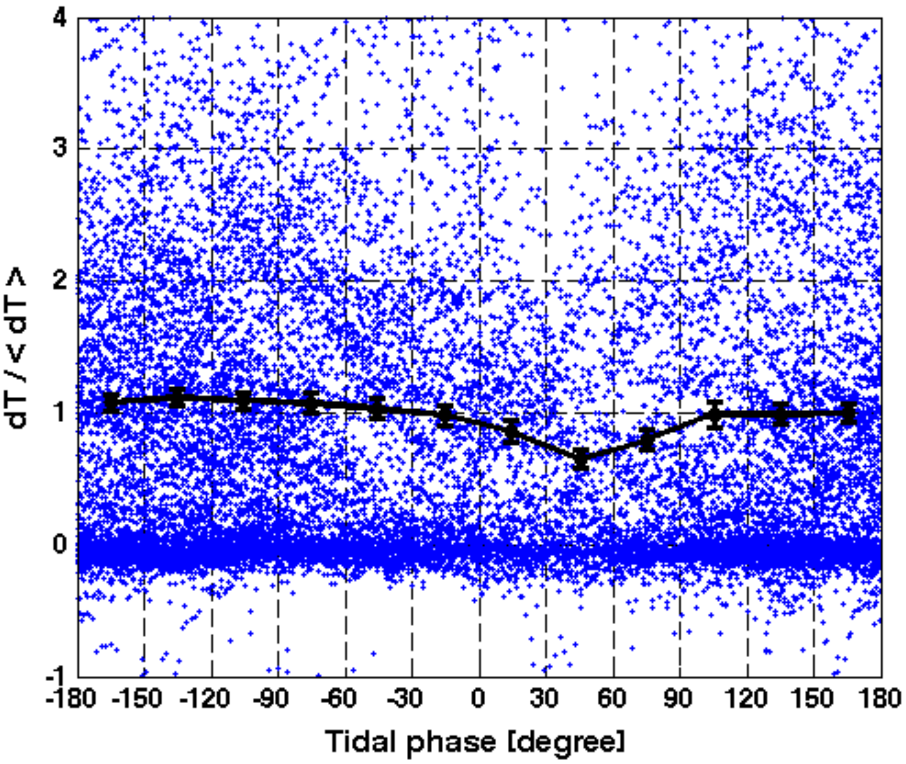

Figure 4.21 Relationship of normalized stratification versus phase of the tide

#### 4.3.3.5 Relationship of normalized thermal gradient and its previous values

Apart from the influence of environmental forcing, the normalized thermal gradient has strong inertia. Thus strong correlation exists between the thermal gradient and its previous value 30 minutes apart (Figure 4.22).

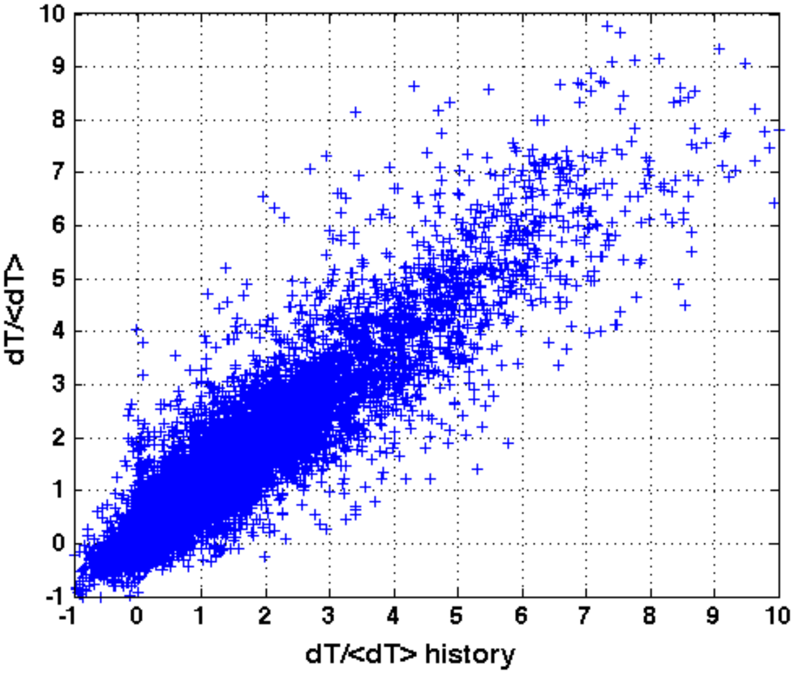

Figure 4.22 The dependence of the thermal gradient on its value 30 minutes ago.

It has been shown that instantaneous external parameters such as wind speed, wave height, solar insolation, and tidal phase are important for the immediate formation or destruction of the thermal gradient. However, it was also recognized that it took a significant period of time for the external forces to reconstruct the thermal gradient; therefore inertia has to be considered as one of key parameters. The influences which affect the thermal gradient could be ranked as follows: thermal gradient history> wind speed>wave/tide/insolation.

## 4.4 Concluding remarks

In this chapter, the Little Cayman station from Caribbean dataset is chosen for a more detailed analysis between diurnal warming characteristics and the environmental forcing. It is found that the daily maximum warming correlated with daily average wind speed positively near the surface, and negatively near the bottom, indicating downward heat transport during windy conditions. For the cloudy days, the warming amplitudes are smaller at both near surface and near bottom depths. In addition to warming relationship with ‘daily average/maximum’ forcing, this chapter further explored the relationship between the instantaneous thermal stratification of the water column and instantaneous environmental parameters including wind speed, insolation, significant wave height, and tide. The influences that affect the instantaneous thermal gradient could be ranked in the order of descending importance: the history of thermal gradient, the wind speed, and less importantly waves, tides, and insolation.

# Chapter 5 Great Barrier Reef dataset

In contrast to open ocean, coastal phenomena tend to exhibit more local characteristics. So in order to capture the general characteristics of the diurnal warming at coastal shallow waters, it is essential to study the phenomenon at many stations covering large spatial region and varying environmental characters. In this chapter, we study such a dataset from the Great Barrier Reef (GBR) region offshore NW Australia.

## 5.1 Locations, local physical environment and instrumentation

The Great Barrier Reef (GBR) is the world's largest coral reef system composed of over 2,900 individual reefs and 900 islands. The GBR region extends from 9 ˚S to 22 ˚S, stretching for over 2,600 kilometers along the northeast coast of Queensland, Australia (Figure 5.1). The east edge of the barrier reef is aligned with the continental shelf break, where the depth is about 100 m at the edge of the shelf. The coral reefs are very densely located in the northern part (north of about 16 ˚S), and cover most of continental shelf. South of 16 ˚S, the reefs are largely located on the outer half of the shelf. Moving southward, the reefs are located progressively further offshore and the reef densities vary from highly dense to sparse (Brinkman et al 2002, Wolanski and Spagnol, 2000). A shallow Great Barrier Reef lagoon separates the Queensland mainland from the barrier reefs offshore, and becomes wider from north to south (Luick et al., 2007). Inside the GBR lagoon, the depths are generally around 20 m near shore, increasing to 40–60 m on the outer shelf. The GBR lagoon is generally considered sheltered from the regional large-scale circulations due to the existence of the reef matrix and the shelf break.

However at the locations along GBR where the reef matrixes are sparse, cross-shelf inflow that transports water onto the shelf by the Eastern Australia Current (EAC) into GBR lagoon do occur (Brinkman et al., 2002).

Southeasterly trade winds prevail throughout most of the year (Wolanski, 1982). Unlike the Caribbean Region, the GBR region has large tidal ranges, ranging from 2 m in the northern region to about 8 m in the south (http://www.bom.gov.au/oceanography/tides/index_range.shtml). A 5-minute spatial resolution tidal range dataset was provided by Australia National Tide Center (Figure 5.2), and we obtained the tidal range for each study sites by performing 2- dimensional linear interpolation using this datasets. On the coral reefs of the GBR, the range is 2-5 m (Figure 5.2). The tides are mixed diurnal and semidiurnal lunar tides, except near the coast in the south, where the semidiurnal lunar tide dominates (Wolanski 1994).

The temperature dataset is comprised of a total of over 200 temperature loggers placed on the coral top, recording the bottom temperature every 30 minutes throughout Australia, mostly at GBR region .The earlier loggers only record water temperature; depths were also recorded from late 2008 onward (Berkelmans, personal communication). All loggers were placed directly among the coral communities that feature much higher bottom rugosity, i.e. small-scale height variations, compared to the ‘colonized pavement’ of the Caribbean stations. Depending on deployment locations and depths, the stations were named within three types. ‘Reef-flat’ sites refer to measurements taken from just below lowest astronomical tide level. ‘Reef-slope’ sites indicate measurement depths of 5 to 9 m while ‘deep reef-slope’ sites indicate depths of about 20 m. There are no co-located weather and light measurements at the logger locations.

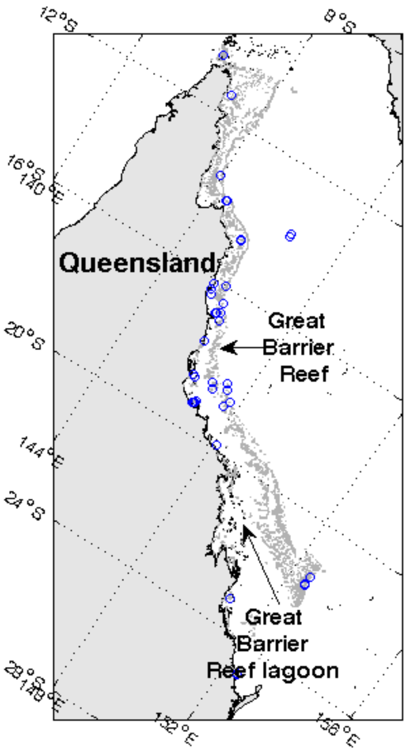

Figure 5.1 The area map of the Great Barrier Reef. The map shows the location of 65 out of 200 logger sites along the GBR, which were analyzed for a five-month period. The stations were shown in blue circles.

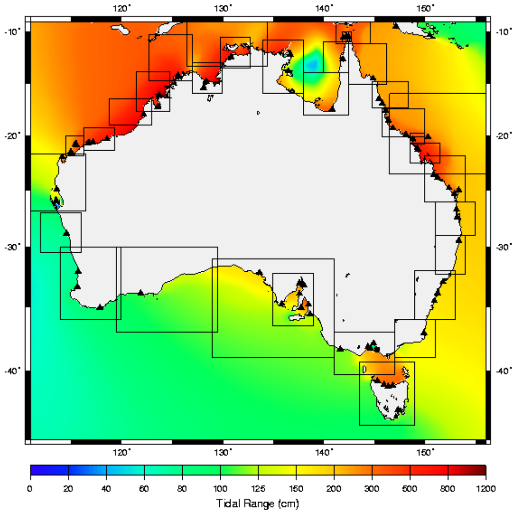

Figure 5.2 Tidal ranges offshore Australia.
(http://www.bom.gov.au/oceanography/tides/index_range.shtml).

## 5.2 Study period and method of analysis

For the diurnal warming analysis, 30-minute resolution water temperature data for a period of five months from November 1st, 2002 to March 31st, 2003 from a total of 65 bottom-mounted loggers were analyzed (see Figure 5.1). The period covers late spring to early autumn in the region. All time stamps have been converted to mean local time for each station according to their longitudes.

We first explore a few representative cases of diurnal warming patterns by examining the time series, diurnal warming statistics and temperature spectrum from sample sites. We next summarized the diurnal warming amplitude and timing for all stations. Last and most importantly, we categorize the stations into groups related to different geographic features, and explore how the diurnal warming characteristics and tidal influences depend on those features.

## 5.3 Results

### 5.3.1 Diurnal warming existence and characteristics: sample stations

The diurnal warming characteristics of four sample stations were chosen (Figure 5.3). For each station, we first visually inspect the temperature data series, and determine the existence of a daily cycle. Then daily maximum warming as well as the time when daily maximum temperature and minimum temperature were reached were calculated, to see if these characteristics align with those found in previous DW studies. Finally, spectrum analysis are performed on the temperature time series, values of $PSD_{M2}$, $PSD_{24}$ , and ($PSD_{M2}/PSD_{24}$) were calculated as described in Chapter 3.

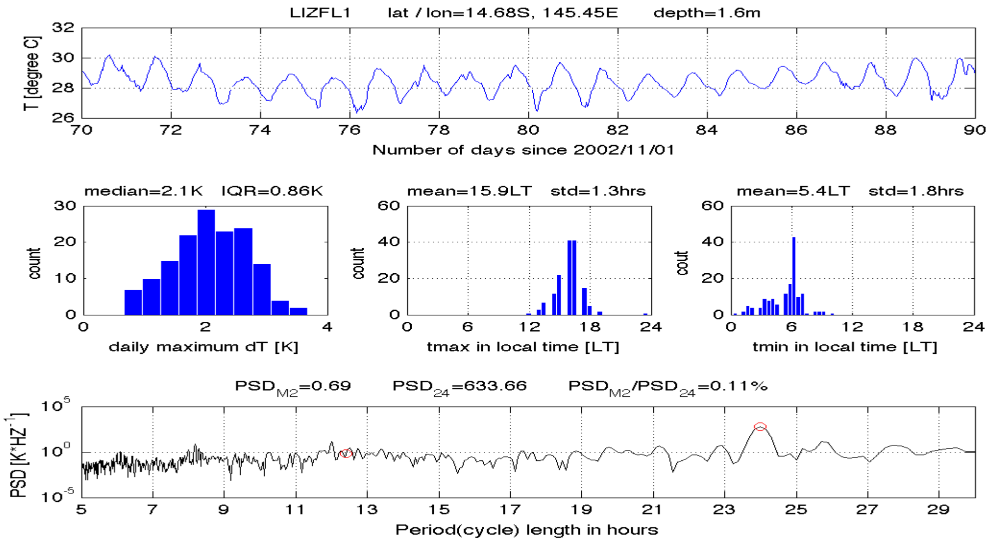
LIZFL1 lat / lon=14.68S, 145.45E depth=1.6m
T [degree C]
32
30
28
26
70
72
74
76
78
80
82
84
86
88
90
Number of days since 2002/11/01
median=2.1K IQR=0.86K
count
daily maximum dT [K]
mean=15.9LT std=1.3hrs
tmax in local time [LT]
mean=5.4LT std=1.8hrs
cout
tmin in local time [LT]
PSD$_{M2}$=0.69 PSD$_{24}$=633.66 PSD$_{M2}$/PSD$_{24}$=0.11%
PSD [K*HZ$^{-1}$]
$10^5$
$10^0$
$10^{-5}$
Period(cycle) length in hours

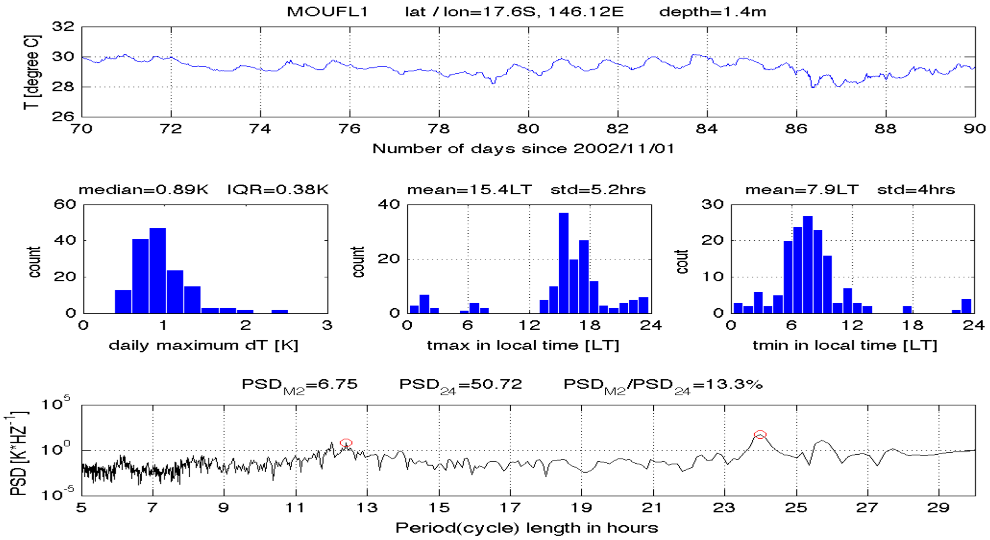
MOUFL1 lat / lon=17.6S, 146.12E depth=1.4m
T [degree C]
Number of days since 2002/11/01
median=0.89K IQR=0.38K
count
daily maximum dT [K]
mean=15.4LT std=5.2hrs
tmax in local time [LT]
mean=7.9LT std=4hrs
cout
tmin in local time [LT]
PSD$_{M2}$=6.75 PSD$_{24}$=50.72 PSD$_{M2}$/PSD$_{24}$=13.3%
PSD [K*HZ$^{-1}$]
Period(cycle) length in hours

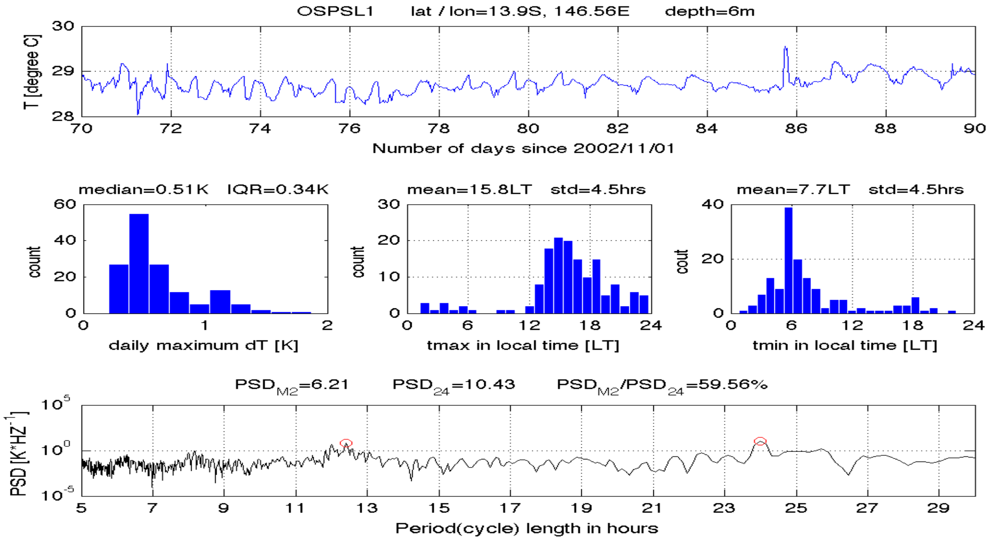
OSPSL1 lat / lon=13.9S, 146.56E depth=6m
T [degree C]
30
29
28
Number of days since 2002/11/01
median=0.51K IQR=0.34K
count
daily maximum dT [K]
mean=15.8LT std=4.5hrs
tmax in local time [LT]
mean=7.7LT std=4.5hrs
cout
tmin in local time [LT]
PSD$_{M2}$=6.21 PSD$_{24}$=10.43 PSD$_{M2}$/PSD$_{24}$=59.56%
PSD [K*HZ$^{-1}$]
Period(cycle) length in hours

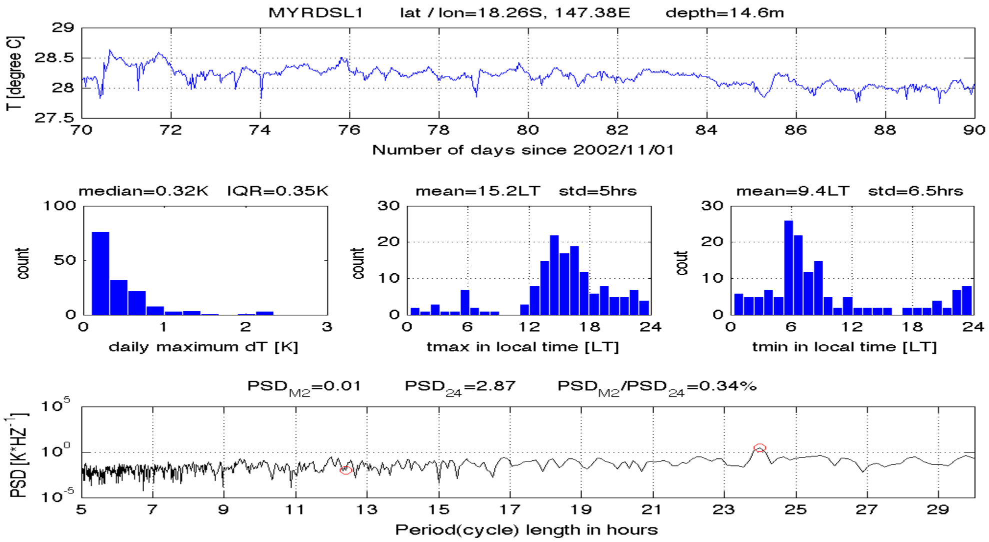

Figure 5.3 Characteristics of temperature measurements for four sample stations. The top panel is the temperature time series. Station latitude, longitude, average depth of the water column. The middle panel shows the histogram of the daily warming amplitude for the five-month time period (left plot), as well as the histograms of the local time when the daily maximum (center plot) and minimum (right plot) are reached. The bottom panel shows spectrum analysis results for temperature measurements. Solar component $PSD_{24}$ and tidal component $PSD_{M2}$ are marked with red circles.

The reef flat station at Lizard Island (LIZFL1) is a site with strong and clear diurnal warming patterns, where tides exhibit minimal influences. The histogram shows a median daily warming of 2.1K, and interquartile range (IQR, the value between first and third quartile) of 0.87K. Here robust statistics measures such as median and IQR are used instead of mean and standard deviation, as the daily warming amplitudes often do not have normal distribution. The mean local hours when daily maximum and minimum warming are reached are respectively at late afternoon (16.1LT) and early morning (5.5LT), similar to previous findings. Spectrum analysis shows a large $PSD_{24}$ of 633.66 $K\cdot Hz^{-1}$ and a weak $PSD_{M2}$ of $0.69K\cdot Hz^{-1}$, the ($PSD_{M2}/PSD_{24}$) ratio is only 0.11%. The Lizard Island site is inside the lagoon between the barrier reef and coast at the North section, where barrier reef is quite dense and the lagoon could be regarded as well sheltered.

The measurements at reef flat site at Mourilyan (MOUFL1) on the other hand exhibit a smaller daily warming cycle, and experience more tidal influence. The median daily warming amplitude is 0.89K, which corresponds to a smaller 24hr component in the spectrum plot ($PSD_{24}$=50.72K·$Hz^{-1}$). While there is still obvious warming during afternoon (mean tmax=15.4LT), there are frequently double peaks in the temperature time series indicating nighttime temperature increase (day 71 and day 88 in the time series for example). These double peaks are most likely caused by tide, as the M2 tide influence is quite strong at this site ($PSD_{M2}$=6.75K·$Hz^{-1}$). The relative influence of M2 tide vs. insolation ratio ($PSD_{M2}/PSD_{24}$) is over 13%. This large tidal influence might be explained by possible proximity of a tidal inlet. The Mourilyan site is at the coast, close to an opening (possibly a tidal inlet) of a mostly enclosed bay at the middle section.

Osprey Reef is the only station in our dataset that lies east from the GBR, i.e., off the continental shelf. At Osprey reef slope station (OSPSL1) where the water depth is 6m, insolation influence on temperature is weak ($PSD_{24}$=10.43K·$Hz^{-1}$), while tidal influence on temperature is relative strong ($PSD_{M2}$=6.21K·$Hz^{-1}$). Double peaks are frequently present in the temperature time series. Daily warming amplitude has a distribution close to exponential, and mean local time when daily maximum and minimum temperatures are reached are again late afternoon and morning, though the data have more spreads.

The Myrmidon Reef deep reef slope station (MYRDSL1) has a water depth of 20m. The insolation influence on temperature is very weak ($PSD_{24}$=2.87K·$Hz^{-1}$), and the tidal influence on temperature is even weaker ($PSD_{M2}$=0.01K·$Hz^{-1}$). The daily warming could still be detected as the daily temperature reached the maximum at a mean 16.95LT. However, the time when daily minimum temperature is reached become more evenly distributed. The distribution of the daily warming amplitude is exponential, i.e., majority of days have warming below 0.5K, and large warming events are rare. The Myrmidon Reef is located at middle section of the barrier Reef.

### 5.3.2 Warming statistics for all GBR stations

In this section, histograms of daily warming amplitudes and timings were plotted combining the 9815 daily data points from all 65 stations during the five-month (151 days) period. Overall distinct diurnal warming patterns with significant amplitudes were shown to exist in the dataset. The warming amplitude shows a near exponential distribution. Majorities of the days have warming less than 1K (65%). 35% of days has warming amplitude larger than 1K, 15% of days has warming larger than 2K, and only 3% of days has warming larger than 3K. Majorities of the daily maximum temperatures occurred in the late afternoon, while majorities of the daily minimum temperature occurred in the early morning. Around 40% of days have maximum temperature between 15:00 and 17:00, and about same ratio of the days have minimum temperatures between 5:00 and 7:00. The variance in the local time when the daily maximum and minimum temperatures were reached were due to 1) days where cloud or strong wind present thus there is little or no obvious afternoon warming 2) a few stations where tidal or other effects are more important. Despite the variances, these histograms using all the stations' data combined showed a clear daily warming pattern with characteristics consistent with previous DW study's findings.

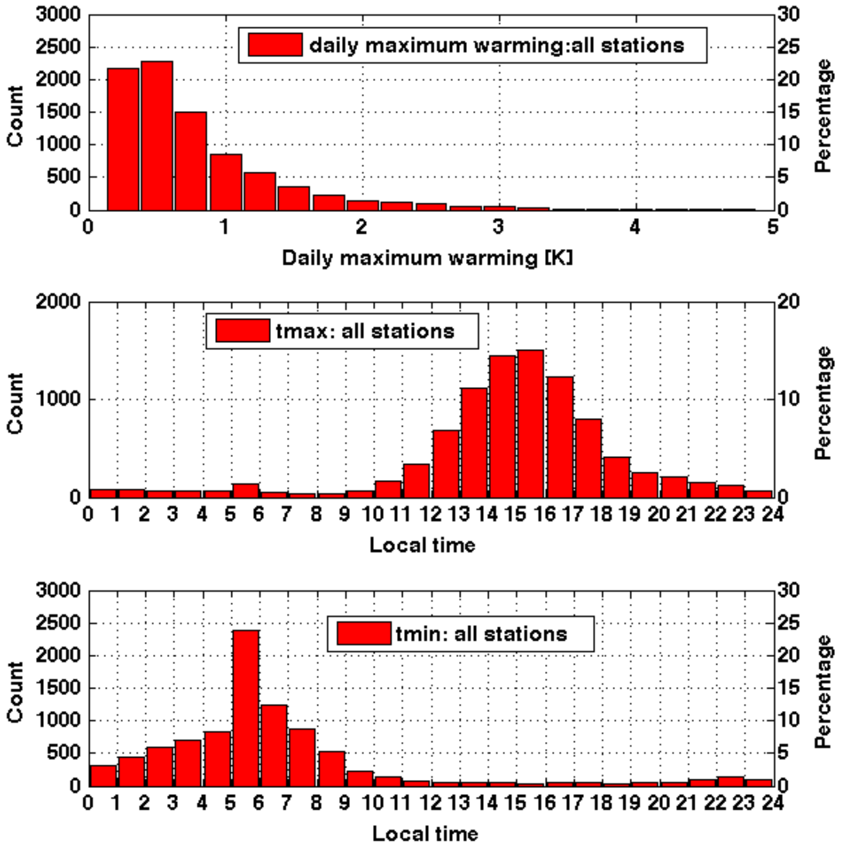

Figure 5.4 Histograms of the daily maximum warming (top panel), time of the day when daily maximum temperatures occur (middle panel) and time of the day when daily minimum temperatures occur (bottom panel) for the five-month time period for all 65 stations.

### 5.3.3 Relationship of diurnal warming amplitude with station location and geographic environment

Compared to the open ocean case, one of the unique characteristics of coastal diurnal warming is its spatial inhomogeneity due to the local geographic features. These features include local currents circulation, tides and wave patterns, bottom roughness and bathymetry, coastline geometry and proximity to features such as river and tidal inlet. The local geographic features affect diurnal warming mostly by mechanical mixing (and sometimes advection), which affects the heat distribution in the vertical (and sometimes horizontal) direction. But unlike the mechanical wind mixing, the mixing induced by geographical features is more predictable as these features do not change in a rapid fashion. For instance, a sheltered lagoon will generally have weaker currents and wave mixing, while locations next to tidal inlet tend to have strong currents and mixing. As a result, recognizing geographic features that affect diurnal warming characteristics is important, so that coast regions with higher possibilities of high daily warming can be recognized readily.

In this section, the influences of the coastal geographic environment, including coastline and bathymetry features, on the daily warming amplitude were examined. The GBR data are suitable for the task as stations are situated along the entire length of GBR with very different environmental surroundings. In the analysis, 65 stations were grouped in six different ways according to the station depths, reef types, latitudes, relative locations to GBR in the longitudinal direction, whether sheltered by islands and proximity to a tidal inlet (Table 5.1). The hypothesis behind categorizing stations by location 'east/west to a nearby island' is that locations to the west of a nearby reef are probably more sheltered from waves and swell propagating from the Pacific Ocean. Also, it is important to point out the method to identify stations close to a tidal inlet is somewhat subjective given that no current measurements were available, only nearby shoreline geometry was examined.

| Criteria to categorize geospatial features | Categories in each method | Definitions and number of stations in each category |
|---|---|---|
| Water depth | None | Use average water depth |
| Reef types | ‘FL’<br>‘SL’<br>‘DSL’ | Reef flat stations located below lowest astronomical tide, 24 stations<br>Reef slope stations with 5~9m depth, 34 stations<br>Deep reef slope stations with ~20m depth, 7 stations |
| Latitudes | ‘North’<br>‘Central’<br>‘South’ | 10 °S to 15 °S, 12 stations<br>15 °S to 21 °S, 43 stations<br>21 °S to 25 °S, 10 stations |
| Relative locations to GBR in the east-west direction | ‘Coast’<br>‘Lagoon’,<br>‘Inner GBR’,<br>‘Outer GBR’,’<br>‘East of GBR’ | Stations right off coast, 11 stations<br>Lagoon sites between coast and GBR chain, 21 stations<br>Stations located on the west edge of the GBR chain, 7 stations<br>Stations located on the east edge of the GBR chain, 24 stations<br>Stations located east from GBR, off continental shelf, 2 stations |
| East/west to a nearby island | ‘Island West’<br>‘Island East’<br>‘N/A’ | Stations being located to the west of the nearest reef, 31 stations<br>Stations being located to the west of the nearest reef, 23 stations<br>Coastal sites, 11 stations |
| Whether is near a tidal inlet | ‘Tidal Inlet’<br>‘No Tidal Inlet’ | Stations possibly near a tidal inlet, 20 stations<br>Stations possibly not near a tidal inlet, 45 stations |

Table 5.1 Different methods to categorize geographic environments for GBR stations.

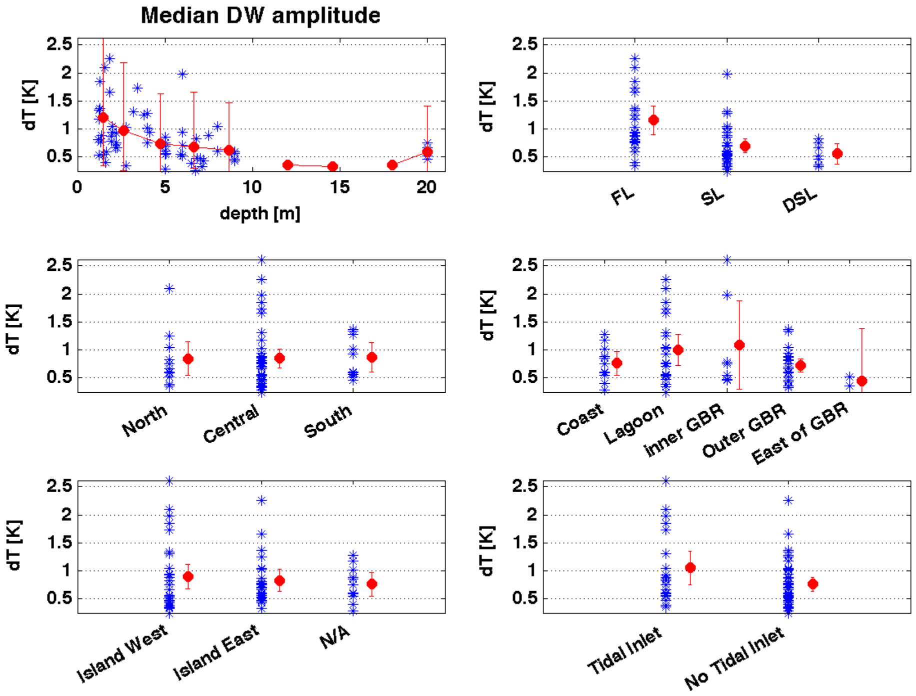

Figure 5.5 The diurnal warming amplitudes for stations grouped in various ways including station depths (upper left plot), reef types (upper right plot), latitudes (middle left plot), relative locations to GBR in the longitudinal direction (middle right plot), whether is sheltered by islands (bottom left plot) and whether is near a tidal inlet (bottom right plot). Averaged diurnal warming amplitude for the five-month period for each station was calculated and then grouped (blue star). For the upper left depth plot, bin-averaged diurnal warming amplitude was given for each 2-meter water depth bin along with the 95% confidence limits (red). For other plots, the mean and 95% confidence limit were given for each group (red).

The mean and 95% confidence limit of diurnal warming amplitude for each group were calculated. The diurnal warming amplitudes were shown to be related strongly to water depths. For stations with water depths of less than 3m, the mean warming amplitude was above 1K. Not surprisingly, the warming amplitudes were also affected by station types, as the water depths and station types were closely related. The diurnal warming at FL stations is significantly larger than the SL and DSL. It was found that the latitudes did not play an important role in determining diurnal warming amplitude, though the north most and south most station has a latitude difference of 15 degree and a north-south distance of about 1600 km. The east-west direction, on the other hand, revealed different warming amplitude patterns. Larger warming amplitude occurred at stations located inside the GBR lagoon and at the inner GBR island chain, possibly as these regions are well sheltered and have weak currents and wave impact, thus more likely to develop stronger warming. Whether the location is to the east or west of a nearby reef does not have much influence on diurnal warming, while stations close to tidal inlet has larger warming than other stations. Note that the warming here refers to the temperature difference between daily temperature maximum and minimums, so the larger warming could actually be due to the tidal influence, like in the Bahamas station CMRC, but this is not strictly the conventional diurnal warming caused by the solar radiation.

To visualize the Great Barrier Reef warming distribution more directly, spatial maps were drawn with station colors representing the diurnal warming amplitude (Figure 5.6). The GBR area spans over 2000km in length, yet multiple measurement locations (usually of different types, i.e., reef flat, reef slope, deep reef slope) often are located on one coral reef within hundreds of meters, making it difficult to distinguish one from another. Thus the diurnal warming spatial map of reef flat, reef slope and deep reef slope stations were plotted separately.

It was shown that for the same region, stations in the reef flat category have generally larger warming amplitude than those in the reef slope category, and much higher than deep reef stations (take a few areas in the south and central parts of GBR for example). Compared within the same category, the stations located at the inner edge of GBR, and inside GBR lagoon have larger warming than the stations located at the outer edge of GBR and east of GBR. These results were consistent with findings shown in Figure 5.5.

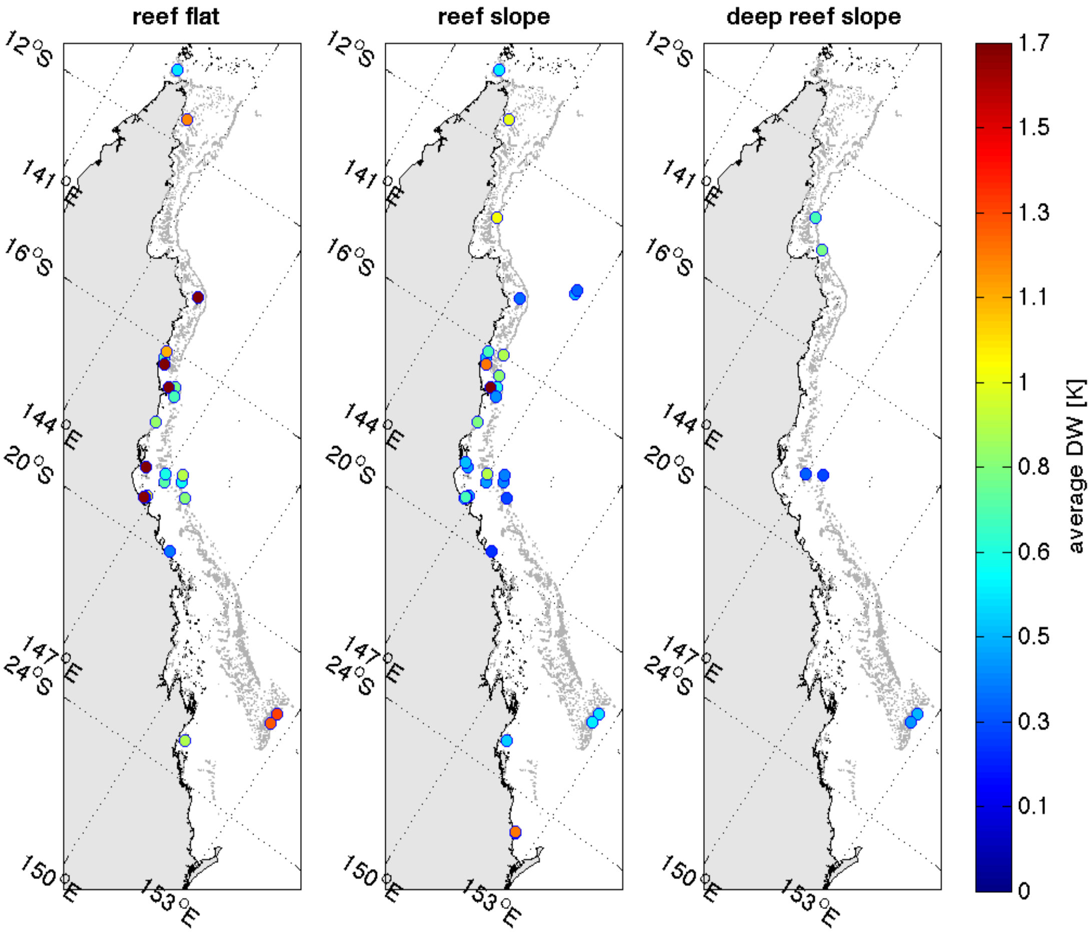

Figure 5.6 Spatial distribution of the diurnal warming amplitude at the studied reef flat (left), reef slope (middle) and deep reef slope stations (right). Note that the darkest red at the upper end of the color bar corresponds to average diurnal warming of 1.7K and higher.

### 5.3.4 Tidal influence on diurnal warming at GBR

When calculating the daily temperature changes at the coast, it is important to differentiate warming due to solar heating versus that due to tides. For stations with strong tidal influence, the tidal effects on daily temperature changes have to be taken into consideration. From modeling point of view, simple empirical models which calculate diurnal warming using only wind and insolation might need additional terms of tidal components; whereas physical diurnal warming models either need to take into consideration of tidal induced water depth changes or solve tidal advection in three-dimensional model. One-dimensional model might not be sufficient to resolve the diurnal warming. For stations with weaker tidal influence compared to solar heating, on the other hand, one-dimensional models previously developed for the open ocean diurnal warming should still be applicable.

As shown in the spectrum analysis for several sample stations, spectral densities calculated from the temperature spectrum analysis provides a useful tool in differentiating forces which influence diurnal warming. Particularly, ($PSD_{M2}/PSD_{24}$) was shown to be a reliable tool for predicting if the time series have single or double temperature daily peaks. Using ($PSD_{M2}/PSD_{24}$) as an indicator of tidal influence versus insolation for each station, its histogram were plotted. We found that despite of the fact that the Great Barrier Reef region has large tidal amplitudes with most of stations have tidal ranges (peak to peak) of 1.5m to 4m, the tidal influences are surprisingly modest compared to solar warming (Figure 5.7). There are 56 stations in GBR dataset data with good enough quality, where spectrum analysis were done properly. Among them, 47 out of 56 stations (84%) have ($PSD_{M2}/PSD_{24}$) values of less than 10%. The stations with ($PSD_{M2}/PSD_{24}$) values larger than 10% are either stations at the outer edge of GBR, east of the GBR island chain (i.e., off continental shelf) or coastal stations close to tidal inlets. The implications of this result is that the tidal influence on the daily warming is generally small compared to the solar heating, even in dynamic coastal regions with large tidal amplitude.

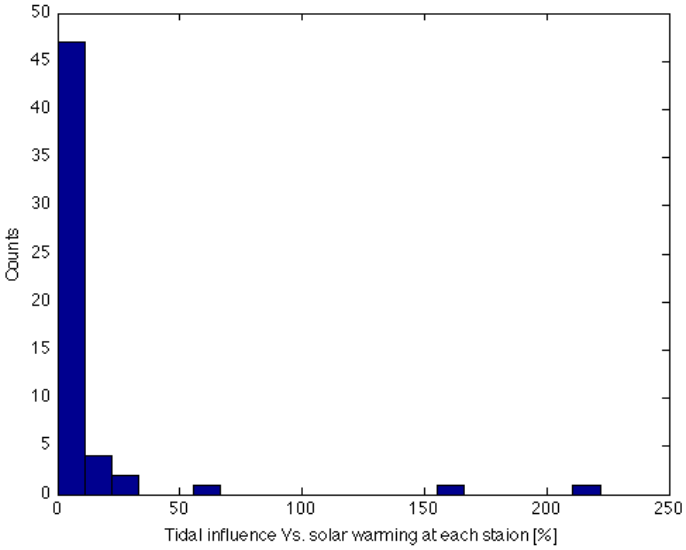

Figure 5.7 Histogram of $PSD_{M2}/PSD_{24}$, the ratio of spectral densities at M2 tidal and 24 hour cycles, from the Great Barrier Reef dataset. There is one $PSD_{M2}/PSD_{24}$ from each station shown as a percentage.

### 5.4 Concluding remarks

In this chapter, the GBR dataset is described and analyzed. The strength of the GBR dataset is in the number of loggers and related locality of the warming. Moreover, the stations are located in macro tidal region, where the tidal ranges are 2-3m, as compared to 0.5m-1m in Caribbean sites. Thus emphasis of the GBR dataset analysis is on the relationship between warming and spatial inhomogeneity, as well as on the evaluation of tidal impacts on warming. By categorizing GBR station locations according to six criteria, it is found that the solar-driven diurnal warming amplitudes are impacted by water depths, station types (reef flat, reef slope, or deep reef slope stations) and the relative locations of the site to the GBR reef chain in the East-West direction. Specifically, the stations located inside the GBR lagoon and inner reef chain are shown to have larger warming on average than coastal sites and outer reef sites. This is suggested to be linked to the hydrodynamic environments, where the lagoon and inner reef sites are more sheltered, thus facilitating stronger heating during calmer conditions. Despite the fact that GBR stations have macro tidal range, 80% of sites have the ($PSD_{M2}/PSD_{24}$) ratio of less than 10%, indicating that the tidal impact on diurnal warming is rather limited compared to solar heating for the majority of the stations.

# Chapter 6 Simulating shallow water diurnal warming using one-dimensional models

Models are very useful tools to understand, diagnose and predict physical phenomena. Various types of 1-dimensional models, from the simplest regression models, to more complex physically-based empirical models, to the most complex turbulence models have been used to study ocean diurnal warming (Chapter 2, section 2.1). Simple regression models are not good choices for our study, given that they are usually limited by the datasets and regions of past studies, which are rarely at the coast. Turbulence closure models need more measurements of estimates of turbulence quantities and are also very computationally expensive, so may not suitable here. Thus, in our coastal study, several one-dimensional physically-based empirical warm layer models are used to simulate coastal diurnal warming. In this chapter, we will first describe individual model algorithms, and then the formulation of several physical processes such as solar absorption schemes will be described. The models will be applied to the Little Cayman station data in the Caribbean Sea in the next chapter.

## 6.1 Models used in our coastal studies

The models we used include the Profiles of Ocean Surface Heating (POSH) model (Gentemann et al 2009), the Zeng and Beljaars (2005) prognostic diurnal warm layer model and a simple well mixed “box model” which assumes heat entering the water column will be quickly well mixed throughout the water column.

### 6.1.1 POSH model

The POSH model (Gentemann et al. 2009) is a modification of the Fairall et al. (1996)

diurnal warm layer model. Both the Fairall et al (1996) and POSH models are derived by simplifying the Price-Weller-Pinkel mixed layer model (Price et al., 1986). Both Fairall et al (1996) and POSH models are based on the hypotheses that changes in temperature and current shear in the upper ocean are only due to surface fluxes (not vertical entrainment) and are confined to a diurnal layer with the depth $D_T$. $D_T$ is determined by requiring the bulk Richardson number Ri to be equal to 0.65.

$$D_T = \sqrt{\frac{2R_i c_p}{\alpha g \rho}} \frac{\tau_{ac}}{\sqrt{Q_{ac}}} \qquad \text{equation 6.1}$$

$Q_{ac}$ is the integrated net heat flux, $\tau_{ac}$ is the integrated wind stress. is the thermal expansion coefficient, g is the gravitational acceleration.

The only major difference is that Fairall et al 1996 assumes a linear vertical temperature profile, while POSH model assumes empirically derived vertical profiles dependent on wind speed while conserving the heat content calculated in Fairall model. The wind dependent warming profile is shown in equation 6.2.

$$\Delta T(z) = e^{-9.5\left(\frac{z}{D_T}\right)^a} \qquad \text{equation 6.2}$$

the value of coefficient a depends on the wind speed range. As shown in Table 6.1.

| wind speed ($ms^{-1}$) | value of a |
|---|---|
| <=1.5 | 2 |
| 3 | 3 |
| 4.5 | 5 |
| 6 | 7 |
| >=7.5 | 9 |

Table 6.1 The values of coefficient a in equation 6.2 for POSH model temperature profiles, which depends on wind speed ranges.

The authors show that the modified vertical profiles in POSH produced larger and earlier surface warming peaks, which produces better comparisons with ship borne radiometer measurements of the skin SST than the Fairall model results.

The models are not conservative in heat because the solar radiation absorbed below the calculated diurnal warm layer $D_T$ is neglected. When the $D_T$ deepens throughout the day, the temperature evolution is not affected by the previously trapped heat below $D_T$.

### 6.1.2 ZB05 (Zeng and Beljaars et al 2005) model

The Zeng and Beljaars (2005) model was derived for the computation of sea surface skin temperature in weather forecasting, data assimilation and ocean-atmosphere coupled modeling. The model calculated both cool skin and warm layer, and the heat is handled in a conservative fashion. The vertical mixing is parameterized using the Monin-Obukhov theory. The authors reasoned that 'the diurnal variation of ocean temperature is usually small at 2–4 m', thus the depth of diurnal warm layer is fixed at 3m. This assumption might be problematic for our coastal applications, where a considerable amount of daily warming is often recorded at deeper depths (Chapter 4 and 5). For the shallow water study where the whole water column is likely to be affected by diurnal warming, this depth needed to be altered as well as parameter $\upsilon$ in equation 6.4.

In ZB05 model, the temperature difference across cool skin layer is calculated as,

$$T_s - T_{-\delta} = \frac{\delta}{\rho_w c_w k_w}(Q + R_s f_s) \qquad \text{equation 6.3}$$

For the warm layer, the temperature difference across the warm layer is calculated as:

$$\frac{\partial}{\partial t}(T_{-\delta} - T_{-d}) = \frac{(Q + R_s - R(-d) * (\upsilon + 1)}{d\rho_w c_w \upsilon} - \frac{(\upsilon + 1)ku_{*w}}{d\phi_t(d/L)}(T_{-\delta} - T_{-d}) \qquad \text{equation 6.4}$$

The symbols and values are given in Table 6.2.

| Symbols and meanings | Equations and values |
|---|---|
| $\delta$: cool skin depth | $\delta = \left[1 + \left(\frac{-16 g \alpha_w {\nu_w}^3}{{u_{*w}}^4 {k_w}^2 \rho_w c_w} (Q + R_s f_s)^{3/4}\right)\right]^{-1/3}$ |
| $\phi_t(\frac{-z}{L})$:stability function(Large et al., 1994) | $1 + 5\frac{-z}{L}$, when –z/L >=0<br>$(1 - 16\frac{-z}{L})^{-1/2}$, when –z/L<0 |
| L: Monin-Obukhov length | $L = \rho_w c_w u^3{}_* /(kF_d)$<br>$F_d = g\alpha_w[Q + R_s - R(-d)]$, when $T_{-\delta} - T_{-d} \le 0$<br>$F_d = \left(\frac{\upsilon g \alpha_w}{5d}\right)^{1/2} \rho_w c_w u^2{}_{*w} \sqrt{T_{-\delta} - T_{-d}}$, when $T_{-\delta} - T_{-d} > 0$ |
| model input related: | |
| Q: surface fluxes | Q=LH+SH+LW |
| $R_s$: incoming surface solar radiation | |
| R(-d): the solar radiation left at depth -d | |
| $f_s$: fraction of solar radiation absorbed in the cool layer | Calculated using nine band scheme – as in POSH. |
| $u_{*w}$: water friction velocity | $u^2{}_{*w} = u^2{}_{*a}\sqrt{\rho_a/\rho_w}$ |
| Constants: | |
| g :gravitational acceleration | g =9.8 $ms^{-2}$ |
| $\alpha_w$:water thermal expansion | $\alpha_w$=1.e-5 *T (T>1 in Celsius); 1.e-5 (T<1) |
| $c_w$: water specific heat capacity | $c_w$=4190 J/(kg.K) |
| $\rho_w$: water density | $\rho_w$=1025 $kg.m^{-3}$ |
| $k$: Von Karman constant | $k$=0.4 |
| $k_w$:molecular thermal conductivity | $k_w$=1.4$e^{-7}Wm^{-1}K^{-1}$ |
| $\nu_w$:kinematic viscosity of water | $\nu_w$=1.$e^{-6}$ $m^2s^{-1}$ |
| Constants that might need to be changed: | |
| d: a fixed warm layer depth where the diurnal warming is negligible. | d=3 |
| $\upsilon$: empirical coefficients which values depends of the choice of d | $\upsilon$=0.3 |

Table 6.2 Symbols and values used in the ZB05 model

The choice of parameter $\upsilon$ is determined by the choice of the diurnal warming depth d (similar to $D_T$ in the POSH model). In the Zeng and Beljaars (2005) paper, the d value is 3m, and the $\upsilon$ value is then chosen as 0.3, so that for the peak insolation of 1000 W and assuming the balance of the last two terms in equation 6.2, (Ts - Td) is about 3 K under weak wind conditions. Note that, if a significantly different d is used, $\upsilon$ needs to be adjusted under the above constraint.

### 6.1.3 A simple "box model"

Another model we considered for the shallow water diurnal warming is very simple. For the "box model", we calculated the heat absorbed into the water column, and assume it is instantaneously evenly distributed so there is no vertical thermal stratification at any time. Though conceptually very simple, the modeled temperature profile might be quite realistic when the wind speed is strong, or where the water depths are very shallow so that the surface and bottom boundary generate enough turbulence to mix the water column. The temperature changes at each step can be calculated as

$$\rho_w c_w h \frac{\partial T}{\partial t} = Q + Rs * frac \qquad \text{equation 6.5}$$

where $frac$ is fraction of solar radiation absorbed in the water, h is the depth of the water column, other symbols are the same as in Table 6.2.We found better agreement between box model and data, when $frac$ is set to be 1, i.e., assuming all solar radiation is being absorbed into the water column. This might be related to multiple reflection of solar radiation due to the presence of the shallow bottom. Even though the heat from solar radiation may not be absorbed entirely in the downward path, part of light is reflected at the bottom, and then reabsorbed into the water column or reflected again at the sea surface, or absorbed at the sea bed and the heat released into the water above creating a convectively sustained bottom boundary layer.

## 6.2 Formulation of several physical processes

### 6.2.1 Two solar absorption schemes

To properly model diurnal warming phenomenon, one important aspect to consider is how the solar radiative fluxes are absorbed and the resultant heat is redistributed in the vertical direction. The extinction of light through a medium is described by Beer-Lambert's law. For absorption of solar radiation in the ocean water, a simple multiple band empirical scheme (Gentemann et al., 2009; Paulson and Simpson, 1981) and a more complex empirical scheme considering the role of chlorophyll, cloud amounts and solar zenith angle were both considered (Ohlmann and Siegel, 2000) are frequently used and described below.

#### 6.2.1.1 An improved nine-band scheme considering solar zenith angle

A nine band spectral parameterization was originally used by Paulson and Simpson (1981), the scheme has a stronger absorption at all depths, but particularly at shallow depths compared to a previous three-band parameterization. Gentemann et al (2009) improved the scheme by taking into account subsurface solar angle. The ratio of the solar radiation absorbed between surface and depth z is

$$f_w(z,\theta) = 1 - \sum_{i=1}^{9} F_i \exp(-\frac{z}{\zeta_i * \cos(\theta)}) \qquad \text{equation 6.6}$$

where $\theta$ is subsurface solar angle.

Gentemann et al (2009) found that multiplying the ratio by 1.2 produced more realistic diurnal warming profile compared to profiler measurements, reasoning that the sea water absorption is larger than that in the clear water, on which the original nine band model is based. Not including water properties such as chlorophyll concentration which increase solar absorption, might explain the discrepancy. This discrepancy might be larger for the coastal regions where chlorophyll and other dissolved or suspended material concentrations are higher. The model nevertheless is a good way for simple calculations, in situations where the concentrations of absorbing or scattering material is not known.

| Wavelength [$\mu$] | i | $F_i$ | $\zeta_i$[m] |
|---|---|---|---|
| 0.2-0.6 | 1 | 0.237 | 3.48*10 |
| 0.6-0.9 | 2 | 0.360 | 2.27 |
| 0.9-1.2 | 3 | 0.179 | $3.15*10^{-2}$ |
| 1.2-1.5 | 4 | 0.087 | $5.48*10^{-3}$ |
| 1.5-1.8 | 5 | 0.080 | $8.32*10^{-4}$ |
| 1.8-2.1 | 6 | 0.0246 | $1.26*10^{-4}$ |
| 2.1-2.4 | 7 | 0.025 | $3.13*10^{-4}$ |
| 2.4-2.7 | 8 | 0.007 | $7.82*10^{-5}$ |
| 2.7-3.0 | 9 | 0.0004 | $1.44*10^{-5}$ |

Table 6.3 Values of $F_i$ and $\zeta_i$ values in nine-band absorption model, as in Table 1 in Paulson and Simpson (1981)

#### 6.2.1.2 A more complex empirical scheme considering the role of chlorophyll, cloud amounts and solar zenith angle

Ohlmann and Siegel (2000) derived a more complex scheme using empirical solar transmission parameterizations derived from radiative transfer model HYDROLIGHT (http://www.sequoiasci.com/product/hydrolight/). Similar to the nine band model, the ratio of solar radiation at the surface and absorbed at and above depth z is also a sum of exponentials

$$f_{OS}(z,chl,CI,\theta) = 1 - \sum_{i=1}^{n} A_i \exp(-K_i z) \qquad \text{equation 6.7}$$

where coefficient $A_i$ and $K_i$ are calculated as linear functions of chlorophyll concentration, cloud index and solar zenith angle.

$$y = C_1 chl + C_2 CI + C_3 \cos^{-1}\theta + C_4 \qquad \text{equation 6.8}$$

where *chl* is the chlorophyll concentration, CI is the cloud index (the fraction of cloud covering the sky, ranging from 0 to 1) and $\theta$ is the solar zenith angle; *y* refers to either *A* or *K* coefficients and is determined using the values of $C_1$, $C_2$, $C_3$ and $C_4$ in Table 6.4. Different sets of coefficients were used for cloudy and clear sky cases. For cloudy sky cases, the coefficients $A_i$ and $K_i$ are determined by *chl* and CI; and for clear sky cases, the coefficients are determined by *chl* and $\theta$ (Table 6.4).

| | $C_1$ | $C_2$ | $C_3$ | $C_4$ |
|---|---|---|---|---|
| (a) Cloudy Sky | | | | |
| $A_1$ | 0.026 | 0.112 | 0 | 0.366 |
| $A_2$ | -0.009 | 0.034 | 0 | 0.207 |
| $A_3$ | -0.015 | -0.006 | 0 | 0.188 |
| $A_4$ | -0.003 | -0.131 | 0 | 0.169 |
| $K_1$ | 0.063 | -0.015 | 0 | 0.082 |
| $K_2$ | 0.278 | -0.562 | 0 | 1.02 |
| $K_3$ | 3.91 | -12.91 | 0 | 16.62 |
| $K_4$ | 16.64 | -478.28 | 0 | 736.56 |
| (b) Clear Sky | | | | |
| $A_1$ | 0.033 | 0 | -0.025 | 0.419 |
| $A_2$ | -0.010 | 0 | -0.007 | 0.231 |
| $A_3$ | -0.019 | 0 | -0.003 | 0.195 |
| $A_4$ | -0.006 | 0 | -0.004 | 0.154 |
| $K_1$ | 0.066 | 0 | 0.006 | 0.066 |
| $K_2$ | 0.396 | 0 | -0.027 | 0.886 |
| $K_3$ | 7.68 | 0 | -2.49 | 17.81 |
| $K_4$ | 51.27 | 0 | 13.14 | 665.19 |

Table 6.4 Linear regression coefficients to calculate A and K parameters using equation 6.8. (a) gives coefficients for the cloudy sky model, which depends on chlorophyll concentration and cloud amount (b) gives coefficients for the clear sky model, which depends on chlorophyll concentration and solar zenith angle. This table is the same as Table 2 in Ohlmann and Siegel (2000).

### 6.2.1.3 Comparison of the absorption profiles

In this section, the absorption profiles of both schemes were explored.

As shown in Gentemann et al 2009, the nine-band model absorbs strongly in the shallow depths. Over 50% of solar radiation is absorbed in the top meter (Figure 6.1a). The ratio of the absorbed radiation also depends on solar zenith angle $\theta$. At zero $\theta$, the absorption rate is the smallest because the optical path to a given depth is the shortest. The absorption ratio increases as the zenith angle increases. For $75^{\circ}$ $\theta$, 90% of solar insolation is absorbed by 10m depth compared to 80% at zero $\theta$.

The absorption profile for the Ohlmann and Siegel (2000) case for clear sky and when chlorophyll concentration was set to 0.1 mg.m$^{-3}$ is shown (Figure 6.1b). The curve is also a function of solar zenith angle $\theta$, and we compared it with the nine-band model case. We can see the curves are very similar to the nine band model, though the absorption ratio in Ohlmann and Siegel scheme increases less with the increasing solar zenith angles.

The next plot (Fig 6.1c) illustrates the influence of chlorophyll concentration on the absorption in the Ohlmann and Siegel (2000) scheme. The clear sky case was plotted with solar zenith angle set to zero, but with varying chlorophyll concentrations *chl*. The solar absorption rates for *chl* = 0.01 and 0.1 mg.m$^{-3}$are very similar, and quite closely resemble the nine band model case with zero zenith angle (black line). These levels of *chl* are typical of the open ocean values (e.g. http://eoimages.gsfc.nasa.gov/images/imagerecords/4000/4097/S19972442003273.jpg). For *chl* equal to 1mg.m$^{-3}$, which is often found in coastal regions and northern high latitudes, the absorption ratio becomes larger than the nine-band model for all depths except the very shallow (<0.3m). For *chl* ranges equal or larger than 10 mg.m$^{-3}$, which are often found in the coastal zone with upwelling or arctic regions, the absorption becomes very large. Nearly 100% of the solar radiation is absorbed in the top 6 meters.

The last plot shows the relationship of the cloud amount CI on the absorption profile in Ohlmann and Siegel case. CI can affect the absorption rate as clouds alter the spectral distribution of radiant energy. The nine-band scheme absorption rate at zero zenith angles is similar to those in the cloudy case during low cloud coverage when 0<CI<0.4, however it is much larger than the cloudy case during medium to high cloudy conditions.

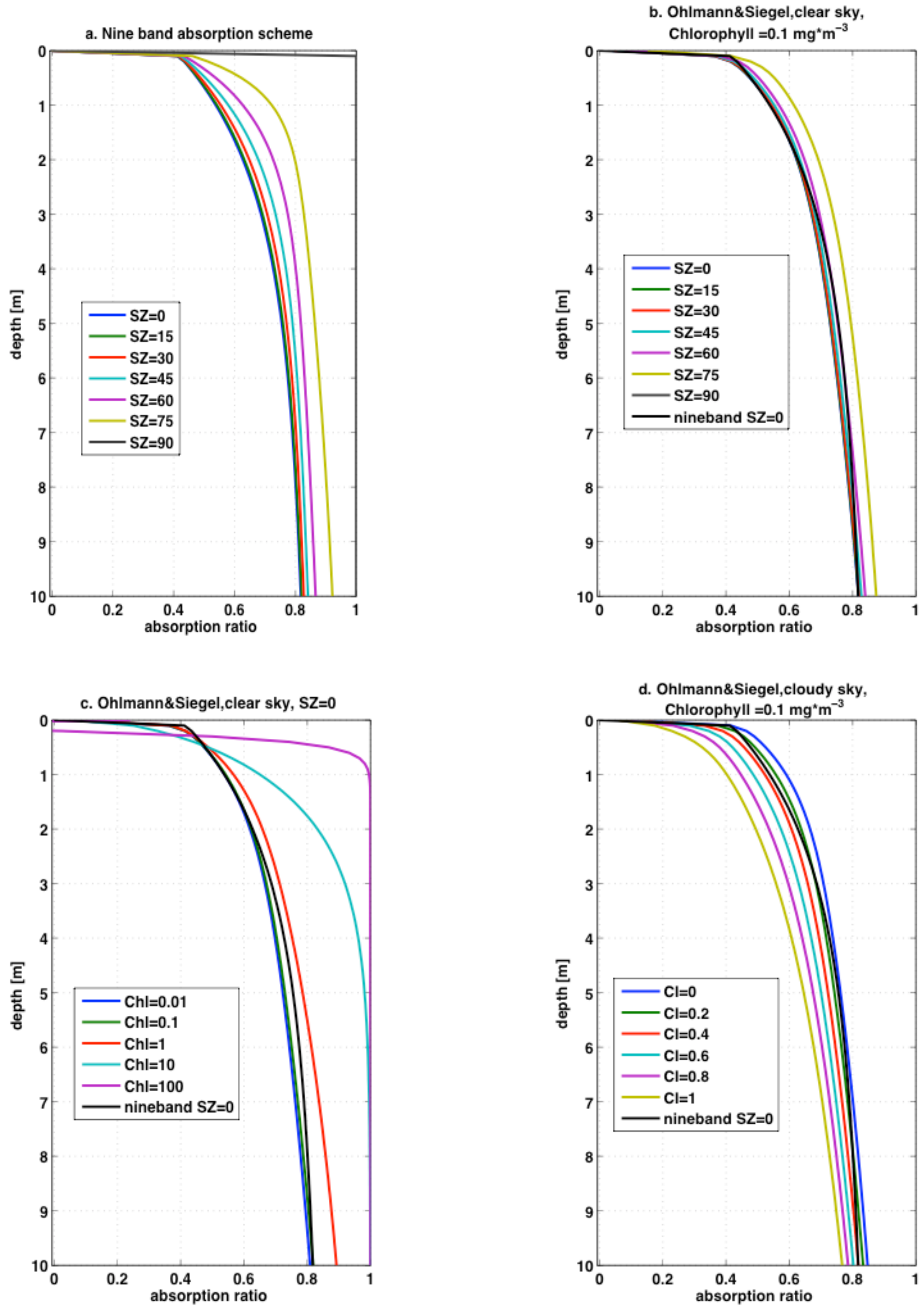

Figure 6.1 Comparison of the vertical solar absorption profiles using nine-band and Ohlmann and Siegel schemes. Panel a shows profiles from the nine-band scheme was shown with different solar zenith angles. Panel b, c, d shows the profiles from Ohlmann and Siegel scheme with varying solar zenith angle, chlorophyll concentration and cloud index respectively. Nine-band scheme with zero zenith angle are also plotted for comparison.

To summarize, the absorption profiles of the nine-band schemes are similar to the Ohlmann and Siegel cases during clear sky or low cloud cases (cloud fraction less than 0.4), and when chlorophyll concentration is similar to those found in open ocean (0.01-0.1 mg·m$^{-3}$) cases. For our diurnal warming modeling in the coastal ocean, we can use the nine-band model for the most cases, except those where chlorophyll > 1 mg·m$^{-3}$, where the latter should be used. The chlorophyll concentration at the Little Cayman station is mostly < 1 mg·m$^{-3}$ (http://earthobservatory.nasa.gov/GlobalMaps/view.php?d1=MY1DMM_CHLORA).

### 6.2.2 Bottom absorption and reflection

The presence of the sea floor affects the distribution of radiative heat fluxes, as the substrate will absorb part of the remaining solar radiation, while reflecting the rest. In this section, we discuss the fractions of incoming solar radiative fluxes being absorbed into the bottom, being absorbed into the water columns, and escaped back into the air, as a function of water depth, number of light rays (or numbers of reflections plus one), and the bottom albedo. We use the nine-band absorption model described in section 6.2.1. First we set the bottom albedo to be 0.3, which is a reasonable albedo for the coral and set the solar incidence angle to be zero as this represents the case where the influence of the corals on the radiation is greatest. We assume that the solar rays are partially reflected at the bottom and then partial internal reflection at the surface. The water-air reflection coefficient is set to be 1, i.e., no energy escaped back into the air to represent the worst case. The coefficient is an estimate, since the amount of energy after the second light path is quite small, the value is not very important. Moreover, according to Snell's law, when the incident angle from the water to air is larger than 48.6˚, there is total reflection.

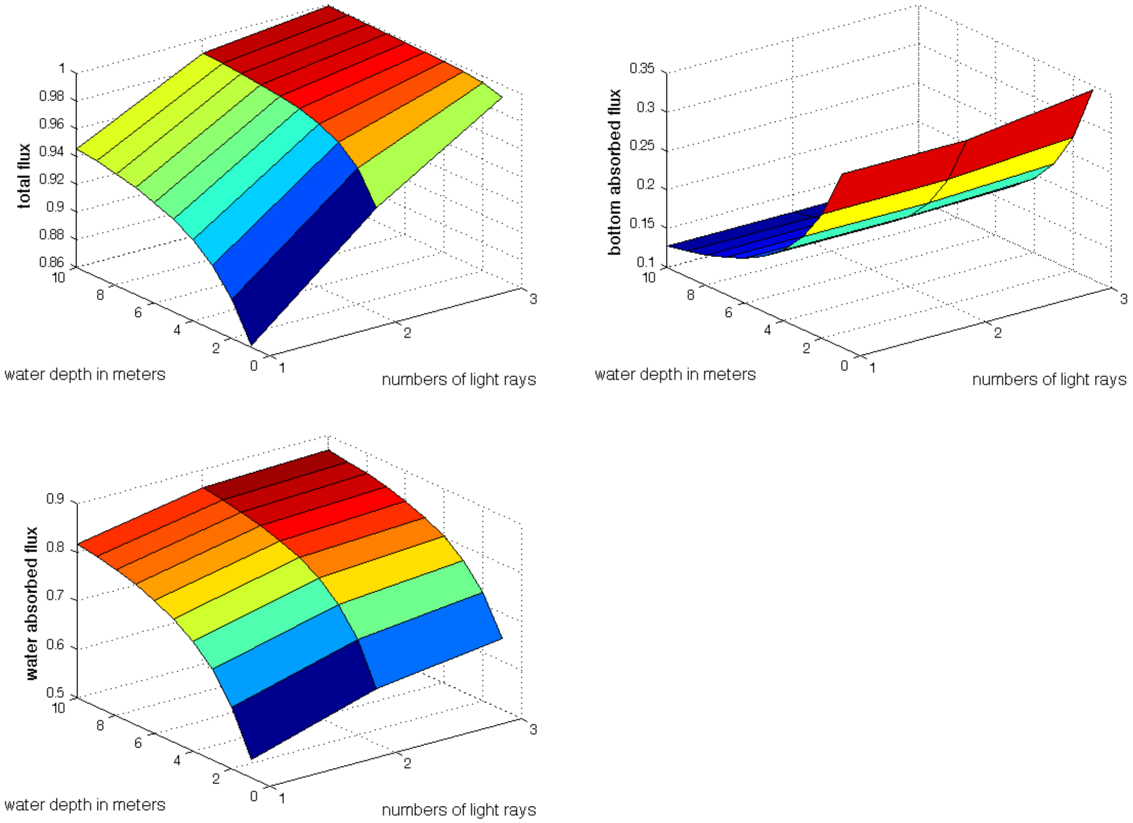

Figure 6.2 The fraction of total solar fluxes (upper left), bottom absorbed fluxes (upper right), solar fluxes absorbed by water (lower right) as a function of water depth and number of light rays in the water. The bottom albedo is set to be 0.3. The fluxes are shown as fractions of incoming solar radiative flux.

Giving that a large portion of the bottom reflected light will have a large incidence angle, thus it is reasonable to set the coefficient to 1. How the solar energy is distributed as a function of water depth and number of the light rays is shown in Figure 6.2. For total radiative fluxes (upper left), we can see that almost all (>95%) of the solar fluxes is absorbed either by water or bottom after two reflections, even when the water depth is 1m. Hence, there is no need to consider more than one bottom reflection and one surface reflection regardless of the water depth. For the deeper water, the total fluxes increase only slightly with each reflection. But for very shallow depths (e.g. < 2m), multiple reflections are important mechanisms to consider. For instance, the downward absorption for the 2m depth water column absorbed about 88% of incoming solar radiation, while about 94% is absorbed after the first bottom reflection.

Considering bottom absorption (Figure 6.2, upper right), more energy is absorbed at the bottom for shallower depths. About 12% of the total flux is absorbed by the bottom for 10-m water depth, and up to 35% is absorbed for the 1-m depth water column. The water absorbed fluxes is also strongly influenced by water depth, only 65% of the flux is absorbed by the water for 1-m depth, compared to over 85% at 10m depth after two reflections.

For majority of the Caribbean station where the averaged water depth is 6.5m, we consider only one bottom reflection. We calculate the fluxes as a function of varying bottom albedos raging from 0.1 to 0.7. For Caribbean stations, the sea bottom are categorized as “colonized pavement” which is flat, low-relief, solid carbonate rock with coverage of algae and coral. So this is probably quite similar to coral sand, which has a bottom albedo ≥0.5 (Burns et al 2010).

As shown in Figure 6.3, one bottom reflection is sufficient to attenuate over 96% of the incoming solar radiation. For a bottom albedo of 0.5, the bottom absorbed flux accounts for < 10% of the incoming flux, while the water absorbed about 86% of the incoming flux.

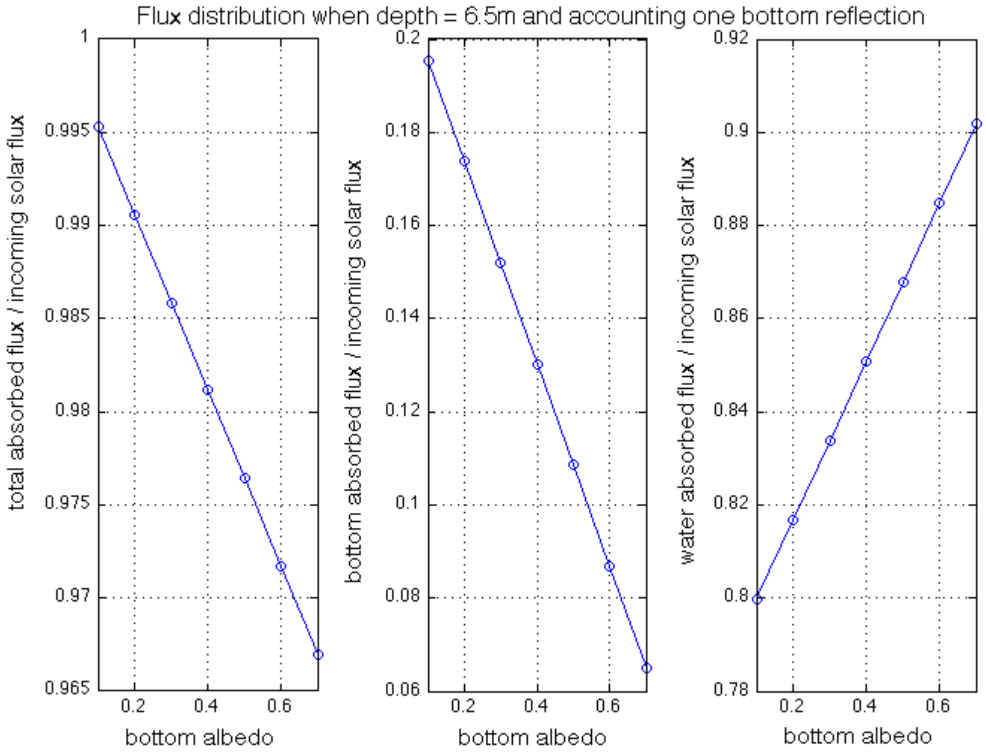

Figure 6.3 The fraction of total flux, bottom absorbed flux and water absorbed flux as a function of bottom albedo, when the depth is 6.5m and one bottom reflection.

## 6.3 Concluding remarks

Three 1-dimensional physical-empirical diurnal warming models are described in this chapter, including a simple well mixed box model, POSH model, which calculates a diurnal warm layer depth $D_T$ each step and assumes a wind dependent temperature profile, as well as ZB model, which parameterizes vertical mixing based on Monin-Obukhov theory and assumes the diurnal warm layer to be fixed at 3m. The chapter gives detailed formulations of these models. Next, two solar absorption schemes are described and their values and dependence on various environmental parameters are compared. It is found that the absorption profiles of the nine-band schemes are similar to the Ohlmann and Siegel scheme during clear sky or low cloud cases (cloud fraction less than 0.4), and the cases when chlorophyll concentration is similar to those found in open ocean and some of the coastal regions (0.01-1 mg·m$^{-3}$). Finally, the chapter quantifies how the heat fluxes are distributed between water absorption and bottom absorption, given different bottom albedo values, numbers of bottom/surface reflections and water depths. For a depth of 6.5m, which is a typical water depth for most of the Caribbean stations, one bottom reflection is sufficient to attenuate over 96% of the incoming solar radiation. For a bottom albedo of 0.5, the bottom absorbed flux accounts for less than 10% of the incoming flux, while the water absorbed about 86% of the incoming flux.

# Chapter 7 Diurnal warming simulations for the Little Cayman station

In this chapter, we report on model simulations of warming using the three models described in the previous chapters, with the forcing input from Little Cayman station (LCIY). The modeled temperatures are compared with the in-situ measurements. We chose the Little Cayman station as the location to conduct our modeling study because of the simpler environment and more comprehensive measurements. The station has co-located measurements of light and weather, a five-point vertical thermal profile measurement in 2011. Also, the station is located in a calmer, well sheltered environment. Thus it is suitable for the detailed study of 1-d model performance and necessary model adjustment for the shallow water case.

The model runs are simulated for each day from day 35 (February 4) to day 269 (September 26) in 2011. We use the nine band model for the solar absorption scheme (Gentemann et al., 2009; Paulson and Simpson, 1981). The model runs reset the warming to be zero every day at 6am.

## 7.1 Acquiring downward longwave radiation data

Besides solar radiation, surface fluxes which include latent heat fluxes, sensible heat fluxes, and longwave radiative fluxes data are needed to calculate heat budget. At LCIY, the in-situ measurements include most of variables needed to calculate surface fluxes, except for downward longwave radiation (DLWR). Thus we extract the value for Little Cayman location from hourly global NCEP Climate Forecast System Reanalysis (CFSR) data for 2011. As shown, DLWR values ranges from 360 to 440 $Wm^{-2}$ throughout the year (Figure 7.1). The variations are caused by those in near-surface air temperatures, water vapor and clouds (Duarte et al., 2006). DLWR are categorized as surface fluxes as all of it is absorbed in the first 0.1mm of the ocean.

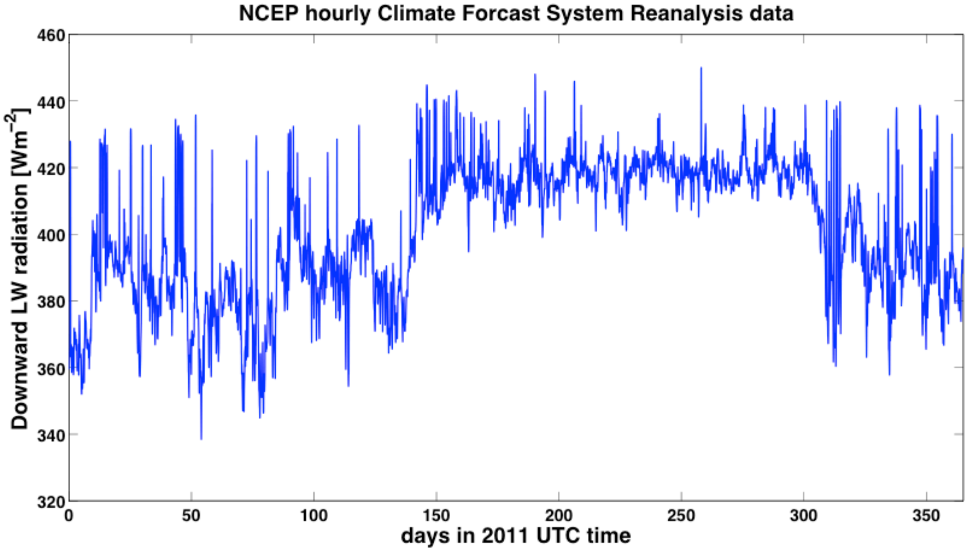

Figure 7.1 Downward longwave radiation data for 2011 at LCIY location extracted from NCEP Climate Forecast System Reanalysis (CFSR) data.

## 7.2 Model data comparison results: time series case studies

In this section, time series of modeled results from the ZB model (Zeng and Beljaars 2005) , box model, and the POSH (Gentemann et al 2009) model are compared to the logger measurements, along with the environmental variables including wind, solar insolation, rain and calculated fluxes (Figure 7.2).

The time series from day 44 to day 54 are shown first. The daily wind maximum exceeded 10 ms$^{-1}$ for 8 out of 10 days. Due to the strong wind, the latent heat flux is large which causes the total heat fluxes to be ~500Wm$^{-2}$ for most of the days. For heat fluxes input of such amplitudes, the ZB and POSH models produced very little warming (<0.1K); while the measurement data actually shows the water warms up evenly throughout the column, ranging from 0.2 to 0.5K daily. The box model, on the other hand, was capable of simulating the warming with similar amplitudes as found in the data, although we noticed the model predicted too much cooling by the end of the day during strong wind cases.

The time series from day 76 to day 86 are discussed next. The first five of the ten-day period has very large wind speed of over 10 $ms^{-1}$, so again the ZB and POSH models produced very weak warming (<0.1K). The box model produces diurnal warming amplitude closer to the measurements, and loses too much heat at night. The maximum wind speeds for the next five days are around 6-9 $ms^{-1}$.The calculated total heat fluxes ranged from 800 to 1000$Wm^{-2}$. For this range of wind speeds, the ZB model produces sharp heating peak at amplitudes comparable to those measured by the shallowest logger. However, the warming peak occurs 2-3 hours earlier and is very narrowly located temporarily compared to the measurements. For the box model, the timing and amplitude of the warming are close to that in the data. However, box model produced a gradual and insufficient cooling during this period. The POSH model produced smaller warming than the measurements, especially for the near bottom depths, though the timing of the peak warming is similar. A sharp temperature increase on day 82 is shown in the data; this is possibly due to the very brief rainfall during this time. It is possible that a fresh water lens from the rain could form on ocean surface. And since after the rainfall the solar radiation remains very strong, then a stable thin layer can be rapidly heated up thus surface warming suddenly increased. This phenomenon has been reported by previous research (Webster et al., 1996). Notice the measurement data only show this abrupt increase of the temperature at the near surface depths, because the rain amount is small and the rain event is brief. The simulation of rain is not set up in our models at this stage, so this event is not reflected in the model results.

Examining the time series from day 130 to 140, the first four and last three days of the ten-day period have intermediate wind speed of between 5 to 9 ms$^{-1}$, so the model behaviors are similar to the period between day 82 to 85. Focusing on day 134 to day 136, where the maximum winds are below 5 ms$^{-1}$, logger-measured temperatures show clear thermal stratification. Both the ZB and POSH models produced larger surface warming than that from the shallowest logger (note the different y-axis scales in Figure 7.2). This is understandable since the surface SST (which is produced by the ZB and POSH models) could be much larger than subsurface temperatures at 1m or deeper (which are measured by the shallowest logger) under low wind speeds, however, the ZB model seems to be produce extraordinarily large warming peaks, 1.5 to 2 times those of the POSH model. The temperatures produced by the POSH model are smaller compared to logger data for individual sub-surface depths. The temperature simulated by the box model is smaller than measured by the top loggers, but often larger than measured by the mid-depth and bottom loggers. The inability of the box model to reproduce thermal signals is expected as the water is far from well mixed.

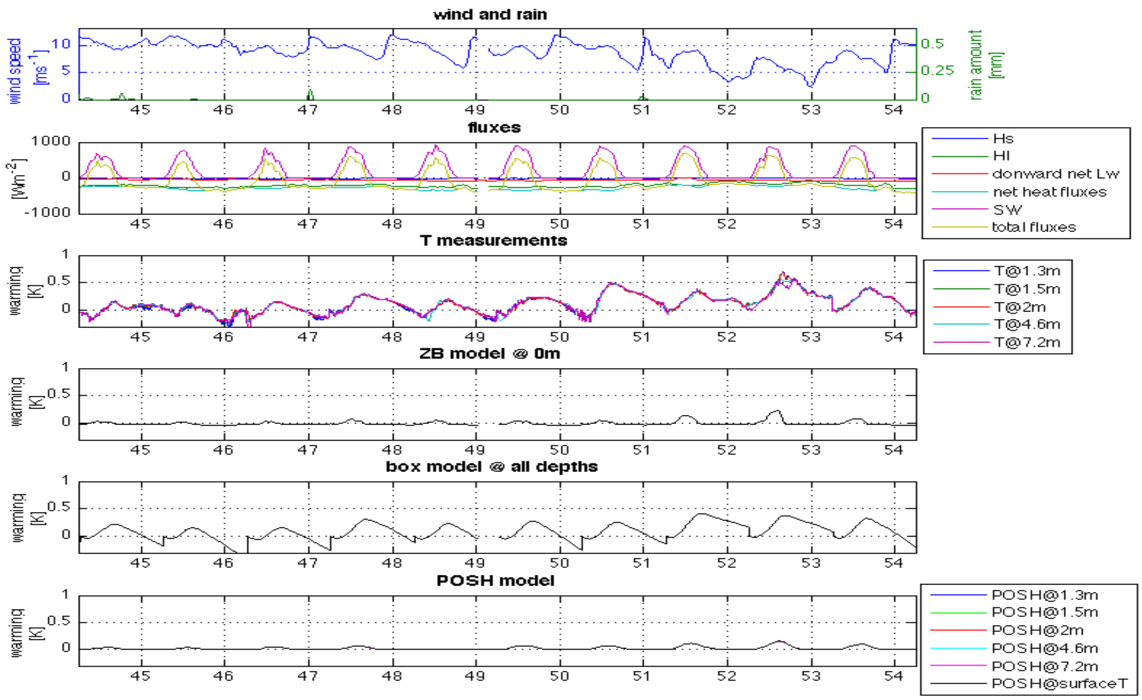
wind and rain
wind speed [ms-1]
rain amount [mm]
0
5
10
0
0.25
0.5
45
46
47
48
49
50
51
52
53
54
fluxes
[Wm-2]
1000
0
-1000
Hs
Hl
donward net Lw
net heat fluxes
SW
total fluxes
T measurements
warming [K]
1
0.5
0
T@1.3m
T@1.5m
T@2m
T@4.6m
T@7.2m
ZB model @ 0m
box model @ all depths
POSH model
POSH@1.3m
POSH@1.5m
POSH@2m
POSH@4.6m
POSH@7.2m
POSH@surfaceT

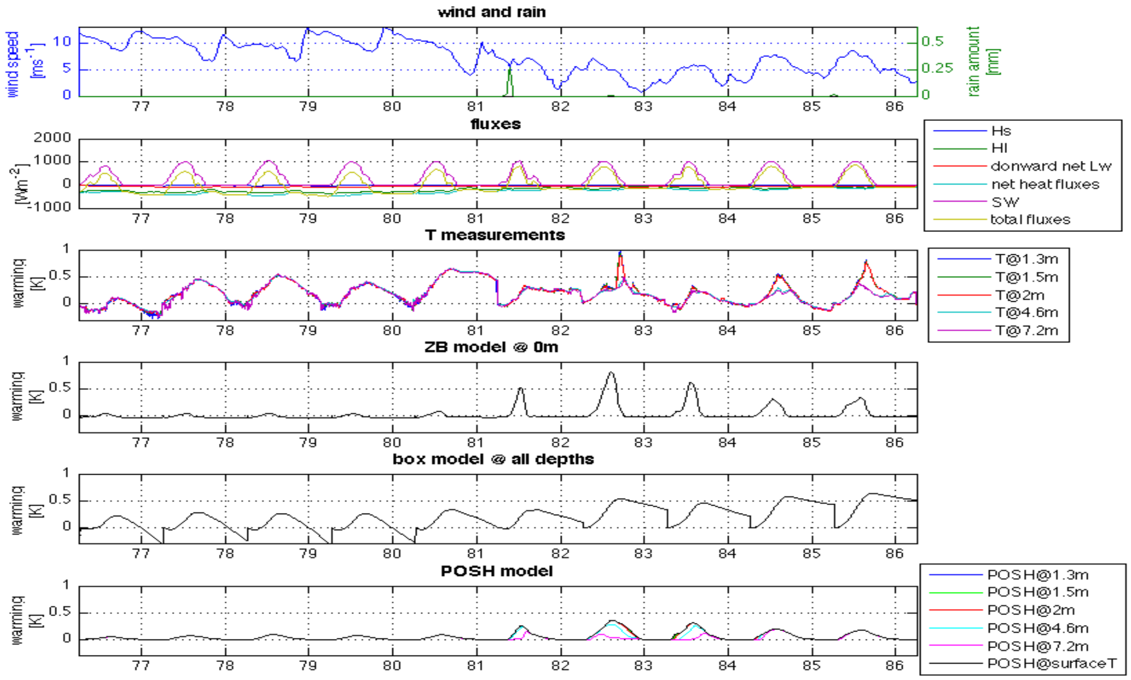
wind and rain
wind speed [ms-1]
rain amount [mm]
0
5
10
0
0.25
0.5
77
78
79
80
81
82
83
84
85
86
fluxes
[Wm-2]
2000
1000
0
-1000
Hs
Hl
donward net Lw
net heat fluxes
SW
total fluxes
T measurements
warming [K]
1
0.5
0
T@1.3m
T@1.5m
T@2m
T@4.6m
T@7.2m
ZB model @ 0m
box model @ all depths
POSH model
POSH@1.3m
POSH@1.5m
POSH@2m
POSH@4.6m
POSH@7.2m
POSH@surfaceT

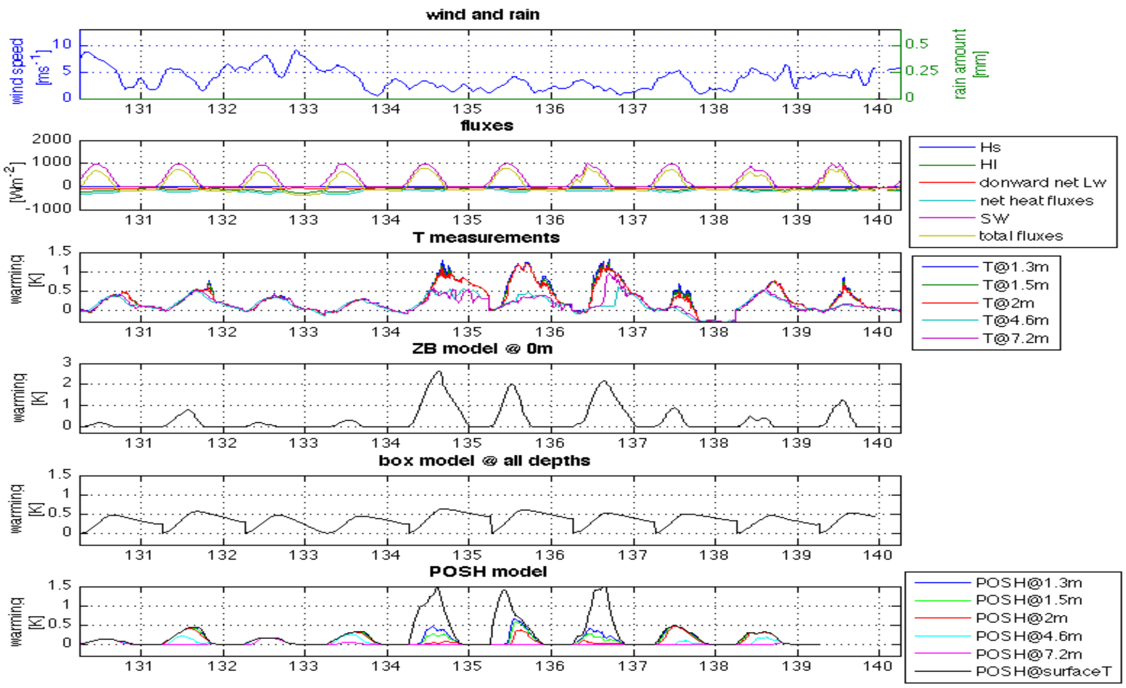

Figure 7.2 Time series of modeled and measured temperature time series for three sample periods. X-axis is the year day in 2011. For each sample period, the top panel is wind speed in ms$^{-1}$ and rain amount in mm. The second panel shows sensible heat flux Hs, latent heat flux Hl, downward net longwave flux, net surface heat fluxes (=Hs+Hl+net longwave), shortwave radiation SW, and total heat fluxes, all in unit of Wm$^{-2}$. The third panel shows the temperature measurements at 1.3m, 1.5m, 2m, 4.6m and 7.2m. The fourth panel shows the surface temperatures simulated by the Zeng and Beljaars 2005 model. The fifth panel shows the temperatures simulated by the simple box model. The bottom panel shows the temperature measurements at 1.3m, 1.5m, 2m, 4.6m and 7.2m as well as the surface temperature simulated by the POSH model.

The following table summarizes the results from comparing the model simulated temperature time series with the data.

| | Box model | ZB model | POSH |
|---|---|---|---|
| High winds days ($U_{max} \geq 9 ms^{-1}$) | Modeled DW amplitudes compare well with data, cooling is too fast | Model produces almost no warming, very different from the data. | Model produces well-mixed profile, and produced almost no warming, very different from the data. |
| Intermediate wind days ($5\ ms^{-1} < U_{max} < 9 ms^{-1}$) | Modeled DW amplitudes compare well with data, cooling is too slow. Residual heat remains by 6am on the next day. | Modeled amplitudes are very sensitive to winds. The modeled results are closest to the data in this range. However the peaks occur earlier and are much narrower. | Model produces stratified vertical profiles. Overall the amplitudes are similar to or smaller than the measurements. |
| Low wind days ($U_{max} \leq 5 ms^{-1}$) | Modeled amplitudes are much smaller than the shallow loggers and of similar amplitude or larger than deeper loggers. Cooling is slower than in the measurements | Modeled peaks are much larger than the top logger data peak, and occur earlier. | Model produces stratified vertical profiles. The modeled surface warming is larger than the shallow logger measurements, but smaller that ZB results. For the measurements depths, modeled amplitudes are smaller than in the measurements. |

Table 7.1 Result summaries from model-data time series comparisons.

### 7.3 Model data comparison results: histograms of the warming amplitude, timing and shapes

In this section, we summarize the diurnal warming characteristics for the model results and measurement data for the entire time periods where data are available, i.e., from day 35 (February 4th) to day 269 (September 26) in 2011. We use histograms to illustrate the distribution of warming amplitudes, timing, as well as the lengths and shapes of the warming and cooling phases.

### 7.3.1 Distributions of the diurnal warming amplitudes

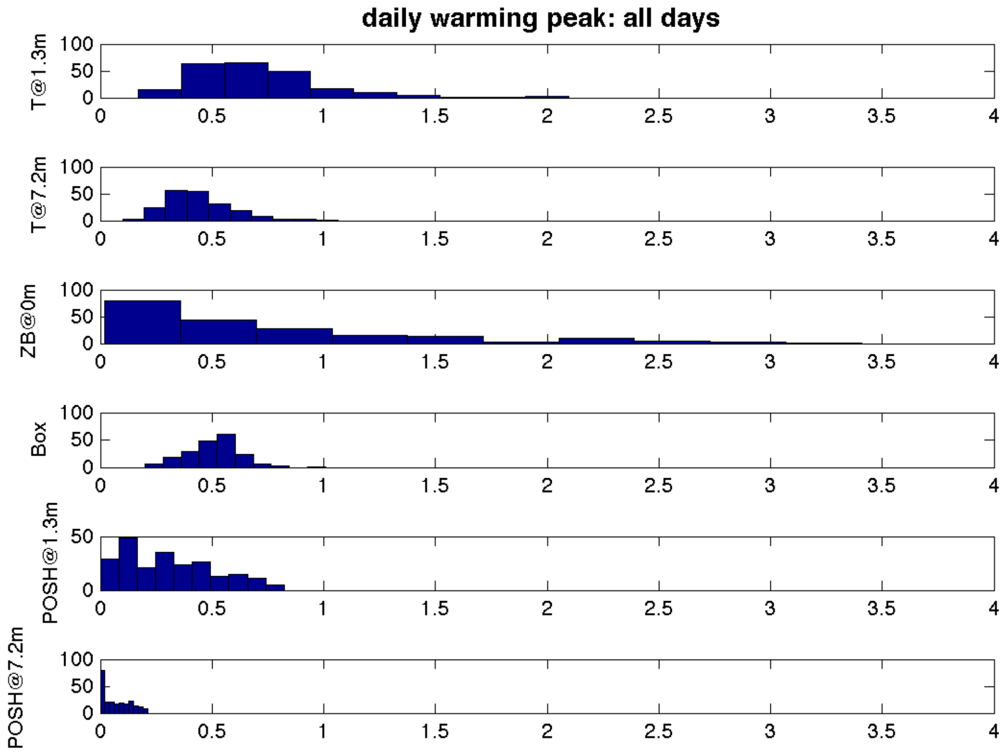

Figure 7.3 Histograms of the daily diurnal warming amplitudes of the logger measurements at 1.3 m (top logger, panel 1) and 7.2 m (bottom logger, panel 2), the ZB modeled surface temperature (panel 3), box model simulated temperature (panel 4), the POSH modeled temperature at 1.3 m (panel 5) and the POSH modeled temperature at 7.2 m (panel 6). X-axis is the daily warming amplitudes in K.

The histograms of the daily diurnal warming amplitudes for various model outputs and measurement data are very revealing.

For measurements at 1.3m, the warming amplitudes mostly range from 0.3 to 1K. There are no days without warming, and the largest daily warming is just over 2K. For the measurements at the deeper 7.2 m depth, the amplitudes mostly range from 0.3 to 0.5K. Again, there are no days with no warming. This is an important trait to notice when comparing to model results.

Histograms of the ZB models show a very different distribution of warming amplitudes. The majority of the days have warming amplitudes smaller than 0.3K, among which a large number of days have minimum warming. At the other end, very large diurnal warming amplitudes occurred on several days with the largest warming approaching 3.5K, much larger than the measured temperature at 1.3m. This obviously corresponds to the low wind days such as day 134 to 136 shown in Figure 7.1.

The histogram of the box model simulations shows a distribution quite similar to the temperature measurements at 7.2m. The warming ranges are within 1K, and not very variable, and every day there is some degree of warming.

For the POSH model, the simulated temperatures at 1.3m are generally smaller than the temperature measurements at the same depths. Particularly, there are many days with the warming amplitudes close to zero. The simulated temperatures at 7.2m are much smaller than the measurements at the same depths, and also much smaller than the simulations at 1.3m. In fact, the simulated daily warming at 7.2m is smaller than 0.1K for 65% of days. Given the fact that the surface temperature from POSH model is usually very large during the low wind condition (figure 7.2), this is an indication that POSH model does not allow enough heat to be transported downwards for our coastal cases, resulting in very large discrepancies in daily warming amplitudes across the depths. According to the measurements, the thermal differences between depths are much smaller, probably due to more energetic vertical mixing at the coastal regions.

### 7.3.2 Distributions of the diurnal warming peak time

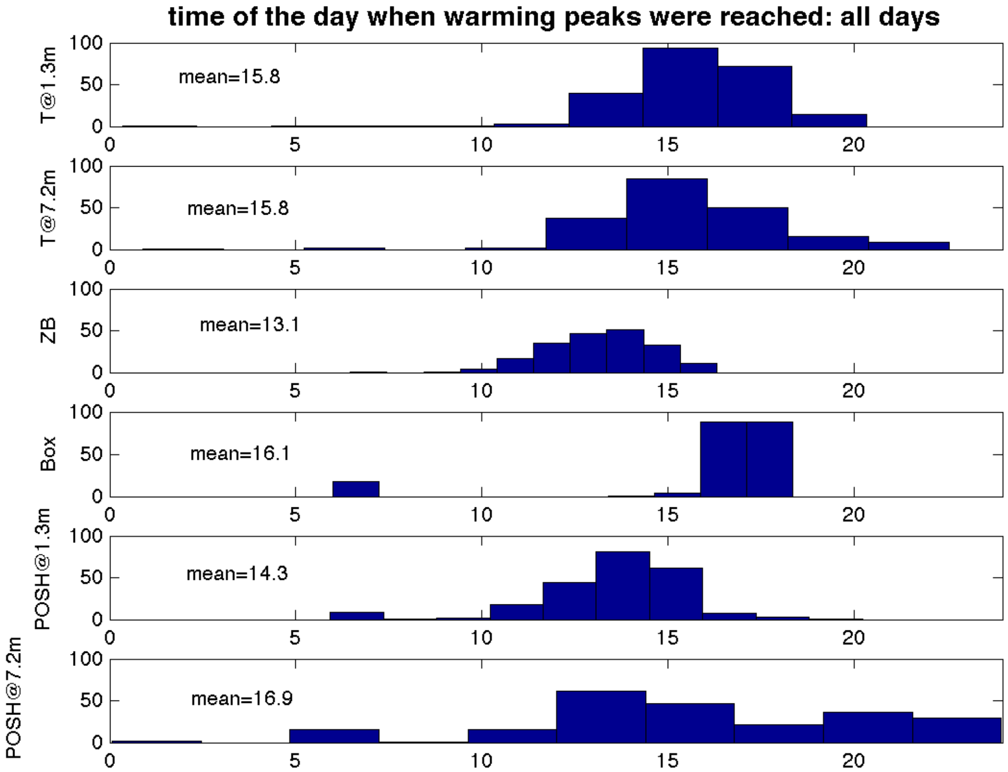

Figure 7.4 Histograms of the daily diurnal peak times of the logger measurements at 1.3 m (top logger, panel 1) and 7.2 m (bottom logger, panel 2), the ZB modeled surface temperature (panel 3), the box model simulated temperature (panel 4), POSH modeled temperature at 1.3 m (panel 5) and POSH modeled temperature at 7.2 m (panel 6). X-axis is the local time.

In this section we compare the distributions of the timing of the daily peaks between measurements and the model results. For the measured data, the shallowest and deepest loggers peaked around the same time. On average, the ZB modeled temperatures tend to reach the daily peak about 2.7 h earlier than the measurements, while the box model, on average, lagged the measurements about 0.3 hours. For the POSH model, the shallower depth simulated temperatures reach the daily peak 1.5 h earlier than the measurements, while the deeper depths simulated temperatures reach the daily peaks about 1 h later than in the measurements. As we can see in the sample cases time series (Figure 7.1), a later peak in diurnal warming in deeper water depths is a common feature shown in the POSH simulations. This reflects the physical mechanism that during the cooling phase, the near surface layers lose heat from the surface and vertical convective mixing transports the heat down, thus the deeper depths continue to rise in temperature, resulting a lag in the warming peak. For this coastal site, this behavior is not seen in the data.

### 7.3.3 Lengths and shapes of diurnal warming and cooling phases

As we have seen in the sample time series (Figure 7.1), the lengths and shapes of the diurnal warming and cooling phases differed greatly between measurements and various model results. For instance, the ZB model predicted a large amplitude and short duration warming curve with an equally short cooling curve, while the cooling curves from the box model are much longer, and of equal or smaller slopes compared to the warming curves.

In this section, we compare these characteristics from each measurement and model cases. First, we chose the ratio of 0.7, to find the local time where 70% of the daily warming peak was reached before and after the daily peaking time, $t_{max}$.

Then we calculate the time between local peak tmax and the local time when 70% warming peak was reached for each day, and plotted the histograms to study the distributions of this time length $L_{up}$ (Figure 7.5 top panel). Similarly, the time, $L_{down}$ between peak and when 70% warming peak was reached during the cooling curves are also plotted (Figure 7.5 middle panel). Finally, we compared the logarithmic ratio of the $L_{down}/L_{up,}$ to illustrate the symmetric features of the warming and cooling curves for measurements and model results (Figure 7.5 bottom panel).

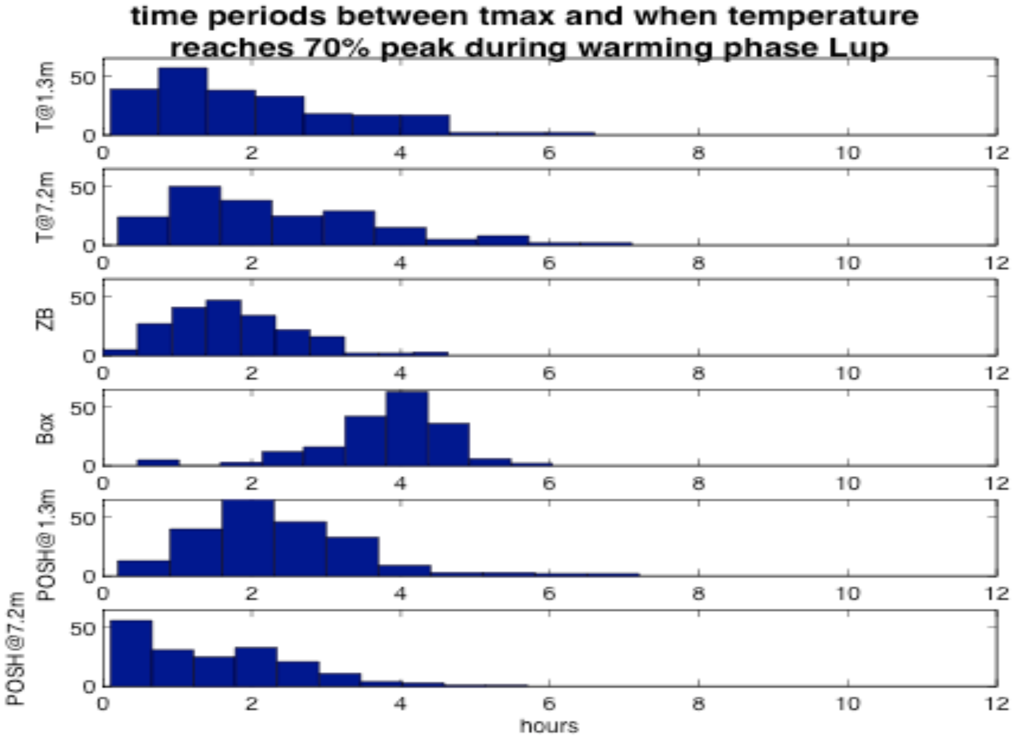

time periods between tmax and when temperature reaches 70% peak during warming phase Lup

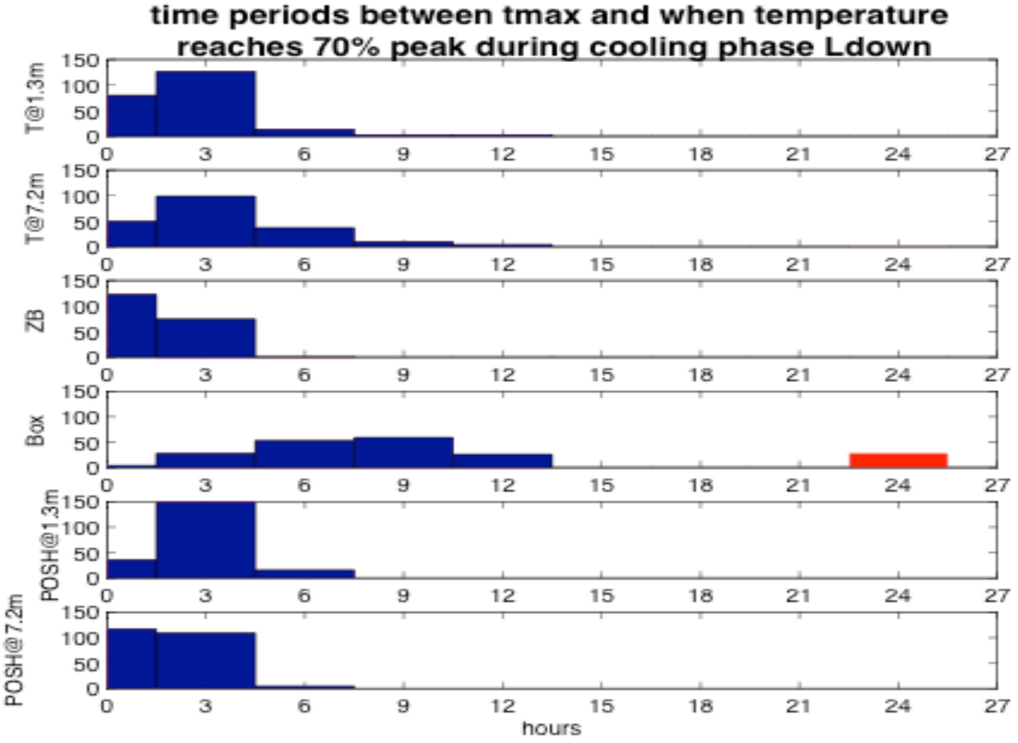

time periods between tmax and when temperature reaches 70% peak during cooling phase Ldown

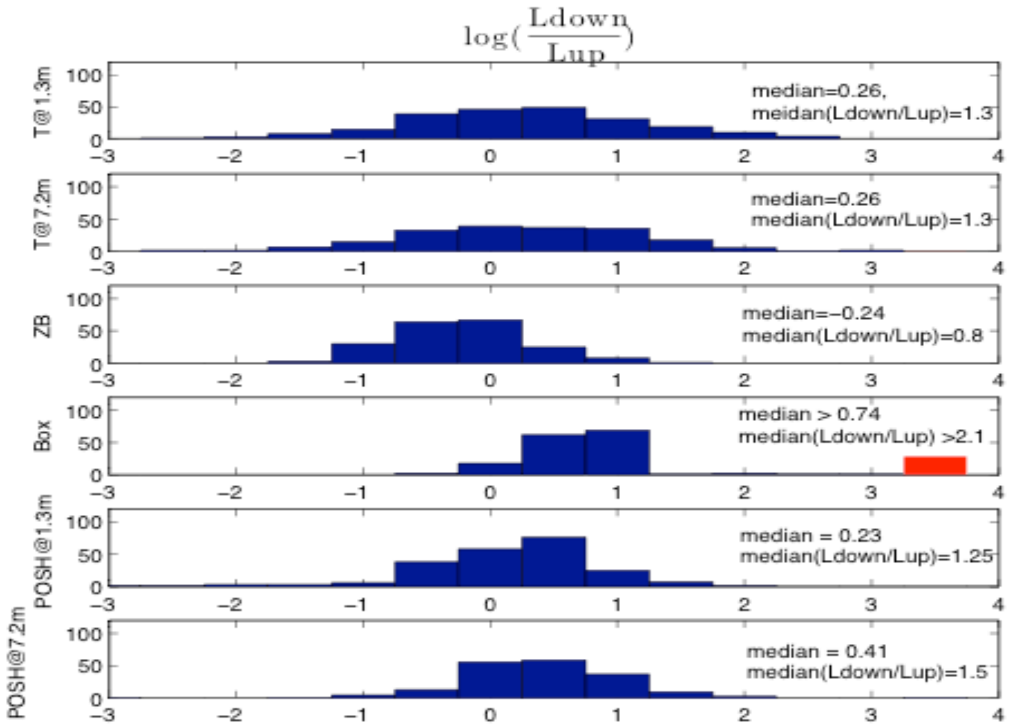

Figure 7.5 Histograms of the diurnal warming and cooling curves. Local time $t_{max}$ is the time when the daily peaks were reached. For the box model plots, the red bars indicated the days where 70% peak were never reached during the cooling phases, before the next day at 6am when the model was reset. X-axis is the value of log ($L_{down}/L_{up}$).

For the warming phase time length $L_{up}$, we noticed all models except box model behaved similarly to the measurement data. The ZB model has fewest extreme cases where the warming takes more than 5 hour. The box model, on average, takes the longest to warm up. The majority of cases took around 4 hours for the box model, as compared to around 2 hours for other models.

For the cooling time $L_{down}$, the box model takes the longest time to cool down; for 19% of the days, 70% of the peak temperatures was never reached during the cooling phase before next day at 6am when the model was reset (red bar in Figure 7.5). This is related to the insufficient cooling we have seen in the sample time series. The ZB model reaches the 70% value the fastest, with an average of 1.4 hour. The POSH model predicts the cool down times reasonably well compared to the measurements. The average $L_{down}$ time length is 2.67 hour and 1.75 hour for 1.3m and 7.2m for the POSH model, as compared to 2.48 hour and 3.45 hour for the measurement data at the same depths.

The ratio $a = \log(\frac{L_{down}}{L_{up}})$ shown in the third panel of figure 7.5 is an indication of the symmetry of the warming and cooling phases. A ratio of 0 indicates the warming and cooling phases are symmetric, by this measure. A ratio of < 0 indicates that cooling is shorter than warming. Only the ZB model has an average faster cooling than warming rate with a median of $\left(\frac{L_{down}}{L_{up}}\right)$ = 0.8. The POSH model compares well to the data. The median value of $\left(\frac{L_{down}}{L_{up}}\right)$is 1.25 and 1.5 for the depth at 1.3m and 7.2m, as compared to the measurement data value of 1.3 and 1.3 for the same depths. The box model has the slowest cooling process, just counting the 81% days during which 70% of warming peaks are reached, the cooling process is 2.1 times of the warming process.

### 7.4 Model adjustment for shallow water cases

During the high wind conditions, the box model gives reasonable results compared to the measurements. However due to the model setup, the box model cannot correctly resolve any thermal stratification. The POSH model can simulate thermally stratified profiles, but the calculated warming is too concentrated in the shallowest meter. The model produced large warming at the surface, and not enough warming at depths when compared to measurements. So, in this section, we first adjust the calculation of POSH diurnal warm layer depth and the thermal profile to test if and how the model performance can be improved for the coastal studies.

We will also attempt to improve the box model performance. While the box model produced the warming amplitudes reasonably well during intermediate to high wind conditions, there is usually excessive cooling during high wind cases, and excessive warming left during intermediate wind cases by the next day at 6am. The relationship between wind speeds and residual warming could be put into an empirical formulation, in order to improve box model performance.

Moreover, the model runs have not considered the effects of the bottom reflection of solar radiation. In this section, we will investigate whether the inclusion of bottom reflection improves the model results.

### 7.4.1 POSH model adjustment

As shown in the model data comparison, the POSH model produced very large warming near the surface, but the warming did not penetrate down enough when compared with shallow water data. Two items can be altered in the model formulation to increase the warming at depth. The first adjustment is to increase the diurnal warming depth $D_T$. The second is to change the vertical shape of the warming profile, so that more heat is transported deeper.

Another common problem for the shallow water case in the model formulation is that the diurnal warming depth is often larger than the actual water depth, especially during the cooling phases. As the original POSH model does not consider any bottom, using the original modeled profiles for the shallow water means simply neglecting any heat at the depths lower than water depth. In this section, we devise a method to take into account bottom effects in POSH:

a) Change the vertical temperature shape of the wind dependence by increasing the value of a in Table 6.1 and equation 6.2 (Table 7.2, Figure 7.6).

As shown in Figure 7.6, the larger a value in the $\Delta T(z) = e^{-9.5\left(\frac{z}{D_T}\right)^a}$ formulation results in a well-mixed near surface layer and larger thermal gradient near the bottom of $D_T$. For the same $D_T$ value, heat is concentrated closer to the bottom.

| wind speed (ms$^{-1}$) | original values of a | new values of a |
|---|---|---|
| <=1.5 | 2 | 15 |
| 3 | 3 | 15 |
| 4.5 | 5 | 15 |
| 6 | 7 | 30 |
| >=7.5 | 9 | 50 |

Table 7.2 Increased values of a in the vertical thermal profiles in POSH.

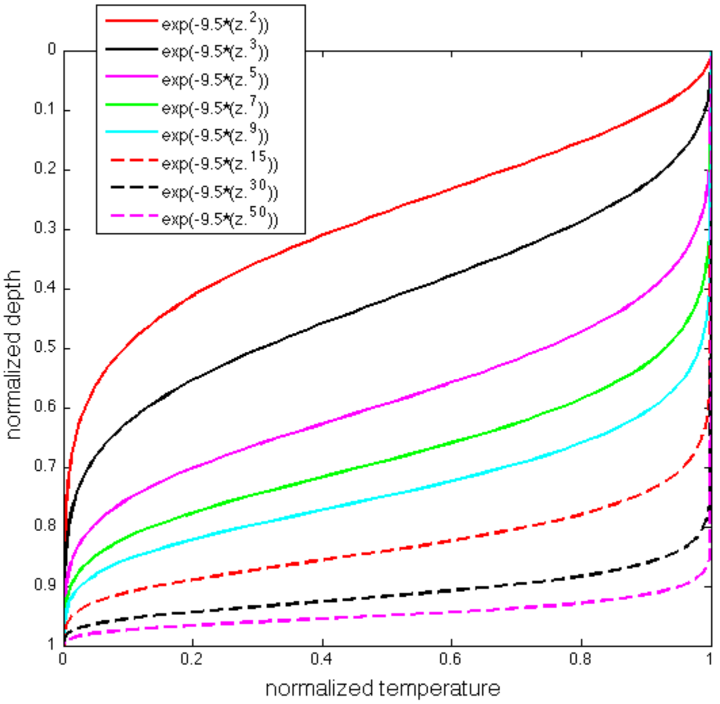

Figure 7.6 The normalized vertical temperature structure of diurnal warming $\Delta T(z) = e^{-9.5\left(\frac{z}{D_T}\right)^a}$ for values of $\alpha$ ranging from 1 to 50. The y-axis is the normalized depth $D/D_T$.

b) Well mixed bottom assumption

For situations where $D_T$ is larger than water depth, we calculate a well-mixed bottom layer from depth z to the bottom depth. The depth z is determined so that the heat content between z and bottom depth equals to the heat from z to the $D_T$ in the original POSH calculation, i.e. heat is conserved in the water column.

c) Simply increase the diurnal warming depth $D_T$

The diurnal warm depth is calculated as $D_T = \sqrt{\frac{2R_i c_p}{\alpha g \rho}} \frac{\tau_{ac}}{\sqrt{Q_{ac}}}$, where $\tau_{ac}$ is the accumulated wind stress, which represent the mechanical turbulence mixing by wind. In the coastal region, vertical turbulence mixing is generally stronger than in the open ocean due to the tidal mixing, the existence of the bottom or mixing from wave breaking. So we adjusted the model by increasing $D_T$ to say $1.5D_T$, which is an arbitrary number at this point, just to check quantitatively how the increase impacts the warming profile.

d) Combine the increase of $D_T$ and well-mixed bottom layer calculation

The last adjustment basically combined the increase of $D_T$ to $1.5D_T$ and the mixed bottom layer calculation.

The modeled time series after four types of adjustments as listed above in comparison with the in-situ data and original POSH model runs are shown in figure 7.7.

For the intermediate wind cases, we examine day 130 to day 133. The measured warming is ~0.5K, and the temperatures at all the measure depths are similar. The original POSH model produced ~0.5K warming at the depths of the three near-surface thermometers. The model predicted large thermal stratification, with ~0.2K warming at 4.6 m and no warming at 7.2 m. Changing the profile coefficient resulted in smaller simulated warming near the surface, but the thermal stratification issue remained, so it is worse than the original model results. The mixed bottom assumption returns very similar results to those of the original model, with slight warming at 7.2 m. This is probably because during intermediate and low wind condition, the diurnal warm layer, $D_T$, is generally less than the water depth, thus there is little difference from the original model runs. The model results improved significantly with the increase in the $D_T$ value, with the warming at 4.6 m increasing to almost 0.5K and at 7.2 m by ~0.2K. The last method, which combines the increased $D_T$ and bottom mixed layer, improves the results even more.

For the low wind cases, we look at day 134 to day 136. The measured warming at the three near surface depth is ~1K with slight stratification among them and ~0.5K warming at 4.6 m and 7.2 m. The original POSH model overestimated the warming at the surface (shown in Figure 7.2), but significantly underestimated the warming at the sub-surface depth with only 0.5K at the top three logger depths. Changing the profile coefficient caused the warming to be even lower, thus making it worse. Assuming a well mixed bottom boundary layer did not improve the results either, as the diurnal warm layer depth $D_T$ is never larger than the water depth. Again, increasing $D_T$ helps the most in terms of increasing the warming amplitudes at near-surface depths and 4.6m. However, it predicts no warming at 7.2m, whereas some warming (~0.5K) was measured.

To summarize, among the adjustments to POSH model for the low and intermediate wind conditions, increase the diurnal warm depth $D_T$ is mostly effective, though it still could not predict warming near the bottom. A well-mixed bottom layer itself does not improve the model results significantly, but combining it with the increased $D_T$ provides the best model improvements. Changing the coefficient in the temperature vertical profile formulation makes the simulations further from the measurements.

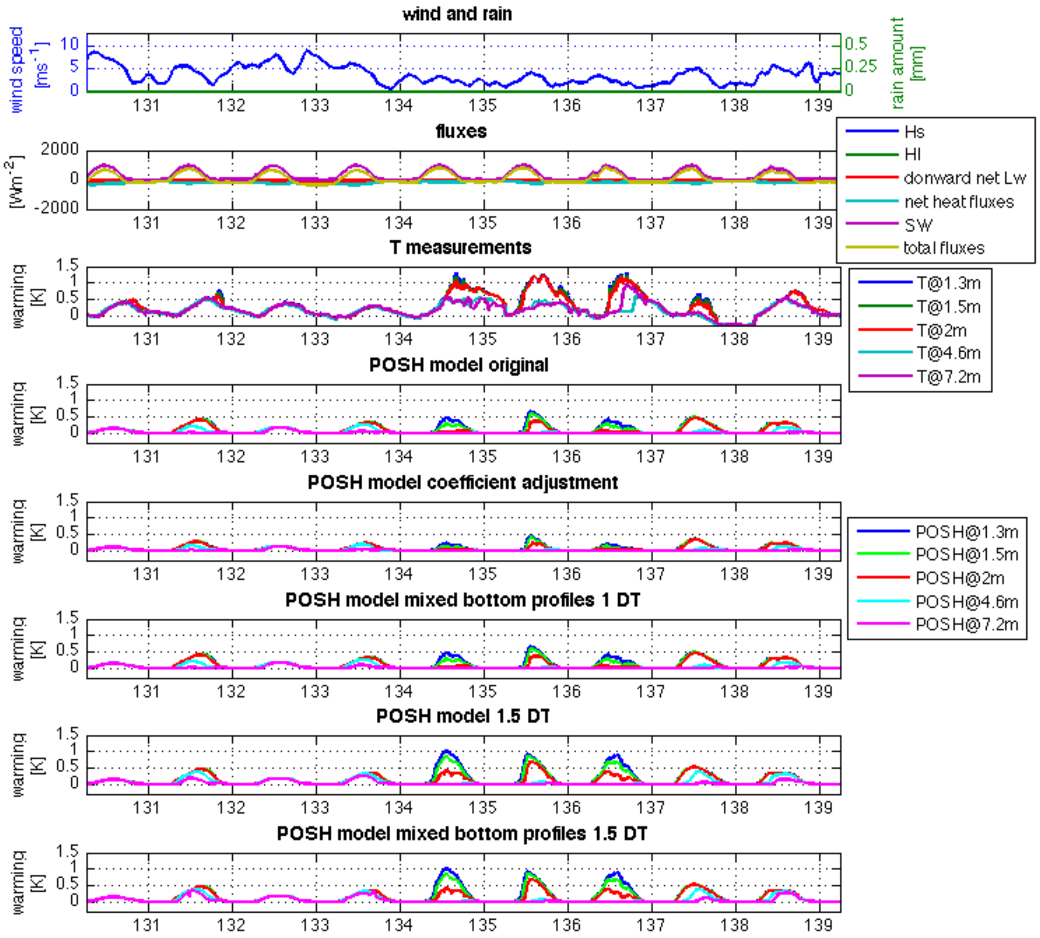

Figure 7.7 Time series of temperature measurements and POSH original and adjusted model output. X-axis is the year day in 2011. The top panel is wind speed in ms$^{-1}$ and rain amount in mm. The second panel shows sensible heat flux Hs, latent heat flux Hl, downward net longwave flux, net surface heat fluxes (=Hs+Hl+net longwave), shortwave radiation SW, and total heat fluxes, all in unit of Wm$^{-2}$. The third panel shows the temperature measurements at 1.3 m, 1.5 m, 2 m, 4.6 m and 7.2 m. The fourth panel shows the original POSH model output at 1.3 m, 1.5 m, 2 m, 4.6 m and 7.2 m. The fifth panel shows the modified POSH output with the profile coefficient a altered (Table 7.2). The sixth panel shows the modified POSH output assuming a well-mixed bottom layer. The seventh panel shows the modified POSH output with diurnal warm layer depth $D_T$ increased to 1.5 times. The bottom panel shows modified POSH output with increased diurnal warm layer depth $D_T$ and well-mixed bottom layer.

### 7.4.2 Box model adjustment

While the box model produced reasonable amplitudes of warming during the intermediate and high wind speeds, there are usually excessive modeled warming by the end of the diurnal warming day (6am next day) for days with weak to intermediate wind speeds ($U_{max}$<$9ms^{-1}$), and excessive modeled cooling for days with high wind speeds ($U_{max} \geq 9ms^{-1}$).

It is found that the end-of-day warming/cooling discrepancies between model outputs and measurement data are closely linked to the wind speeds. Because of the relationship, it is possible to devise a box model correction term based on wind speeds. Moreover, if we look at the averaged wind speeds, the averaging periods from 4pm to next day 6am, and the averaging periods from 0am to 6am, produced similar relationships between residual warming and average wind speeds (Figure 7.8). Given the similarity, from a modeling point of view, it is beneficial to use the averaging periods from 0am to 6am, as shorter time ranges means less requirements for wind data measurements. Thus we will use the wind from 0am to 6am to derive the empirical model correction term.

Using a linear relationship, the simple formulation linking residual warming and average wind speeds is

$$T_{residual} = -0.0601 * wind + 0.485 \qquad \text{equation 7.1}$$

where $wind_{avg}$ refers to wind averaged over 0am to 6am next day, and $T_{residual}$ is the temperature difference between the modeled temperature and measurement at 6am next day. The mean standard error of this linear fit is 0.025K.

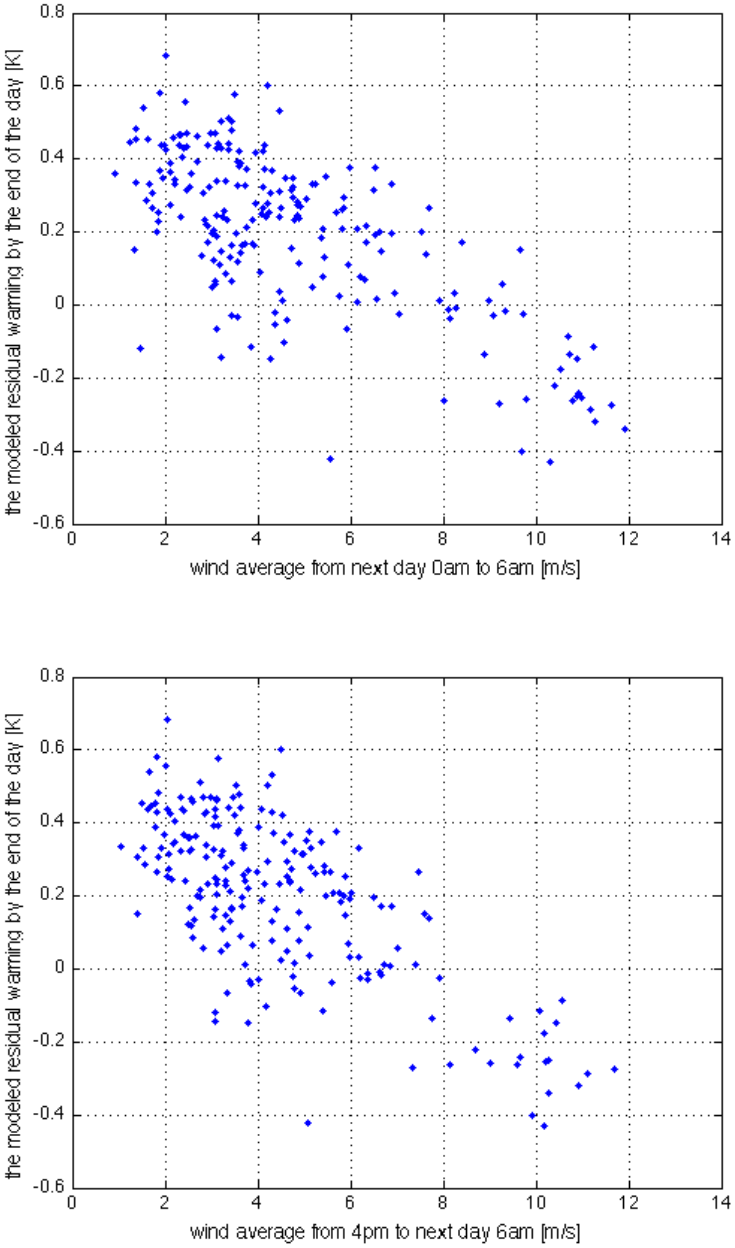

Figure 7.8 The scatter plots of the end-of-day warming discrepancy versus averaged wind speed for a certain time periods later in the day. Note one diurnal warming day is defined as from 6am to 6am next day. The y-axis is the residual warming of the box model simulation by the end of the day compared to measurement data. The x-axis is average wind speed value for the given periods. The upper plot shows the averaged wind speed from the 0am to 6am, while the lower plot shows the averaged wind speed from the 4pm to next morning 6am.

The correction is then added to each hour after $T_{max}$ was reached, i.e., during the cooling phase. Assuming the cooling curve resembles a straight line starting from $T_{max}$ at $t_{max}$ to

$T_{residual}$ at 6:00 next day for the modeled output, while the "correct" cooling curve resembles a straight line starting from temperature $T_{max}$ at local time $t_{max}$ to 0 (no warming, clean slate) at next day 6:00 as the desired output. Then

$$T_{correct} = \frac{(30 - t) * T_{\max}}{30 - t_{\max}} \qquad \text{equation 7.2}$$

and

$$T_{\text{modeld}} = T_{\max} - \frac{(t - t_{\max}) * (T_{\max} - T_{residual})}{30 - t_{\max}} \qquad \text{equation 7.3}$$

where t is the local time ranging from $t_{max}$ (local time of the daily warming peak) to 30 (next day at 6:00).

Thus the empirical correction term for the box model is

$$\Delta T(t) = T_{correct}(t) - T_{\text{modeled}}(t) = -\frac{(t - t_{\max}) * T_{residual}}{30 - t_{\max}} \qquad \text{equation 7.4}$$

Figure 7.9 shows how well the warming/cooling biases are corrected after applying the correction.

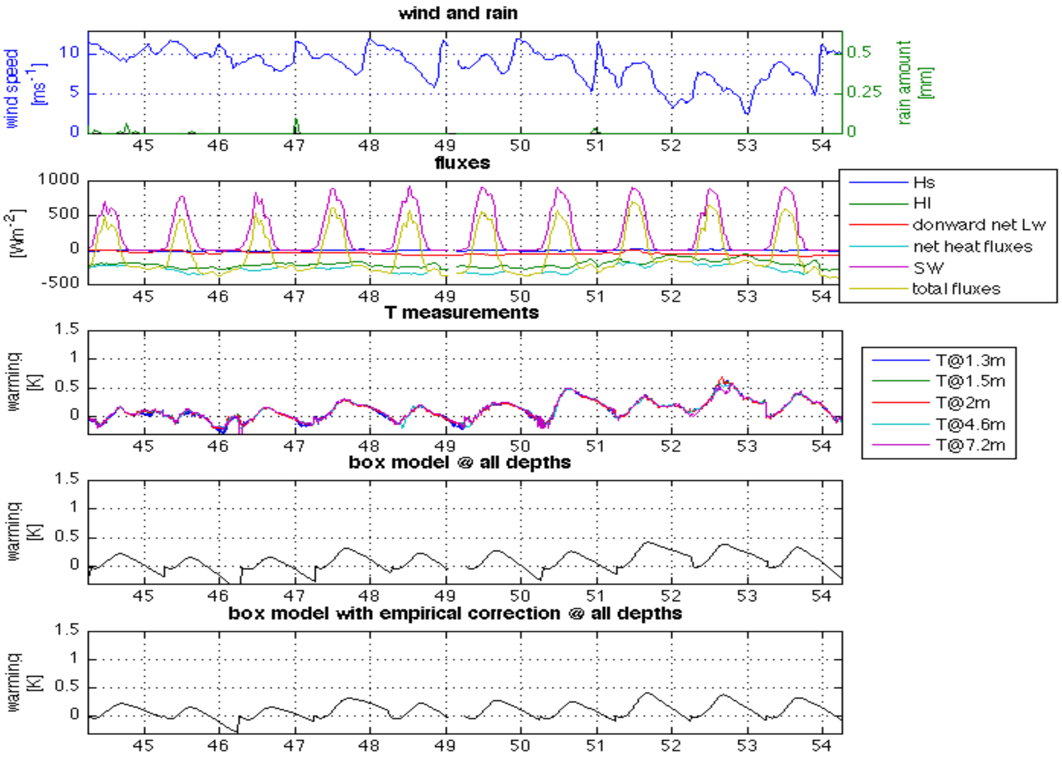
wind and rain
wind speed [ms$^{-1}$]
rain amount [mm]
0
5
10
0
0.25
0.5
45 46 47 48 49 50 51 52 53 54
fluxes
[Wm$^{-2}$]
1000
500
0
-500
Hs
Hl
donward net Lw
net heat fluxes
SW
total fluxes
T measurements
warming [K]
1.5
1
0.5
0
T@1.3m
T@1.5m
T@2m
T@4.6m
T@7.2m
box model @ all depths
box model with empirical correction @ all depths

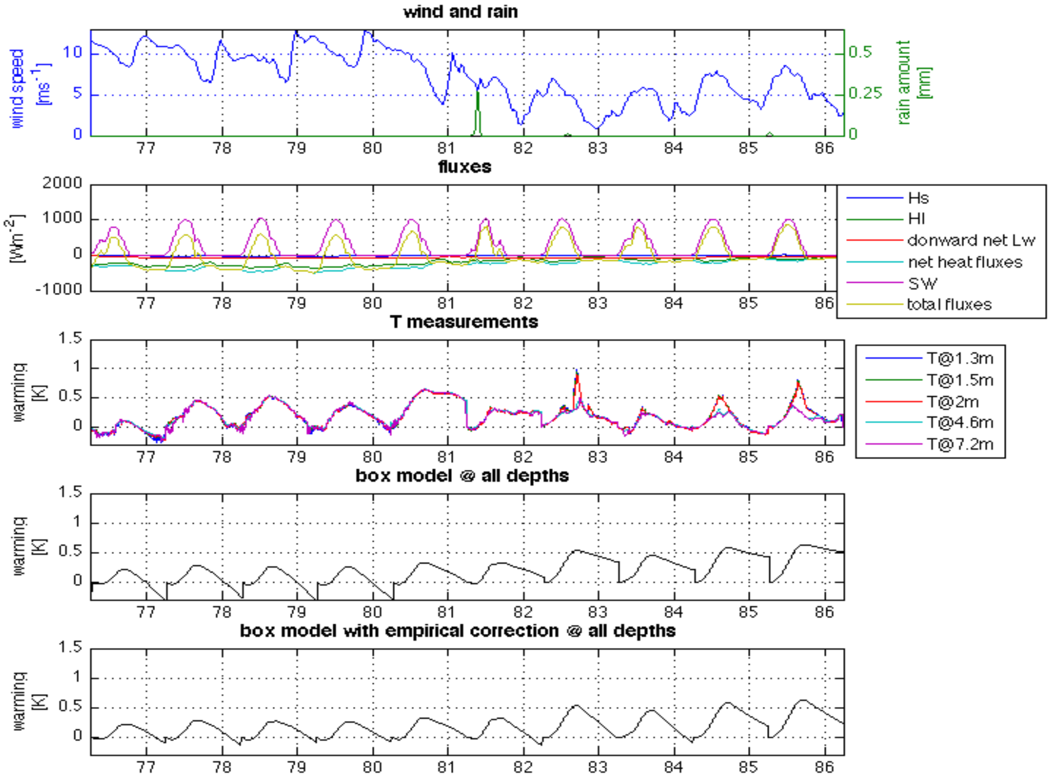
wind and rain
wind speed [ms$^{-1}$]
rain amount [mm]
0
5
10
0
0.25
0.5
77 78 79 80 81 82 83 84 85 86
fluxes
[Wm$^{-2}$]
2000
1000
0
-1000
Hs
Hl
donward net Lw
net heat fluxes
SW
total fluxes
T measurements
warming [K]
1.5
1
0.5
0
T@1.3m
T@1.5m
T@2m
T@4.6m
T@7.2m
box model @ all depths
box model with empirical correction @ all depths

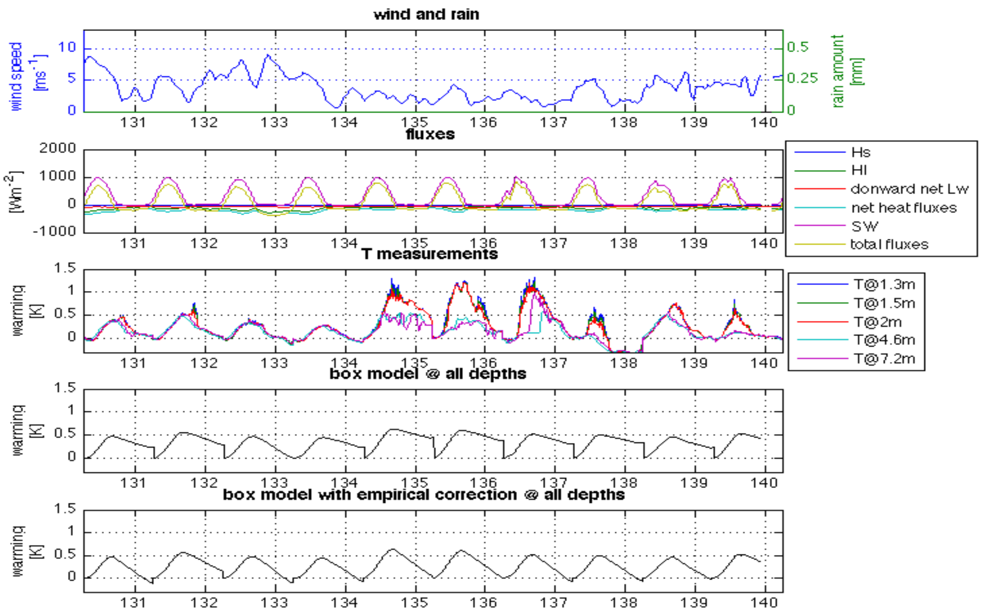

Figure 7.9 The time series of the box model original output versus the output after adding the empirical corrections.

## 7.5 Concluding remarks

In this chapter, the three models described in Chapter 6 are used to simulate the warming at the Little Cayman station, and the results are compared with in-situ measurements. We found that ZB model either produced warming of very large amplitudes (2-3 times of the measurements) during low wind cases, or almost no warming during high wind and intermediate wind cases. The simple “box model” simulates daily warming amplitudes in moderate (5 $ms^{-1} < U_{max} < 9ms^{-1}$) and high wind ($U_{max} \geq 9ms^{-1}$) conditions well, but cools too quickly in high winds and too slowly in moderate winds. POSH model produced best results among three models during low wind conditions ($U_{max} \leq 5ms^{-1}$), but too much heat is concentrated near the surface, while not enough heat propagates down. Empirical adaptations are made for POSH and box models, leading to some improvement in their performance. Further improvements will require higher vertical resolution of temperature measurements, as well as information on bottom fluxes.

# Chapter 8 Satellite and in-situ temperatures in the Great Barrier Reef region

Coastal thermal features, such as diurnal warming and its implications on coastal ecosystems, are most conveniently studied by remote sensing techniques. Sea surface temperature is one of the most mature satellite products and among the most important atmospheric-oceanic variables for oceanic environments monitoring. With the increasingly higher spatial and temporal resolution, satellite SST is becoming more suited to study coastal features. The goal of this chapter is to assess the accuracy of various satellite SST products by comparing them with in situ temperature measurements, to explore various dependence of the bias errors, including coastal features, as well as to examine the diurnal warming features in the satellite data, especially those from geostationary satellites, and to determine whether they are appropriate to predict the temperatures at the depths of the corals.

## 8.1 Materials and methods

### 8.1.1 Satellite data

The satellite SST extracted for the study is for the Great Barrier Reef region, and for the periods of January 1st to April 30th, 2010, which is during summer and autumn seasons in the Southern Hemisphere.

The SST data we use are partly from the comprehensive “TWP+” dataset, which is designed to facilitate the study of the diurnal warming in the tropical warm pool region; data are available for January to April in 2009 and 2010 (https://www.ghrsst.org/ghrsst/tags-and-wgs/dv-wg/twp/). For our coastal studies, 0.02°

twice-daily SST's derived from measurements of the AVHRR's on polar orbiting NOAA 17, 18, 19 satellites and 0.05° latitude and longitude, hourly fields from the geostationary MTSAT were used, both in Level 3 format (Table 8.1). The SST data have been validated against temperatures from local drifting buoys and moorings, and their regression algorithms were adjusted accordingly. The resulting sub-surface SST is then converted to skin SST by simply subtracting a constant 0.17 K, following an algorithm used in Pathfinder SST (Helen Beggs, Australian Bureau of Meteorology, personal communications). In addition, level-2 MODIS 1km Aqua and Terra data were obtained from NASA's OceanColorWEB data archive (http://oceandata.sci.gsfc.nasa.gov/).

| Data platform and processing level | Temporal resolution | Spatial resolution |
|---|---|---|
| MODIS Aqua, level 2 | Twice a day. Satellite overhead time (SOT) is at about 1:15 and 13:40 local time (LT), but changes a little from day to day. Different stations also vary a little | 1km |
| MODIS Terra, level 2 | Satellite overhead time (SOT) is at about 10:50 and 22:10 UTC | 1km |
| NOAA17, level 3 | SOT is about at 9:20 and 21:00 LT. | 0.02° |
| NOAA18, level 3 | SOT is about at 1:45 and 13:55 LT. | 0.02° |
| NOAA19, level 3 | SOT is about at 2:00 and 14:40 LT. | 0.02° |
| MTSAT1R | Every hour | 0.05° |
| In-situ loggers | 10 minutes (30 for Cleveland Bay) | n/a |

Table 8.1 Spatial and temporal resolution of the satellite and in-situ datasets.

### 8.1.2 In-situ stations

Nine in-situ locations are used to compare with satellite SST data for the same time period. Among them, Davies Reef, Cleveland Bay, and Myrmidon Reef are also located near an automatic weather station (AWS), and thus there are also measurements of weather conditions, including air temperature, wind information (speeds and directions) and light measurements (PAR). The other six stations are located to the southern end of

GBR. The station names are Barren Island (BARRSL1), Elusive Reef (ELUSIVEFL1 and ELUSIVESL1), Half Tide Rocks (HALAWS), North Keppel Island (NKEPPSL1) and Pelican Island (PELFL1). The in-situ data at each station are from the bottom-mounted loggers, thus their depth varies.

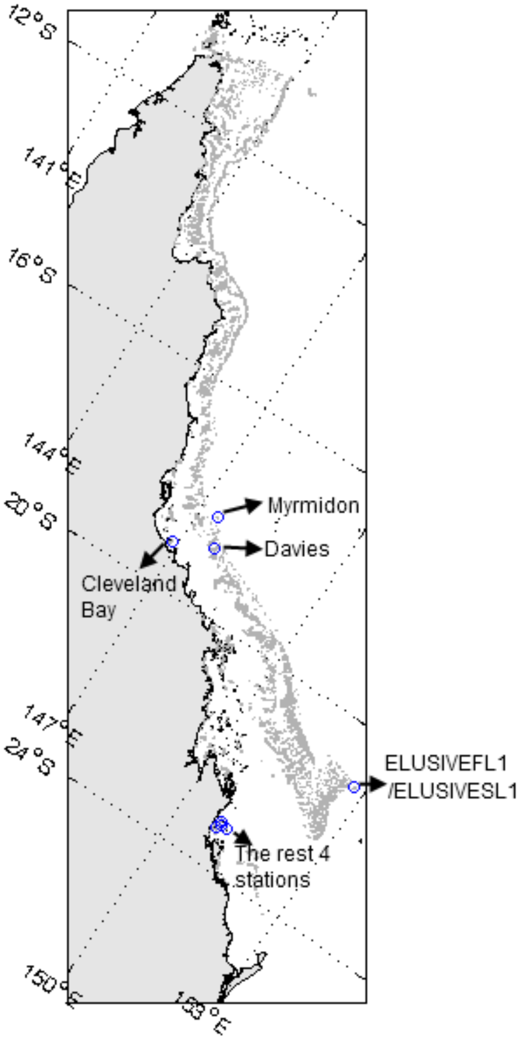

Figure 8.1 Maps for the 9 in-situ station sites, for which the satellite SST were extracted.

### 8.1.3 Matchup procedure

For each in-situ station, the satellite SST data were extracted. For NOAA 17/18/19 L3 composite data, the nearest pixel is first examined. If there were no SST data available (most likely due to cloud cover), the search radius was expanded, so that the pixels with the latitude and longitude no larger than 0.02° from nearest pixel were used. SST data from those pixels were used if available. For the MTSAT data, SST from the nearest pixel is used if available. For MODIS L2 swath data, SST was extracted for the in-situ data if there is a pixel within 0.01 degree both in latitude and longitude from the station.

When extracting the SST, we selected pixels with a quality flag no smaller than 3 (value 3, 4 and 5 with 5 being highest quality) from NOAA AVHRR SST. For MTSAT, we use pixels with the proximity quality flags no smaller than 5, i.e., the best quality cloud free pixels. The value of the proximity flag is here defined as numbers of pixels from the nearest cloud (Leon Majewski, Australian Bureau of Meteorology, personal communications). For example, a pixel with the proximity flag of 5 means the nearest cloud is 5 pixels, i.e., 20km away. For MODIS, the quality flag values are different. A smaller value means less chance of cloud contamination (0 is best quality, 5 is worst quality). We only chose the pixels with quality flag values of 0 and 1. The number of resulting SST matchups for each in situ station is shown in Table 8.2. Each polar orbiting satellite has a total of matchups between 300 and 400. Cleveland Bay has far fewer matchup points due to its proximity to the land, which is only about 13 km away. MTSAT has 3287 matchup points combining all stations.

| In-situ stations | Latitude | Longitude | depth (m) | Number of SST data points for the 4-month/120-day periods | | | | | |
|---|---|---|---|---|---|---|---|---|---|
| | | | | NOAA 17 | NOAA 18 | NOAA 19 | MODIS Aqua | MODIS Terra | MTSAT |
| Davies Reef | -18.807 | 147.669 | 4.4/9 | 47 | 45 | 30 | 67 | 72 | 433 |
| Myrmidon Reef | -18.258 | 147.382 | 7/19 | 42 | 36 | 32 | 43 | 89 | 380 |
| Cleveland Bay | -19.122 | 146.880 | 0 | 14 | 11 | 7 | 0 | 0 | 448 |
| BARRSL1 | -23.158 | 151.071 | 9 | 50 | 64 | 49 | 26 | 35 | 361 |
| ELUSIVEFL1 | -21.104 | 152.765 | 2 | 43 | 55 | 49 | 86 | 67 | 454 |
| ELUSIVESL1 | -21.104 | 152.765 | 10 | 43 | 55 | 49 | 86 | 67 | 454 |
| HALAWS | -23.154 | 150.938 | 6.5 | 33 | 39 | 35 | 48 | 42 | 251 |
| NKEPPSL1 | -23.086 | 150.903 | 8 | 31 | 48 | 43 | 7 | 11 | 274 |
| PELFL1 | -23.239 | 150.874 | 4 | 41 | 61 | 46 | 66 | 55 | 232 |
| Total Matchup points for each satellite | | | | 344 | 414 | 340 | 429 | 438 | 3287 |

Table 8.2 Number of good quality SST data points extracted from different satellite platforms at each in-situ location for the 120-day study periods.

## 8.2 Comparing in-situ temperature and SST: sample time series and statistics

In this section, we compare SST from different satellite instruments with the in-situ data.

### 8.2.1 Sample time series

Sample SST and in-situ temperature time series for a 20-day time period are shown for each station in Figure 8.2. SST from different satellite instruments compare well with the in-situ temperature data. For most stations, there are more SST measurements during days 62 to 68 of 2010 than other time periods. These are “clear sky” days where cloud contamination was absent. For the purposes of our diurnal warming study, we focus on these days.

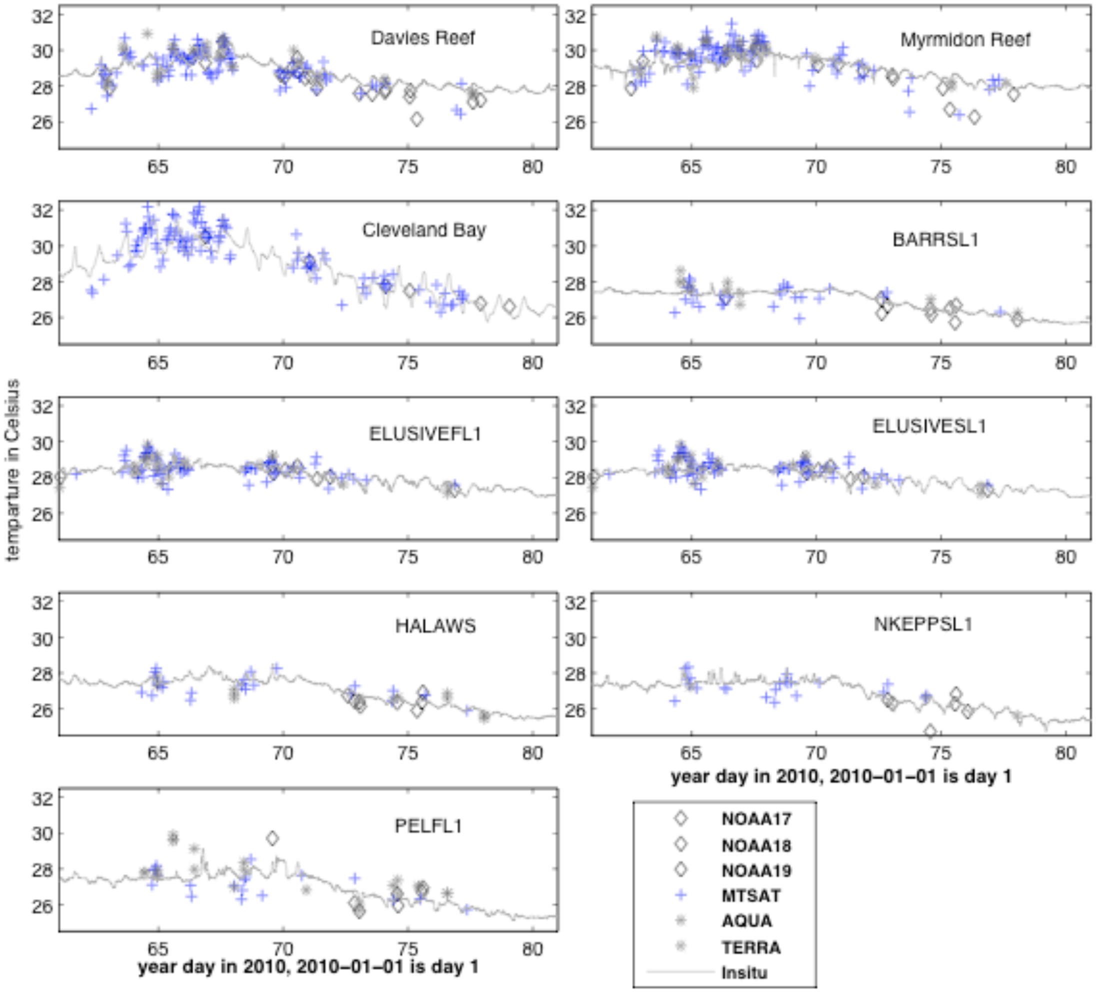

Figure 8.2 SST and in-situ temperature at each station for a sample 20-day period. SST from NOAA1-7, -18, and -19 are all shown as diamond symbols. SST from both MODIS Aqua and Terra satellite are shown as star symbols.

### 8.2.2 Comparison of satellite-derived SST and in-situ temperature

The mean differences between SST from different satellites and in-situ data are small, with values no larger than -0.14 K, except for NOAA-17. The standard deviations are all smaller than 0.75 K, which are better than or comparable to similar coastal validation results (Li et al 2001, Park et al 2014, Xu and Ignatov 2014). It is also interesting to notice that for similar satellites (NOAA series or MODIS series), the morning overpassing satellites (NOAA-17 or MODIS Terra) have a larger negative bias when compared to in-situ data than the afternoon overpassing satellites (NOAA-18, -19 or MODIS Aqua). This result is likely due to the effect of the diurnal warming. The surface temperature (SST) during afternoon is warmer than the measurement data at depths, whereas during the morning hours, the difference is small or zero. The biases are also shown to be quite stable throughout the in-situ temperature ranges (Figure 8.3).

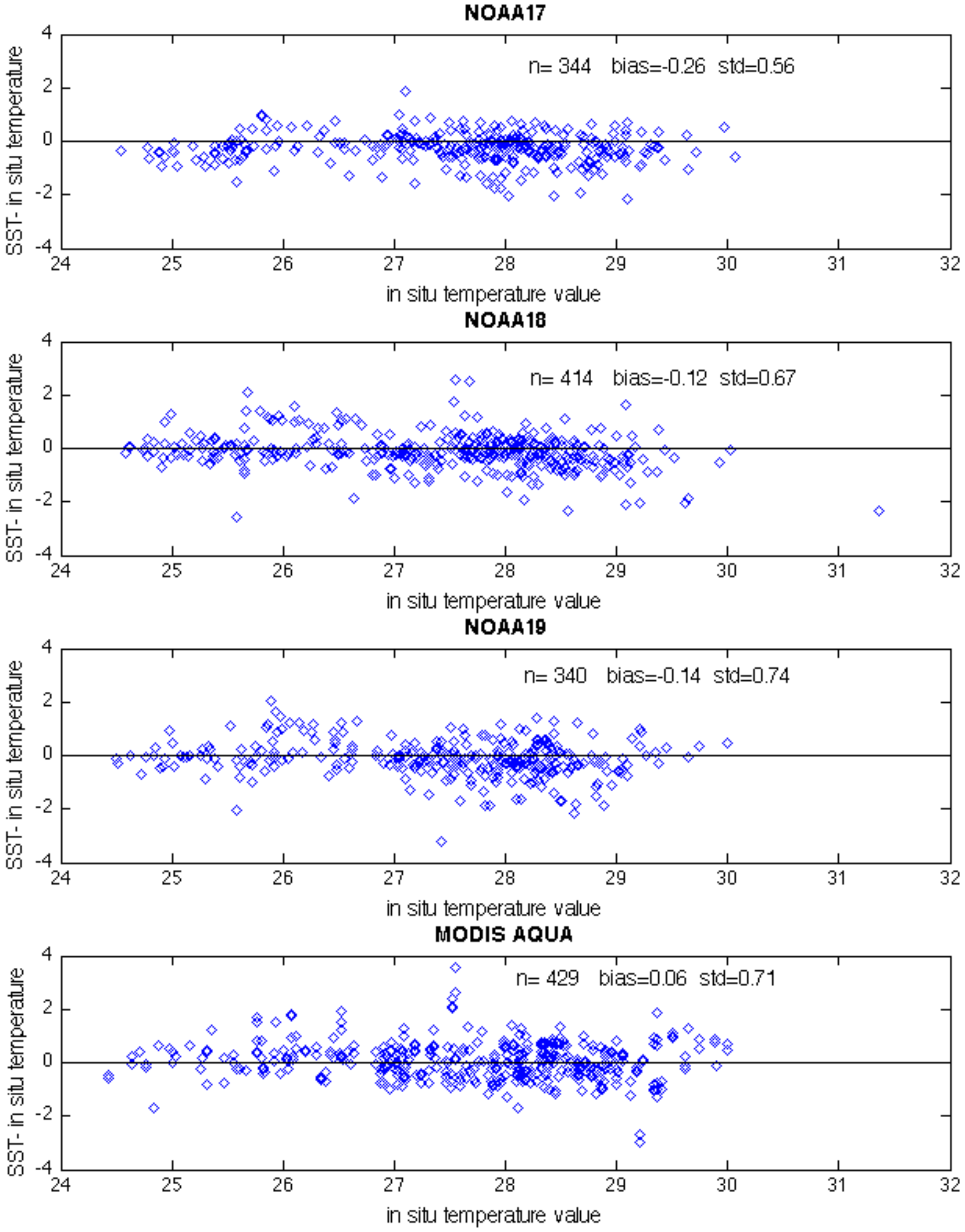

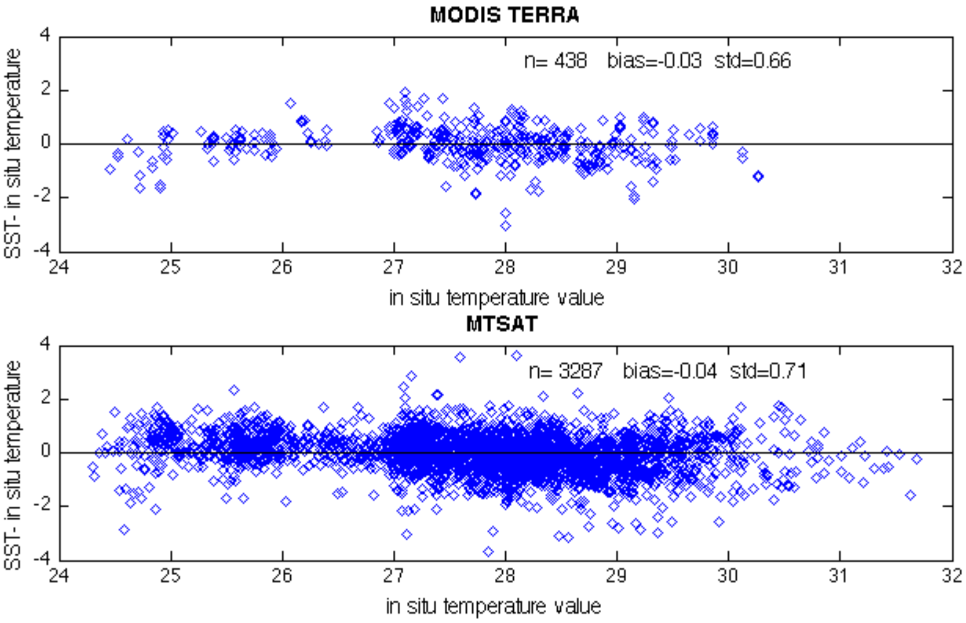

Figure 8.3 Comparisons of differences (satellite – insitu SST) as a function of the in-situ SST for each satellite instrument. The number of data points, bias and standard deviation are given in each panel.

The polar orbiting satellites pass each station location twice a day, once during the day and again at night. Thus, it is useful to calculate the statistics for day and night separately (Figure 8.4). The daytime is defined here as from 6:00 to 18:00 local time, while the nighttime is from 18:00 to next day 6:00. Since all the locations are within 25° from the equator, the annual change of the sunrise/sunset time is small. For all the satellites except MODIS Terra, the nighttime temperature standard deviation is smaller than during the daytime. NOAA-17 has much more negative bias during daytime than nighttime. The reason is that NOAA-17 has an overpass time of ~9:20 during the day and ~21:00 at night. For a typical day when the diurnal warming is present, the ocean heats up gradually in the morning, and often the warming remains well after mid-night. This might explain why the daytime bias is smaller than nighttime bias for NOAA-17. Given that NOAA-18 and NOAA-19 have a daytime overpass in early afternoon, we expect the daytime bias to be larger than nighttime bias. However, the day night bias differences are quite small for both NOAA-18 and NOAA-19. The daytime bias is slightly smaller than the nighttime bias for NOAA-18, and the daytime bias is slightly larger than the nighttime bias for NOAA-19. For MODIS Aqua and Terra, the daytime bias is much larger than the nighttime bias.

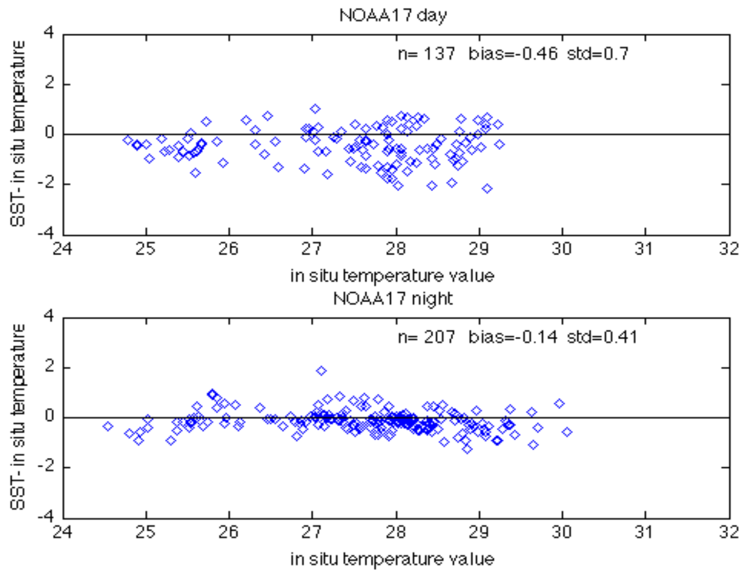

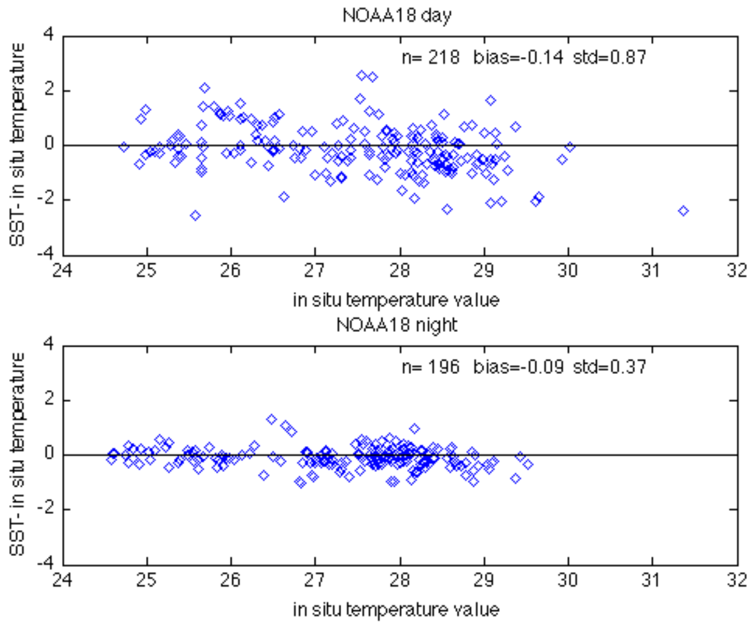

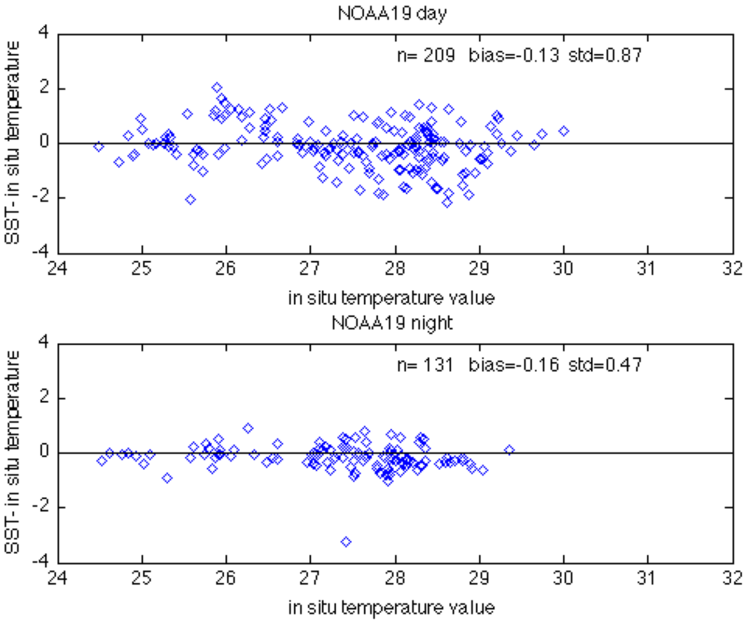
NOAA19 day
n= 209 bias=-0.13 std=0.87
SST- in situ temperature
in situ temperature value
NOAA19 night
n= 131 bias=-0.16 std=0.47
SST- in situ temperature
in situ temperature value
4
2
0
-2
-4
24
25
26
27
28
29
30
31
32

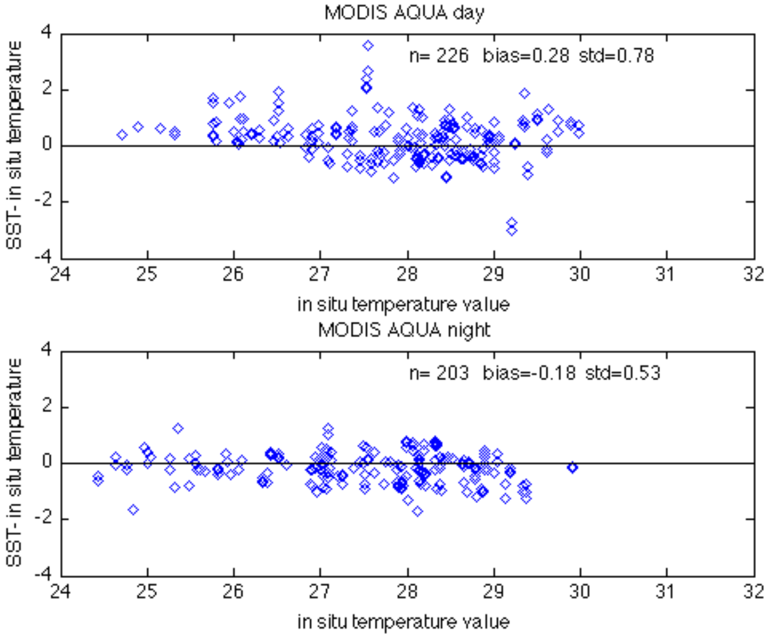
MODIS AQUA day
n= 226 bias=0.28 std=0.78
SST- in situ temperature
in situ temperature value
MODIS AQUA night
n= 203 bias=-0.18 std=0.53
SST- in situ temperature
in situ temperature value
4
2
0
-2
-4
24
25
26
27
28
29
30
31
32

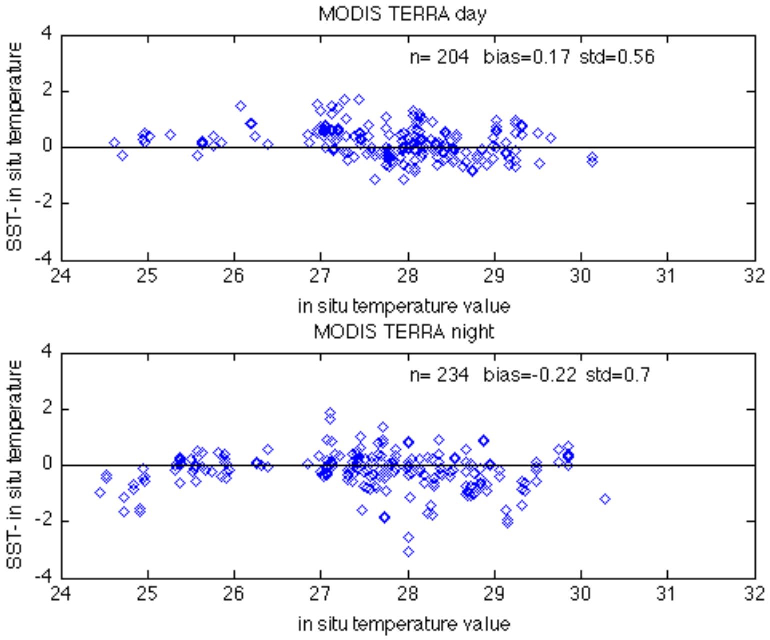

Figure 8.4 Comparisons of daytime and nighttime differences (satellite – insitu SST) as a function of the in situ SST for each polar orbiting satellite platform. Note that the day night is defined as from local time 6:00 to 18:00. The number of data points, bias and standard deviation are also given.

## 8.3 Diurnal warming signals

Having shown that satellite-derived SST's are of reasonable accuracy when compared with in-situ data, we next explore their use to study the diurnal warming at the GBR.

### 8.3.1 Diurnal warming signals in satellite-derived SST's

To examine whether satellite-derived SST's exhibit diurnal warming cycles, hourly bin-averaged SST and the related 95% confidence intervals were calculated (Figure 8.5). We found that for several stations, including Davies Reef, Myrmidon Reef and Cleveland Bay, the SST data from geostationary satellite MTSAT show clear diurnal warming cycles. For these stations, daily maximum temperatures occur around 13:00 to 14:00, while the lowest temperatures occur around 6:00, which is similar to previous findings for the open ocean (e.g. Gentemann et al 2008). The temperature differences range from 1.5 K on average (Davies Reef) to 2.5 K on average (Cleveland Bay). At Davies Reef and

Myrmidon Reef, MODIS Aqua and Terra SST's compare well with those from MTSAT. SST's from the NOAA series AVHRRS's compare well with MTSAT data during night and morning. However, for the afternoon points, the MODIS Aqua data compare with MTSAT better (up to 1K difference at Myrmidon Reef) than the NOAA-18 and -19. Bin-averaged SST's from the polar-orbiters at Cleveland Bay are difficult to compare with MTSAT as there are no (MODIS series) or very few (NOAA series) data points, presumably due to proximity to land (Table 8.2).

BARRSL1 station shows an almost flat daily curve. The lowest temperature from MTSAT is at 8am, after that there is gradual warming but the amplitude is relatively small. NOAA-series SST's compare better with MTSAT than MODIS data for this location. The SST plots from ELUSIVEFL1 and ELUSIVESL1 are essentially the same, as these are two measurement series along the same reef. There is a very slight daily warming of about 0.5K, with the lowest temperature occurring in the night and early morning (2:00-8:00), and slightly higher temperature later in the day (10:00-18:00). The SST's derived from measurements from polar-orbiting and geostationary satellites compare with each other well at these two locations. The MODIS Aqua data during the night are binned into three time bins, and we should not pay much attention of the two side ones as those contain very few data thus larger error bars, rather the important one is the bin average value in the middle with majority of the data. The bin average of the middle bin is comparable to other SST measurements.

The last three stations including HALAWS, NKEPPSL1 and PELFL1 do not show an obvious daily cycle, as shown in the geostationary and polar orbiting SST.

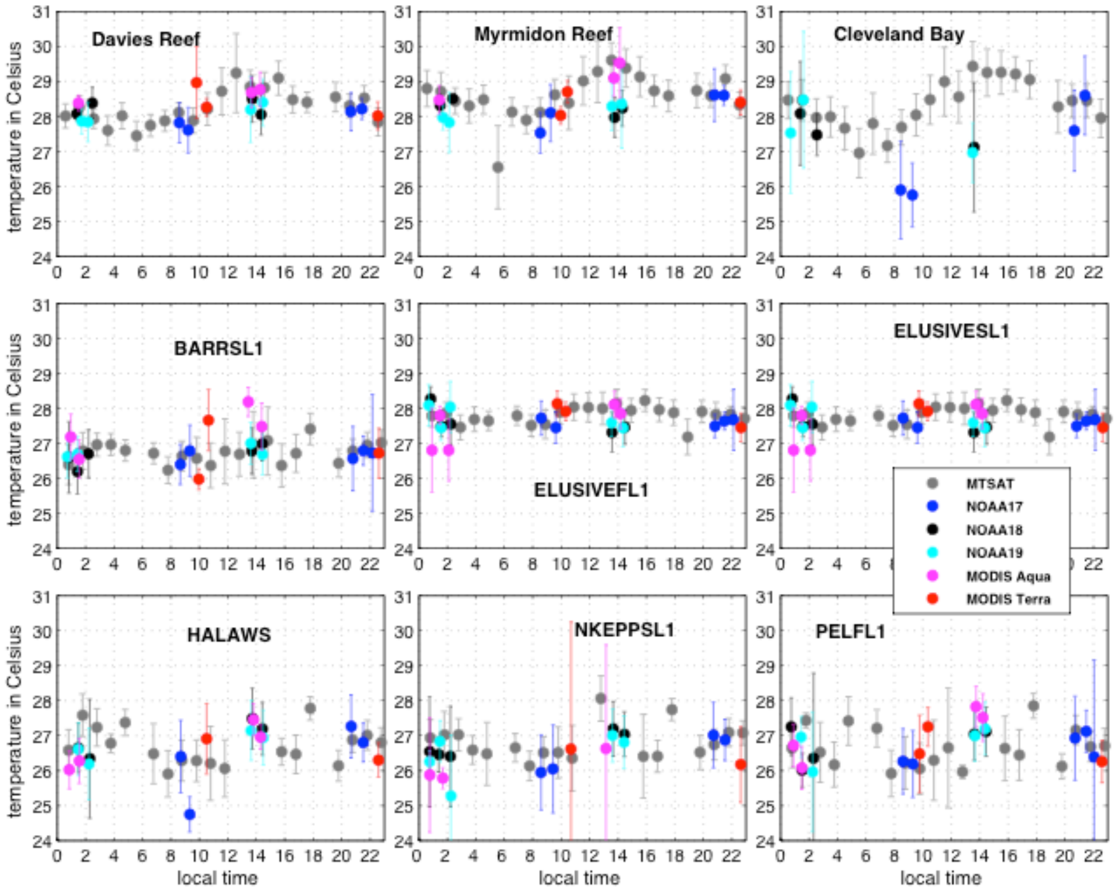

Figure 8.5 Averaged daily temperature evolution captured by different satellite instruments at each station. SST's from different satellite instruments are divided into hourly bins according to local time. The average temperature for each hour is shown by circles, while the 95% confidence intervals are shown by error bars. Note that polar-orbiting satellites cross each location twice a day, but the overpass times vary which leads to two or three adjacent bins being occupied. The bins with a larger confidence error generally result from few data points, and should be considered less important.

### 8.3.2 Comparing diurnal warming signals in SST and in-situ data

In this section, we examine how well the characteristics of diurnal warming signals, both in amplitude and timing, are captured by different satellite instruments, by comparison with in-situ temperature measurements. For this we first concentrate on MTSAT SST's, to examine whether daily warming features shown at each station are consistent with the in-situ temperature measurements.

Comparing the bin-averaged daily temperatures captured by MTSAT and in-situ loggers, we find in-situ data showed similar diurnal warming features for each station as MTSAT, as shown in Figure 8.6.

For Davies Reef, Myrmidon Reef and Cleveland Bay stations, the in-situ data showed similar diurnal warming timing as MTSAT data. Daily maximum temperatures occur around 13:00 to 14:00, while the lowest temperature occurs around 6:00. The Cleveland Bay stations have almost the same average daily warming curve for the MTSAT SST and in-situ data, indicating MTSAT compares closely both in absolute temperatures and in diurnal warming amplitudes to the in-situ measurement. This could be explained by the fact that Cleveland Bay in-situ measurements are located in very shallow water, just below the lowest tide, so the surface SST and bottom measurements are not far apart.

For Davies Reef and Myrmidon Reef, the averaged daily warming amplitudes from MTSAT, i.e., the maximum minus the minimum daily temperature, is larger than the amplitudes at the measurement depths. This makes sense as the surface warming amplitudes tends to be larger. However, the absolute values of the in-situ temperature do not always compare well with satellite-derived SST's. For instance in Davies Reef, the in-situ temperatures are is up to 0.5K higher than the MTSAT data. Considering the in-situ data are measurements on the reef at 4.4-meter depth and SST's are at the sea surface measurement, we expect the in-situ temperatures to be less than the SST's; there appears to be a bias in the satellite-derived SST. One of the possible explanations of such absolute bias is atypical atmospheric profile such as low moisture content (Szczodrak et al 2014), however, it is hard to verify in this study. In summary although the absolute SST might be biased at individual stations, the diurnal warming amplitudes can still be derived with reasonable accuracy.

At the BARRSL1 station, the absolute in-situ temperatures measured at 9m depth are about 1K less than the satellite-derived SST's for the most of day. This could either due to a error in SST retrieval, or the in-situ instrument is faulty. We noticed that the in-situ temperature pattern are very similar, which makes sense due to the closeness in distance between BARRSL1 station and the last three stations. Thus it is more likely that the SST has bias error.The temperature did not show a typical diurnal warming pattern, similar to that shown in the MTSAT data. For the reef flat and reef slope stations at Elusive Reefs, the reef flat measurements at 2m depth are almost the same as the MTSAT measurements, while the afternoon reef slope measurements at 10m is slightly lower that the MTSAT retrievals. Both the in-situ measurements and MTSAT data show a slight (<0.5K) daily warming.

For the remaining three stations, in-situ measurements also do not show obvious daily warming signals, similar to findings from MTSAT data.

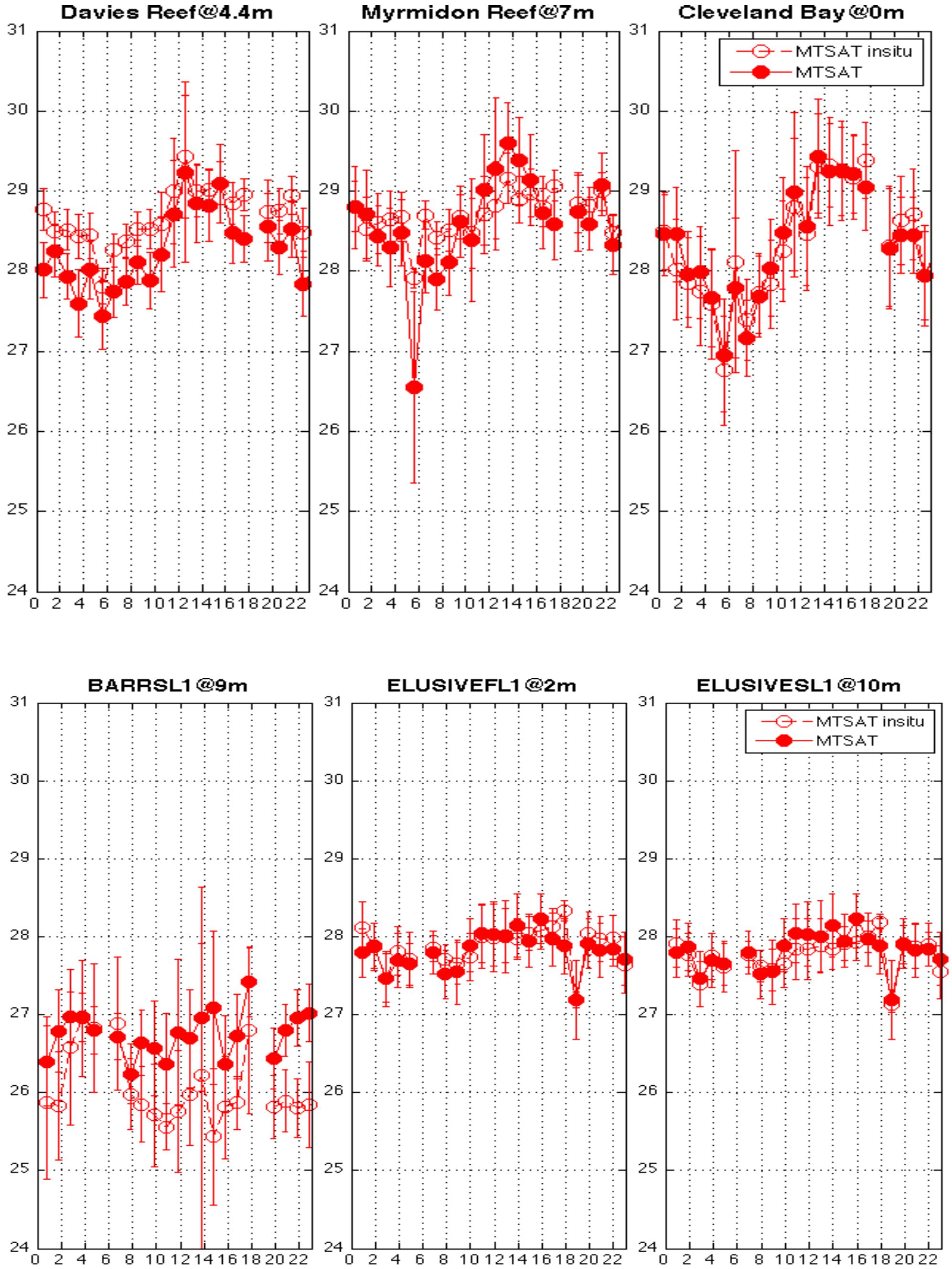
Davies Reef@4.4m
Myrmidon Reef@7m
Cleveland Bay@0m
BARRSL1@9m
ELUSIVEFL1@2m
ELUSIVESL1@10m
MTSAT insitu
MTSAT
31
30
29
28
27
26
25
24
0 2 4 6 8 10 12 14 16 18 20 22

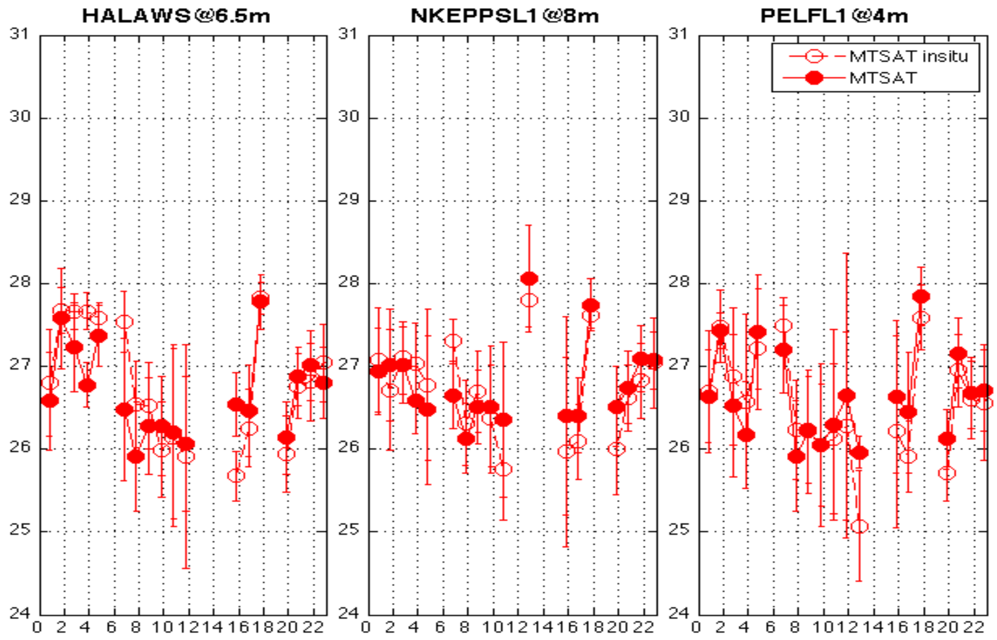

Figure 8.6 Averaged daily temperature evolution captured by in-situ loggers at the sea bottom (empty circles) compared MTSAT SST (filled circles) for each station. Temperature measurements are divided into hourly bins according to the local time. The average temperatures for each hour are shown by circles, 95% confidence intervals are shown by error bars.

Next we compared the in-situ measurements at each location with SST's from polar orbiting satellites. Since the polar orbiting satellites produce at most only two measurements every day at a given location at these latitudes (cloud-cover permitting), and different satellites have different overpass times, the comparison is not as easy to visualize as in geostationary cases. To help quantify the comparisons, we calculated four parameters to supplement the information in the plots for each satellite at each station. The first parameter is dSST, which is defined as the differences between satellite-derived SST later in the day and the SST earlier in the day. The second parameter is dinsitu, which refers to in-situ measurement later in the day minus in-situ measurement earlier in the day. The parameter dSST is the daily warming evolution reflected in satellite SST measurements, while dinsitu is the warming evolution reflected in in-situ measurements.

The third parameter 'dT2' is the difference between the SST and in-situ data for the orbit later of the day. 'dT1' is the difference between the SST and in-situ measurements for earlier in the day. The parameters dT2 and dT1 are evaluations of the absolute temperature differences between satellite and in-situ measurements. A day is the regular day starting at 00:00 local time.

NOAA17 has the early morning/evening orbit. Since usually not much warming is shown by 9:20, and often there is significant residual warming at 21:00, the difference of evening minus the morning temperature is therefore often positive. This can be seen in both satellite SST (dSST) and the in-situ temperature (dinsitu). And the warming difference in the satellite signal is often larger. For the absolute temperature though, SST is often lower than in-situ temperature, likely indicating a bias error.

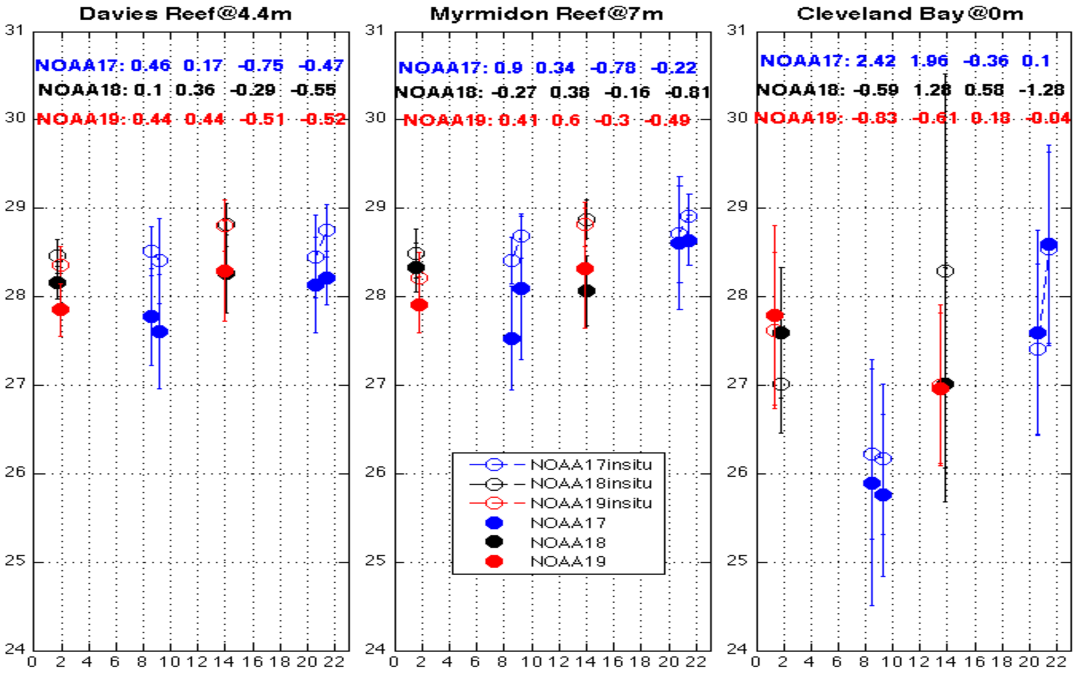

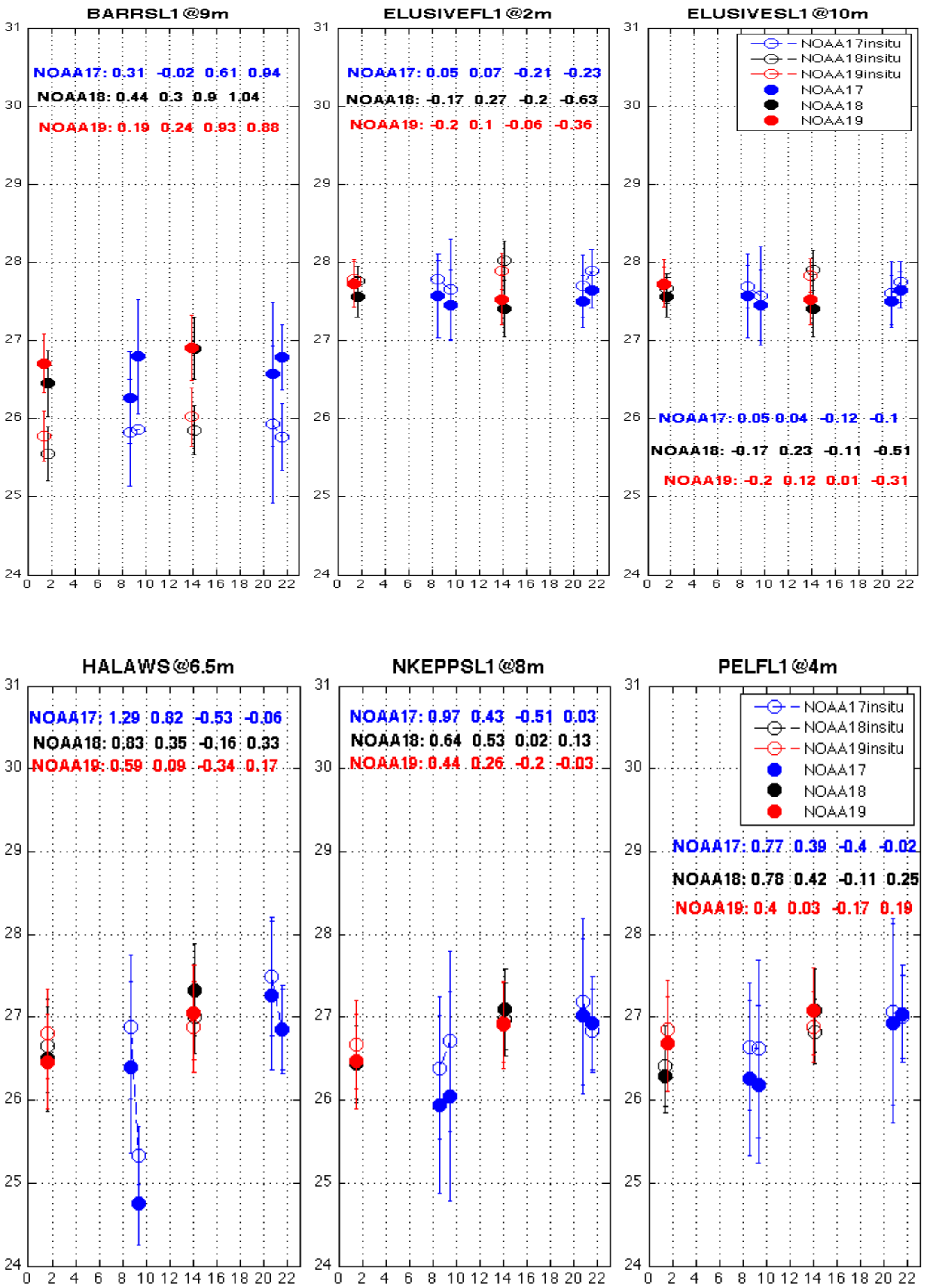

Figure 8.7 Averaged daily temperature evolution captured by in-situ loggers at the depths of the reef at the times of the satellite overpasses (empty circles) compared with NOAA AVHRR SST (filled circles) for each station. The four numbers for each satellite are quantifications of SST and in-situ data comparison. Polar satellites cross the same

locations twice a day, either in a morning orbit or afternoon orbit. The first number is ‘dSST’, which refers to the differences between SST later in the day and the SST earlier in the day. The second column ‘dinsitu' refers to insitu measurement later in the day minus in-situ measurement earlier in the day. The third column 'dT2' is the difference between the SST and in-situ data for the orbit later of the day. 'dT1' is the difference between the SST and in-situ data for earlier in the day. A day is the regular day starts at 00:00 local time.

NOAA18 and NOAA19 are in night/afternoon orbits with local overpass times very close together. For stations with typical diurnal warming characteristics, we expect dSST and dinsitu to be positive. This is true for dinsitu at most stations (except Cleveland Bay due to fewer data points). But for NOAA18 and NOAA19, DSST is sometimes negative for stations shown to have a clear diurnal warming curve (Myrmidon Reef and Elusive Reef), this also could be seen in Figure 8.5. So these two platforms often failed to capture the diurnal warming signatures seen in geostationary datasets.

For NASA MODIS satellites, MODIS Aqua is in a night/afternoon orbit, so we expect the diurnal warming reflected in SST (dSST) is larger than warming signals shown in in-situ data (dinsitu) and both numbers should be positive for stations with obvious daily warming cycle. This holds true for all the stations. For the difference of absolute temperatures, the scenarios are different at different stations. For most stations, the satellite-derived SST data is lower than in-situ measurements at night, which indicates a possible bias error in the satellite SST retrievals, and is often higher than in-situ measurement for the afternoon measurements. The exception is the BARRSL station, where the SST data are about 1K larger than in-situ data for both times of the day, this features could be seen in the MTSAT and in-situ comparisons as well.

Terra is the morning/night orbit with the satellite overhead time at 10:50 and 22:10. Most of the stations have ‘dSST’ less than 0, which means the SST at 22:00 is cooler than during morning at 10:00. The in-situ temperature differences ‘dinsitu’ however, usually shows the SST at 22:00 is not much cooler or is even warmer than at 10:00. This might be due to the fact that the surface temperature warms up faster and cools down faster than the temperature at depth. For most of the stations, Terra MODIS SST is higher than in-situ temperature for the morning orbit, and lower than in-situ for the night orbit, except for the BARRSL1 station.

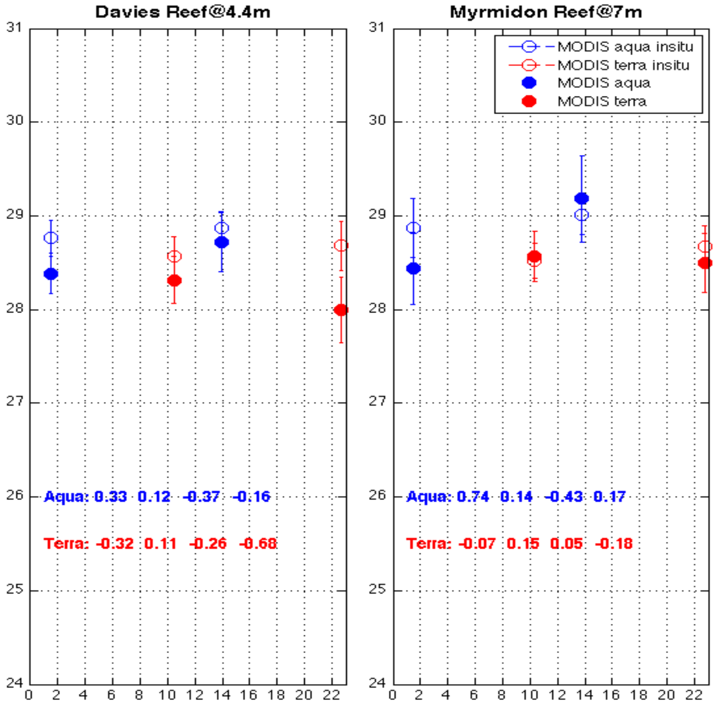

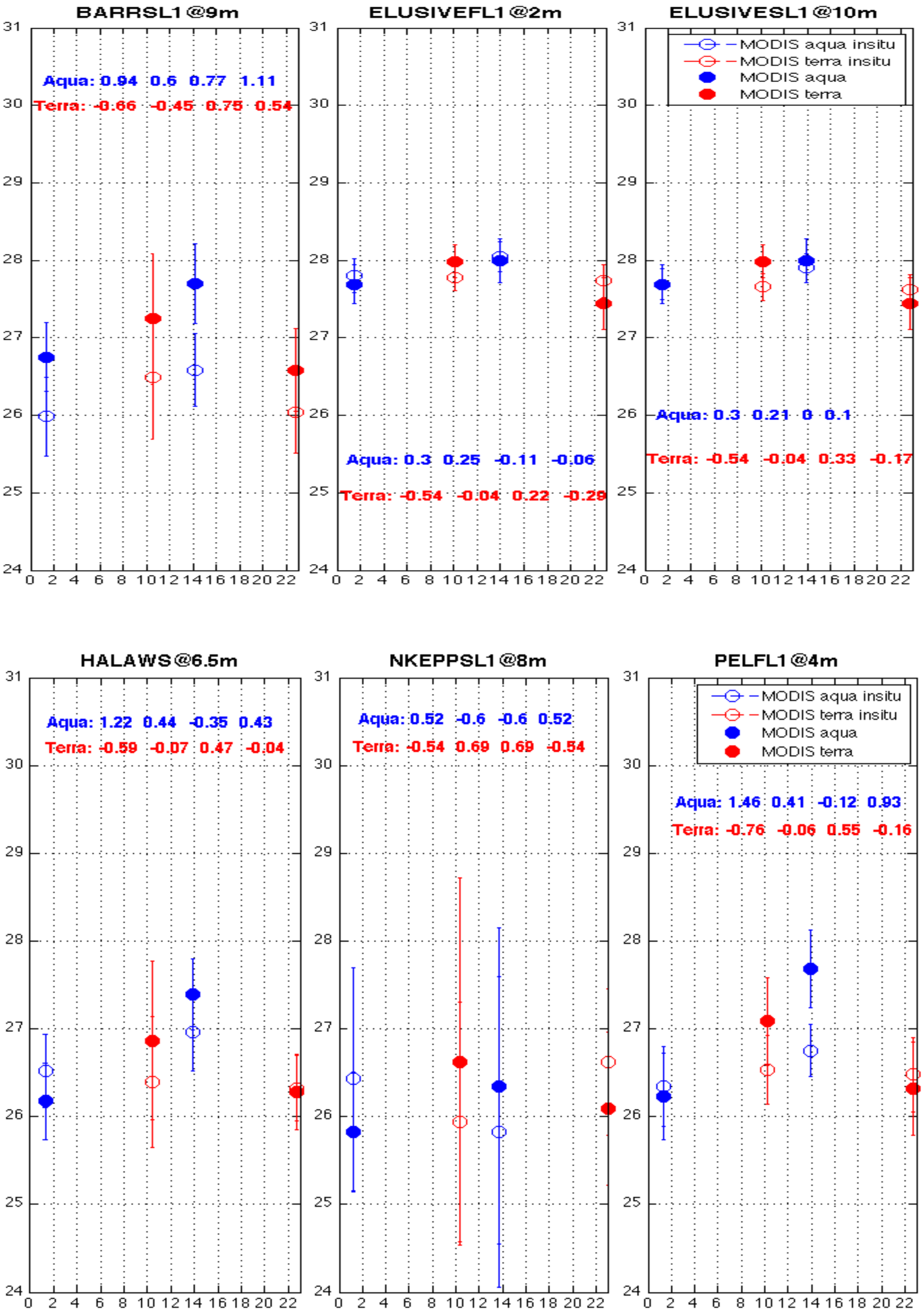

Figure 8.8 As Figure 8.7, but for the Aqua and Terra MODIS.

In this section, the diurnal warming patterns shown in the satellite SST measurements are compared to in-situ temperatures. We found that geostationary SST captured the in-situ diurnal warming pattern particularly well. Although the satellite and in-situ measurements might differ in absolute values, they compare very well in terms of amplitudes and timing of the daily warming.

## 8.4 Concluding remarks

In this chapter, satellite SST from five polar orbiting satellites and one geostationary satellite are compared with in situ temperature measurements from GBR region, to evaluate the ability of SST to capture in-situ temperatures and detect diurnal warming in coastal regions. Comparison of coastal polar-orbiting (AVHRR, MODIS) and geostationary (MTSAT) SST with coral top temperatures shows good agreements, with bias and standard deviation similar or better than similar studies. Diurnal warming pattern (both timing and amplitude) that exist in in-situ temperature datasets are well captured by satellite data, especially by geostationary SST measurements. It is also found that some regional bias corrections are needed to improve SST retrieval.

# Chapter 9 Summary

## 9.1 Major findings

The main goal of this study is to characterize the diurnal warming signals at coastal shallow waters with both in-situ and satellite temperature datasets, and also test and adapt the widely used 1-dimensional diurnal warming models for the coastal case. While the upper ocean daily warming structures for the open ocean have been of interest in recent studies due to their importance in air-sea heat fluxes calculations and satellite surface temperature validations (Clayson and Bogdanoff 2012, Marullo et al 2014), their counterparts for the coastal areas are rarely studied. This is one of the first studies to comprehensively focus on coastal diurnal warming, considering many aspects of coastal related characteristics, including the influence of ocean bottom, tidal impacts and geographic locations, using an integrated approach including in-situ data analysis, modeling and satellite SST analysis.

The characteristics of the shallow water diurnal warming are mostly observed from the in-situ data analysis, while being augmented by modeling. We found that most of the in-situ stations have clear diurnal warming signals at sub-surface depths ranging from less than 1m to over 10m. Even at 7.2m depth or 0.1m above the bottom, we observed consistent daily warming patterns at Little Cayman station. Combining with the model simulations (POSH model, chapter 7), it is shown that the heat penetrates down deeper in our coastal cases than open ocean cases for the same wind and solar radiation strengths, presumably caused by larger coastal vertical mixing. In terms of warming timings, it is shown that the shallower and deeper depths reach the daily warming peaks around the same time for most of the stations which have multiple vertical measurements, while in open ocean studies, larger time lags are shown for warming peaks across depths. Seasonality of the diurnal warming is shown to exist using the data from the Caribbean datasets. We found that the largest warming occurs in springtime, which is explained by a combination of medium strength solar radiation and weak wind speed.

Many environmental parameters are studied for their connections with the coastal diurnal warming characteristics, including those unique to the coastal regions. Similar to open ocean cases, the warming amplitudes are found to be influenced by daily mean wind speeds and daily maximum insolation. We then further study the timeliness of the forcing (not just in an average day sense) at the sample Little Cayman station by linking the forcing with the normalized warming (see Chapter 4). We found that the vertical thermal gradient between different depths are instantaneously influenced by temperature history and wind speeds as the primary impact factors, and influenced by the significant wave heights and insolation as secondary factors. Note that although we don't have wave measuring instruments, the significant wave heights could be estimated from subsurface pressure measurements.

While we take primary interest in the solar-driven daily warming phenomenon, for the coastal regions the tidal elevation changes and tidal currents have such constant presence, that the ability to discern and quantify the tide-induced daily temperature changes is critical. In both in-situ datasets, a parameter $PSD_{M2}/PSD_{24}$ (Chapter 3, Chapter 5) , i.e., the relative ratio of the power spectrum density for the semi-diurnal M2 component versus the 24-hour period component derived from temperature spectra, is found to be a good measure of the relative importance of tides versus solar heating on the temperature. It is interesting to note that even for Great Barrier Reef regions where the tidal changes are very large (2-5 m), the tidal influence on daily warming are mostly minor (< 10%) compared to solar heating. The large tidal influences in warming are mostly related to local features, i.e., if the locations is located close to a tidal inlet (e.g., Lee Stocking Island station CMRC from the Caribbean dataset, or Mourilyan Reef from the GBR dataset).

Another unique coastal feature we studied is the warming dependence on measurement location and the related geographical features. By grouping the Great Barrier Reef stations into different location related categories, it is found that the station water depth, station reef types related to location on coral reef (reef flat, reef slope or deep reef slope) are important factors in influencing warming amplitudes. Also worth noting is that the relative location of the station to the barrier reef chain in the east-west direction influences the warming significantly. The stations in the GBR lagoon or on the western/inner side of the GBR have larger diurnal warming amplitudes on average compared to stations located on the eastern/outer side of the GBR. The stronger warming in the lagoon and on the inner barrier reef is possibly due to more sheltered lagoon environment. On the other hand, latitudes and whether the location is to the west/east to a nearby island did not impact the warming amplitudes.

Testing and adapting the models which have been used in open ocean studies for the coastal region was another objective in our study. Three one-dimensional, physically based empirical warm layer models are used to simulate the warming at our test location, the Little Cayman station. The models include the Profiles of Ocean Surface Heating (POSH) model (Gentemann et al 2009), the Zeng and Beljaars (2005) prognostic diurnal warm layer model and a simple well mixed “box model” which assuming assumes the heat entering the water column will be instantly quickly well mixed throughout the water column. Each model is physically based, yet has certain parameterization assumptions of the vertical profile or turbulence mixing, so that the computation cost is very reasonable. The results show that the very simple "box model" predicts the warming amplitudes better than the other two models during strong and intermediate (>5 $ms^{-1}$) wind speeds. There is however an issue with cooling, which is then improved by adding an empirical correction term, based on the fact that warming/cooling discrepancies between model and data at the end of the diurnal warming day (6am next day) is roughly linearly related to average wind from after midnight to 6am. For the POSH model, the subsurface simulations during high and intermediate wind are much smaller than the measurements at the corresponding depths. But, since we have good results from the box model during those days and the box model could not simulate the stratification during low winds by design, we are mostly interested in the POSH performance during the low wind cases. During the low wind conditions (daily maximum wind speeds of less than 5$ms^{-1}$) , the POSH model produced a very large surface warming, but the heat does not penetrate sufficiently downward, resulting in smaller modeled warming amplitudes at the measurement depths. Also, there is almost always negligible modeled warming near the bottom at 7.2 m, which is not the case in the measurements. Several empirical adjustments were tested, and we found increasing the diurnal warming depth $D_{T,}$ which simulates stronger turbulent mixing, improved the model results best. The Zeng and Beljaars (2005) model performs the worst among the three models. It is shown to be overly sensitive to wind speed, and produced either too much warming during low wind conditions ($U_{max}$≤5$ms^{-1}$) or too little warming during high wind conditions ($U_{max}$≥9$ms^{-1}$).

Ultimately, none of the three models are able to reproduce satisfactory warming signals shown in the measurements under all wind conditions. The attempts to improve the results are mostly empirical and are hindered by the fact that the resolution of vertical temperature measurements is rather limited, as well as the lack of the bottom flux measurements.

The satellite sea surface temperature (SST) with its ever-improving temporal and spatial resolution is becoming increasingly suitable for coastal applications. In this study, we tested satellite SST's accuracy when compared with in-situ measurements as well as tested their suitability for studying the coastal diurnal warming phenomenon. Measurements from infrared radiometers on five polar-orbiters (AVHRR's on NOAA17,18,19 and MODIS's on Aqua and Terra) and one geostationary satellite (MTSAT) were studied together with the in-situ data from Great Barrier Reef region for a four-month period. Comparing the satellite-derived SST against in-situ data from all satellite platforms yielded bias errors of < 0.15K (except for the SST's derived from the measurements of the AVHRR on NOAA-17), and standard deviations of between 0.56K and 0.74K, similar or better than other coastal validation studies (e.g. Li et al., 2001). The average diurnal warming for each station was derived by collecting the temperatures into hourly local time bins. This was done for both the in-situ measurements and satellite SST data. Geostationary SST data are shown to capture the diurnal warming characteristics for most stations well both in amplitudes and timing. This result is very encouraging as previous study by Wick et al. (2002) have found geostationary SST from GOES could not correctly exhibit the diurnal warming cycle due to calibration issues, thus subsequent diurnal warming studies have been very reluctant to utilize geostationary SST. For the

SST’s from polar-orbiting satellites, we compared the in situ measurements and satellite SST data at each overpass time of the day, as well as the warming differences between the two daily overpasses (separated by ~12h) for both measurement and satellite SST data. The comparison results are mixed. The AVHRR on NOAA 17 and the MODIS’s on Aqua and Terra were able to capture the relative warming differences reasonably well, while the AVHRR’s on NOAA 18 and 19 often failed to capture the diurnal warming signatures in their measurements correctly (lower satellite SST during afternoon orbit) . Finally, biases in SST retrievals are observed in the comparison. For example, the absolute values of satellite SST measurements are often lower than the in situ measurements at the same location, which is unlikely in reality as this will cause thermal instability. Also, for certain stations such as Barren Island (BARRSL1), the SST’s from geostationary satellite have a large (0.5K-1K) bias compared to in-situ data throughout the day. Both point to possible biases in the SST retrievals. Fortunately, for most of the cases with suspicious absolute SST value, the relative daily warming amplitude can still be derived with reasonable accuracy.

## 9.2 Future work recommendations

While the two in-situ datasets we analyzed provide a broad coverage in geographic areas of the coral reef warming characteristics and relationship with solar, wind and geolocation related characteristics, the study of shallow water diurnal warming will benefit from more intensive field measurements. Especially for areas like the Great Barrier Reef region, each reef is different because of the complex topography, circulation and wave breaking patterns, and the thermal profile for different parts of the reef is far from uniform. More detailed measurements and hydrodynamic circulation modeling could provide more insights into the intricate interplay between diurnal warming and a host of complex physical parameters, and aid in improving shallow water diurnal warming modeling results.

First, detailed information on water properties and thermal profiles are needed, including higher vertical resolution of the temperature measurements, detailed measurements near the surface and near the bottom layer, water turbidity and chlorophyll contents, as well as measurements of the bottom absorption of the radiative flux. Also given that the diurnal warming is very sensitive to the specific location along the reef structure and reef topography, it will be beneficial to have multiple measurement locations within one reef. Note that the thermal measurements and bottom fluxes measurements are easy to maintain once set up, thus could be set up as long term observation sites. With the newer data, the 1-dimensional diurnal warming we have used for this study could be tested and quantified better. Moreover more complex and physics-based model such as general ocean turbulence model (GOTM) could be used as well, to study the detailed physical processes occurring the shallow water diurnal warming.

Second, currents and wave measurements are needed for the study locations and surrounding areas. Given the shallow and complex topography of the coral reef regions, particularly in regions like Great Barrier Reef where the tidal elevations can be large, current circulation and wave shoaling and breaking could be very important environmental forcing on thermal environments. While our study touched on tidal impacts calculated from temperature spectra, and calculated significant wave heights at one location from pressure measurements, more thorough studies for those forcing require targeted current and wave measurements.

Third, hydrodynamic circulation models could be utilized to study and predict the study site environments. Field measurements of currents and waves could be used to fine tune and validate circulation models, after that, the validated model could simulate and predict the hydrodynamic environments. Combined with the relatively lower cost thermal measurements, the diurnal warming could be studied for longer periods of time.

# References

Altaii, K., Farrugia, R.N., 2003. Wind characteristics on the Caribbean island of Puerto Rico. Renewable Energy 28, 1701-1710.

Berkelmans, R., De'ath, G., Kininmonth, S., Skirving, W.J., 2004. A comparison of the 1998 and 2002 coral bleaching events on the Great Barrier Reef: spatial correlation, patterns, and predictions. Coral Reefs 23, 74-83.

Berkelmans, R., Oliver, J.K., 1999. Large-scale bleaching of corals on the Great Barrier Reef. Coral Reefs 18, 55-60.

Blume, H. ,1974. Caribbean Islands, Longman, London

Bohm, E., Marullo, S., Santoleri, R., 1991. AVHRR visible-IR detection of diurnal warming events in the western Mediterranean. International Journal of Remote Sensing 12, 695-701.

Brinkman, R., Wolanski, E., Deleersnijder, E., McAllister, F., Skirving, W., 2002. Oceanic inflow from the Coral Sea into the Great Barrier Reef. Estuarine Coastal and Shelf Science 54, 655-668.

Burns, B., Taylor, J. and Sidhu, H., 2010. Uncertainties in Bathymetric Retrievals .17th National Conference of the Australian Meteorological and Oceanographic Society IOP Publishing IOP Conf. Series: Earth and Environmental Science 11.

Church, J.A., Andrews, J.C., Boland, F.M., 1985. Tidal currents in the central Great Barrier Reef. Continental Shelf Research 4, 515-531.

Clayson, C.A., & Bogdanoff, A.S. (2012). The Effect of Diurnal Sea Surface Temperature Warming on Climatological Air–Sea Fluxes. Journal of Climate, 26, 2546-2556.

Donlon, C., Robinson, I., Casey, K.S., Vazquez-Cuervo, J., Armstrong, E., Arino, O., Gentemann, C., May, D., LeBorgne, P., Piolle, J., Barton, I., Beggs, H., Poulter, D.J.S., Merchant, C.J., Bingham, A., Heinz, S., Harris, A., Wick, G., Emery, B., Minnett, P., Evans, R., Llewellyn-Jones, D., Mutlow, C., Reynolds, R.W., Kawamura, H., Rayner, N., 2007. The global ocean data assimilation experiment high-resolution sea surface temperature pilot project. Bulletin of the American Meteorological Society 88, 1197-1213.

Doodson, A., 1921. The Harmonic Development of the Tide-Generating Potential, Proceedings of the Royal Society of London, pp. 305-329.

Dunn, S.R., Thomason, J.C., Le Tissier, M.D.A., Bythell, J.C., 2004. Heat stress induces different forms of cell death in sea anemones and their endosymbiotic algae depending on temperature and duration. Cell Death and Differentiation 11, 1213-1222.

Duarte, H.F., Dias, N.L., Maggiotto, S.R., 2006. Assessing daytime downward longwave radiation estimates for clear and cloudy skies in Southern Brazil. Agricultural and Forest Meteorology 139, 171-181.

Fairall, C.W., Bradley, E.F., Godfrey, J.S., Wick, G.A., Edson, J.B., Young, G.S., 1996. Cool-skin and warm-layer effects on sea surface temperature. Journal of Geophysical Research-Oceans 101, 1295-1308.

Flament, P., Firing, J., Sawyer, M., Trefois, C., 1994. Amplitude and horizontal structure of a large diurnal sea surface warming event during the Coastal Ocean Dynamics Experiment. Journal of Physical Oceanography 24, 124-139.

Gentemann, C.L., Donlon, C.J., Stuart-Menteth, A., Wentz, F.J., 2003. Diurnal signals in satellite sea surface temperature measurements. Geophysical Research Letters 30.

Gentemann, C.L., Minnett, P.J., 2008. Radiometric measurements of ocean surface thermal variability. Journal of Geophysical Research-Oceans 113.

Gentemann, C.L., Minnett, P.J., Le Borgne, P., Merchant, C.J., 2008. Multi-satellite measurements of large diurnal warming events. Geophysical Research Letters 35.

Gentemann, C.L., Minnett, P.J., Ward, B., 2009. Profiles of ocean surface heating (POSH): A new model of upper ocean diurnal warming. Journal of Geophysical Research-Oceans 114.

Gentemann, C.L., Wentz, F.J., Mears, C.A., Smith, D.K., 2004. In situ validation of Tropical Rainfall Measuring Mission microwave sea surface temperatures. Journal of Geophysical Research-Oceans 109.

Gill, A.E., 1982. Atmosphere–Ocean dynamics. Academic Press, New York.

Hearn, C.J., Atkinson, M.J., Falter, J.L., 2001. A physical derivation of nutrient-uptake rates in coral reefs: effects of roughness and waves. Coral Reefs 20, 347-356.

Kawai, Y., Otsuka, K., Kawamura, H., 2006. Study on diurnal sea surface warming and a local atmospheric circulation over Mutsu Bay. Journal of the Meteorological Society of Japan 84, 725-744.

Kjerfve, B., 1981. Tides of the Caribbean sea. Journal of Geophysical Research-Oceans and Atmospheres 86, 4243-4247.

Kundu, P.K., Cohen, I.M. 2002. Fluid mechanics, second edition. Academic Press.

Large, W.G., McWilliams, J.C., Doney, S.C., 1994. Oceanic vertical mixing – a review and a model with a nonlocal boundary-layer parameterization. Reviews of Geophysics 32, 363-403.

Li, X., Pichel, W., Clemente-Colon, P., Krasnopolsky, V., Sapper, J., 2001. Validation of coastal sea and lake surface temperature measurements derived from NOAA/AVHRR data. International Journal of Remote Sensing 22, 1285-1303.

Luick, J.L., Mason, L., Hardy, T., Furnas, M.J., 2007. Circulation in the Great Barrier Reef Lagoon using numerical tracers and in situ data. Continental Shelf Research 27, 757-778.

Marullo, S., Minnett, P., Santoleri, R., Tonani, M., & N.Pinardi (2014). SST Diurnal Cycle and Heat Budget Estimates over the Mediterranean Sea. In, *Earth Observation for Ocean-Atmosphere Interactions Science 2014, Responding to the new scientific challenges of SOLAS. 28th-31st October 2014*. European Space Research Institute, Frascati, Italy: European Space Agency.

McClanahan, T.R., Ateweberhan, M., Sebastian, C.R., Graham, N.A.J., Wilson, S.K., Bruggemann, J.H., Guillaume, M.M.M., 2007. Predictability of coral bleaching from synoptic satellite and in situ temperature observations. Coral Reefs 26, 695-701.

Merchant, C.J., Filipiak, M.J., Le Borgne, P., Roquet, H., Autret, E., Piolle, J.F., Lavender, S., 2008. Diurnal warm-layer events in the western Mediterranean and European shelf seas. Geophysical Research Letters 35.

Miller, S.T.K., Keim, B.D., Talbot, R.W., Mao, H., 2003. Sea breeze: Structure, forecasting, and impacts. Reviews of Geophysics 41.

Ohlmann, J.C., Siegel, D.A., 2000. Ocean radiant heating. Part II: Parameterizing solar radiation transmission through the upper ocean. Journal of Physical Oceanography 30, 1849-1865.

Park, K., Lee, E., Li, X., Chung, S., Sohn, E., Hong, S., NOAA/AVHRR sea surface temperature accuracy in the East/Japan Sea, 2014. International Journal of Digital Earth.

Paulson, C.A., Simpson, J.J., 1981. The temperature difference across the cool skin of the ocean. Journal of Geophysical Research-Oceans and Atmospheres 86, 1044-1054.

Price, J.F., Weller, R.A., Pinkel, R., 1986. Diurnal cycling – observations and models of the upper ocean response to diurnal heating, cooling and wind mixing. Journal of Geophysical Research-Oceans 91, 8411-8427.

Reidenbach, M.A., Monismith, S.G., Koseff, J.R., Yahel, G., Genin, A., 2006. Boundary layer turbulence and flow structure over a fringing coral reef. Limnology and Oceanography 51, 1956-1968.

Soloviev, A., Lukas, R., 1997. Observation of large diurnal warming events in the near-surface layer of the western equatorial Pacific warm pool. Deep-Sea Research Part I-Oceanographic Research Papers 44, 1055-1076.

Strong, A.E., Liu, G., Meyer, J., Hendee, J.C., Sasko, D., 2004. Coral reef Watch 2002. Bulletin of Marine Science 75, 259-268.

Stuart-Menteth, A., Robinson, I. S., Weller, R. A., Donlon C. J, 2005. Sensitivity of the diurnal warm layer to meteorological fluctuations part 1: observations, Journal of Atmospheric and Ocean Science, pp. 193–208.

Szczodrak, M., Minnett, P.J. and Evans, R.H., 2014. The effects of anomalous atmospheres on the accuracy of infrared sea-surface temperature retrievals: Dry air layer intrusions over the tropical ocean, Remote Sensing of Environment 140, 450-465

Thorrold, S.R., Shenker, J.M., Maddox, E.D., Mojica, R., Wishinski, E., 1994b. Laval supply of shorefishes to nursery habitats around Lee-stocking Island, Bahamas. 2. Lunar and oceanographic influences. Marine Biology 118, 567-578.

Toba,Y., Local balance in the air-sea boundary processes I. On the growth process of wind waves.J. Oceanogr. Soc. Japan, 28, 109–120, 1972

Vogel, K., Gektidis, M., Golubic, S., Kiene, W.E., Radtke, G., 2000. Experimental studies on microbial bioerosion at Lee Stocking Island, Bahamas and One Tree Island, Great Barrier Reef, Australia: implications for paleoecological reconstructions. Lethaia 33, 190-204.

Ward, B., 2006. Near-surface ocean temperature. Journal of Geophysical Research-Oceans 111.

Webster, P. J., C. A. Clayson, and J. A. Curry. 1996. Clouds, radiation, and the diurnal cycle of sea surface temperature in the Tropical Western Pacific.Journal of Climate no. 9 (8):1712-1730.

Wick, G.A., Bates, J.J., Scott, D.J., 2002. Satellite and skin-layer effects on the accuracy of sea surface temperature measurements from the GOES satellites. Journal of Atmospheric and Oceanic Technology 19, 1834-1848.

Wolanski, E., 1982. Low-level tradewinds over the western Coral Sea region, Journal of Applied Meteorology, pp. 881-882.

Wolanski , E., 1994. Physical Oceanographic Processes of the Great Barrier Reef. CRC Press.

Wolanski, E., Spagnol, S., 2000. Sticky waters in the Great Barrier Reef. Estuarine Coastal and Shelf Science 50, 27-32.

Zeng, X.B., Beljaars, A., 2005. A prognostic scheme of sea surface skin temperature for modeling and data assimilation. Geophysical Research Letters 32, 4.